UCONN LIBRARY

University of Connecticut
OpenCommons@UConn

Doctoral Dissertations | University of Connecticut Graduate School

6-21-2016

Soot and PAH Formation in Counterflow Non-Premixed Flames: Atmospheric Butane and Butanol Isomers, and Elevated-Pressure Ethylene

Pradeep K. Singh
pradeep.singh@uconn.edu

Follow this and additional works at: https://opencommons.uconn.edu/dissertations

Recommended Citation
Singh, Pradeep K., "Soot and PAH Formation in Counterflow Non-Premixed Flames: Atmospheric Butane and Butanol Isomers, and Elevated-Pressure Ethylene" (2016). *Doctoral Dissertations*. 1098.
https://opencommons.uconn.edu/dissertations/1098

Soot and PAH Formation in Counterflow Non-Premixed Flames: Atmospheric Butane and Butanol Isomers, and Elevated-Pressure Ethylene

Pradeep Kumar Singh, PhD

University of Connecticut, 2016

Due to the complexity of the fluid dynamics and non-linear reactions in the combustion zone, a simplified approach to study this process is required. Given these complexities, it is practically very challenging to take measurements in very high temperature and pressure zones in practical combustion systems, and if by any means those measurements can be made, it is equally challenging to analyze those measurements. Hence, in order to more comprehensively understand these processes, the problem needs to be resolved into the smaller and controllable sub-category of experiments, by creating laminar flamelets. One approach used in creating these flamelets is by establishing simplified non-premixed flames in the counterflow configuration. Alongwith all the fundamental properties of combustion, it is important to study the health hazard and environmentally detrimental emissions, such as soot and polycyclic aromatic hydrocarbons (PAHs). Such combustion studies need to be carried out using the *non-intrusive in-situ* optical diagnostics measurement techniques, such as the Laser Induced Incandescence (LII), Planar Laser Induced Fluorescence (PLIF) and Light Extinction (LE). These measurements for renewable biofuels aid in better understanding of the soot formation process, as well as in developing the fuel specific knowledge to bring them into commercial use. Furthermore since the most practical combustion systems operate at elevated pressures, it is also important to understand the soot formation process under elevated pressure conditions. Considering these, in the current study, the soot and PAH formation processes for butane and butanol isomers (C_4

fuels) at atmospheric pressure; and for ethylene at elevated pressure have been experimentally investigated and compared in a counterflow non-premixed flame configuration.

Under the investigated conditions, butane isomers were observed to form more soot than butanol isomers, thereby showing the effect of the hydroxyl group. The effects of isomeric structural differences on sooting propensity were also observed within the butane and butanol isomers. In addition, while soot volume fraction was seen to increase with increasing fuel mole fraction, the ranking of sooting propensity for these C_4 fuels remained unchanged. For the conditions studied, the sooting tendency ranking generally follows *n*-butane > *iso*-butane > *tert*-butanol > *n*-butanol > *iso*-butanol > *sec*-butanol. . The counterflow non-premixed flames were also simulated using the gas-phase chemical kinetic models, USC Mech II [1], Sarathy *et al.* [2] and Merchant *et al.* [3] available in the literature to compute the spatially-resolved profiles of soot precursors, including acetylene and propargyl.

For these C_4 fuels, the PAHs of various aromatic ring size groups (2, 3, 4, and larger aromatic rings) have been characterized and compared in non-premixed combustion configuration. In particular, the formation and growth of the PAHs of different aromatic ring sizes in these counterflow flames was examined by tracking the PAH-PLIF signals at various detection wavelengths. PAH-PLIF experiments were conducted, by blending each of the branched-chain isomers with the baseline straight-chain isomer, in order to study the synergistic effects. The fuel structure effects on the PAH formation and growth processes were also analyzed by comparing the PAH growth pathways for these C_4 fuels. A chemical kinetic model, POLIMI mechanism [4-7], available in the literature that includes both the fuel oxidation and the PAH chemistry was also used to simulate and compare the PAH species up to A_4 rings.

Pradeep Kumar Singh, University of Connecticut, 2016

Counterflow non-premixed sooting ethylene–air flames with fuel mole fractions of 0.20–0.40 in the pressure range of 1–6 atm were investigated experimentally with the laser diagnostic techniques of LII, PLIF and LE. A better understating of the quantitative soot formation process has been developed for ethylene counterflow flames under elevated pressure conditions. The effect of pressure on the formation of PAHs with different aromatic ring sizes has also been determined qualitatively. With increase in pressure, the increase in soot volume fraction and PAH-PLIF signals were observed. A chemical kinetic model available in the literature, that includes both the fuel oxidation and the PAH chemistry, was also used to simulate and compare the PAH species up to A_4 rings. At the incipient stage of the PAH formation, the simulated results exhibited similar behavior to the experimental observations. A chemical kinetic model, WF-PAH mechanism [8], available in the literature was also used to compute the PAHs up to four aromatic rings. This chemical kinetic model predicted enhancing PAHs formation with an increase in pressure, consistent with the experimental trend.

Soot and PAH Formation in Counterflow Non-Premixed Flames: Atmospheric Butane and Butanol Isomers, and Elevated-Pressure Ethylene

Pradeep Kumar Singh

B. Tech, Indian Institute of Technology, Kharagpur, India

M.Tech, Indian Institute of Technology, Kharagpur, India

A Dissertation

Submitted in Partial Fulfillment of the

Requirements for the Degree of Doctor of Philosophy

at the

University of Connecticut

2016

Copyright by

Pradeep Kumar Singh

APPROVAL PAGE

Doctor of Philosophy Dissertation

Soot and PAH Formation in Counterflow Non-Premixed Flames: Atmospheric Butane and Butanol Isomers, and Elevated-Pressure Ethylene

Presented By

Pradeep Kumar Singh, B. Tech, M.Tech

Major Advisor_____

Chih-Jen Sung

Associate Advisor_____

Michael Renfro

Associate Advisor_____

Baki Cetegen

University of Connecticut

2016

Acknowledgements

I would like to extend thanks to the many people, who so generously contributed to the work presented in this thesis.

First of all, special mention goes to my supervisor, Prof. Chih-Jen Sung. I wholeheartedly thank him, not only for his tremendous academic support, but also for giving me so many wonderful opportunities. His patience and diligence with me was very essential in my PhD journey, for me to try harder during the unfavorable times.

Similar, profound gratitude goes to Prof. Baki Cetegen and Prof. Michael Renfro, for accepting to be my committee members. During all my interactions with them, I felt that I found a right direction to tread on, which was a great support. I also thank Prof. Ugur Pasaogullari and Prof. Jason Lee for participating in my dissertation defense.

I am also hugely appreciative of all my present and past lab members, especially for sharing their experience and knowledge to make this dissertation possible. Many thanks to the technical and administrative support experts, for making it easier for me to work on my research work.

Special thanks to the funding agency, Combustion Energy Frontier Research Center, an Energy Frontier Research Center funded by the U.S. Department of Energy, Office of Science, Office of Basic Energy Sciences, without their financial support this dissertation would not have been possible.

Finally, but by no means least, special thanks go to my family for unbelievable support. They are the most important people in my world and I dedicate this thesis to them.

Dedicated to the Supreme Being

Table of Content

List of Figures

List of Tables

Chapter 1: Introduction

Energy is the most crucial factor in the progress of the modern economies. As the economies around the world develop rapidly, the demand for energy also increases. The demand for energy in the world is expected to triple by the end of this century [9]. Combustion is the major sources of the current energy generation process [9]. Wherein, the combustion process is necessary in the generation of energy, it results in the production of harmful bi-products, in the form of gaseous and particulate emissions. Soot emission from fuels is one of such emissions, which is integral part of the combustion process, which requires better understanding for the fuels to be wisely used in the practical combustion systems. These soot emissions are health hazardous as these are known to be carcinogenic, and create respiratory diseases. Alongside, these soot emissions are detrimental for the environment, such as these are responsible for the global warming. One of the key challenges the society faces is to meet the energy demand and at the same time protect its environment. Remedies to the shortcomings of the combustion process are twofold. First, to develop alternative fuels, which can be directly used in the present combustion based infrastructure. Secondly, develop the understanding of the complex combustion processes, including the emission processes. In any of the combustion systems, the process of combustion is turbulent flow and non-linear reacting chemistry. Due to the complexity of the fluid dynamics and non-linear reactions in a practical combustor, a simplified approach to study this process is required. Given these complexities, it is practically very challenging to take measurements in a hostile environment inside the combustion systems, and if by any means those measurements can be made, it is equally challenging to interpret those measurements. Hence, in order to more comprehensively understand these processes, the problem needs to be

resolved into the smaller and controllable experiments, such as by creating laminar flamelets. One approach used in creating these flamelets is by establishing simplified non-premixed flames in the counterflow configuration. Most of the combustion systems are mixing-rate controlled and lead to a non-premixed flame in which fuel and oxidizer are introduced separately [10]. The study of the combustion processes such as soot formation and polycyclic aromatic hydrocarbon (PAH) formation, in these laminar flamelets aids in the development of better chemical kinetic models. These flamelets can be studied under varying parameters to measure the effects of practical combustion system relevant parameters such as fuel loading, oxidizer loading, residence time, temperature and pressure. In general, turbulent flames can be considered as an ensemble of strained, quasi-one-dimensional, laminar flamelets, represented by a non-premixed counterflow flame. This approach can help in the control of the combustion environment inside practical combustion systems, hence can aid in reducing the environmental emissions. Further in the process of solving the aforementioned challenges, alternative fuels can be used. Alternative fuels, which can be produced using the biological processes from the biomass, result in less net contribution of emission to the environment, compared to the fossil fuels. In the production of the biofuels from the biomass, the carbon sequestration and emission process is a cyclic process. Fossil fuel formation process depends on the natural processes, whereas the processes to produce biofuels have been discovered. The usage of the biofuels in the existing fuel based energy infrastructure requires us to study the fundamental combustion properties for them to facilitate the switch to these fuels.

1.1 Motivation

Currently, 80% of world energy demand is met by using fossil fuels [9]. With the projected world energy demand expected to triple by the end of this century [9], alternative and renewable

means of energy resources have huge potential in meeting the ever increasing world energy demand. Biofuels, amongst many other alternative sources of energy, offer multiple benefits in terms of providing energy security, economic advantages, and environmental protection [9].

Extensive research has been conducted on biofuels that are produced from biomass. The so-called second generation biofuels do not pose a threat to food security as these biofuels can be produced from inedible crops [11]. Butanols are second generation biofuels, which are considered as a substitute to currently used first generation ethanol as blend in gasoline. Butanol isomers are high in energy density (36 MJ/kg) compared to ethanol (27 MJ/kg) [12]. Additionally, butanol isomers except for *tert*-butanol are less miscible in water than ethanol, and hence provide ease in fuel distribution through existing infrastructure [11]. Biochemical processes for butanol isomers production, except for *tert*-butanol, have been established and are less capital intensive [11, 13]. *tert*-Butanol that is derived as a petroleum by-product from the propylene oxide, is often used as an octane enhancer in gasoline [14].

As biofuels are considered for practical applications, interest of the research community in fundamental research for butanol isomers has been increasing. The investigation of their fundamental properties assists in the design of advanced engines and combustion systems, to control the combustion processes. This is evident as there have been numerous fundamental combustion studies of butanols conducted on laminar premixed and non-premixed flames e.g., [15-34], flow reactors e.g., [3, 35-39], ignition delays in shock tubes e.g., [40-49] and rapid compression machines e.g., [50-53] fuel pyrolysis e.g., [54-59], and jet stirred reactors e.g., [16, 22, 28, 59-64]. In addition, engine studies were conducted for butanol isomers to determine brake specific fuel consumption, exhaust gas temperature, and thermal efficiency e.g., [65-71].

Fundamental soot formation process is proposed to be a highly hierarchical process which starts from the gas phase chemistry and grows to the solid phase chemistry of soot formation. In the gas phase chemistry fuel breaks into the major and minor species of combustion products, some of these minor species responsible for the soot formation process are known as the precursors. In the development of soot chemistry, precursors such as acetylene (C_2H_2) and propargyl (C_3H_3) are widely known as the fundamental building blocks. The soot formation process as such starts from these precursors to incipient aromatic rings such as benzene (C_6H_6) formation. Then these incipient aromatic rings grow to form the larger aromatic rings known as the polycyclic aromatic hydrocarbons (PAHs). Several pathways of these aromatic ring formation and growth have been proposed.

Polycyclic aromatic hydrocarbons (PAHs) are the precursors in the soot formation process in combustion [72-75]. The PAHs are also known to be harmful to the environment and human health. The PAHs can be generated by various sources such as in the internal combustion engines used for transportation and in the combustors used for power generation, as a result of incomplete combustion. The regulatory measures over time have become more stringent to reduce the particulate emissions from engines and combustors. Moreover, the design of modern combustion engines and devices requires understanding the fundamental PAH/soot formation and growth chemistry to achieve this goal. The widely accepted H-abstraction-C_2H_2-addition (HACA) mechanism of the PAH and soot formation was proposed by Frenklach and coworkers e.g.,[8, 76-80]. Apart from the HACA mechanism, the pathways involving propargyl, allyl, cyclopentadienyl, and indenyl have also shown to contribute to the PAH and soot formation processes cf.[81-89]. Recently, Schenk *et al.* [90] have proposed the methyl- and phenyl-addition pathways of the PAH and soot formation. In addition, the odd-carbon-atom pathways have been

introduced as possible reaction routes of the incipient PAH formation, as the propargyl has been proposed to produce reasonantly stable benzene rings [91-95]. Numerical studies have suggested that the propargyl is also responsible for the PAH growth pathways leading to the soot formation via the propargyl addition and recombination reactions [95-97].

To develop the soot formation chemistry, understanding the PAH formation process is essential. It is observed that there is a lack of experimental databases of the PAHs to develop the comprehensive soot formation chemistry, even in comparative terms between fuels of the same isomeric class. Considering this, *in-situ* PAH measurements using the *non-intrusive* planar laser-induced fluorescence (PLIF) technique in a counterflow non-premixed flame configuration for the butane isomers and the butanol isomers, can provide a qualitative comparison of PAH growth for the C_4 fuels investigated. Specifically, the C_4 fuels investigated are *n*- and *iso*-butanes, as well as *n*-, *iso*-, *sec*-, and *tert*-butanols. The molecular structures of these fuels are shown in Table 1.

Table 1: Chemical structures of butane and butanol isomers.

n-butane	*iso*-butane	*n*-butanol	*iso*-butanol	*sec*-butanol	*tert*-butanol
	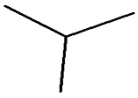	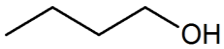	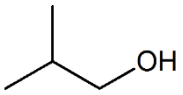	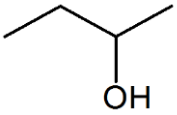	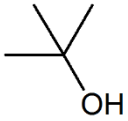

Most practical combustion devices operate at elevated pressures to increase thermodynamic efficiency, resulting in a decrease in their physical size. Consequently, It is important to examine the soot and the polycyclic aromatic hydrocarbons (PAHs) formation at elevated pressures, eventually to control this process [98]. Soot is known to adversely affect the lifetime of the combustion devices as well as pose health related concerns for humans. PAHs have been known as the important class of precursors in soot formation [99, 100], and hence also

play an important role in understanding soot formation mechanisms. In addition, PAHs have been identified to create toxicity/carcinogenicity [101]. Recongizing that ethylene is one of the major olefins produced as an intermediate species in the hydrocarbon combustion and that the study of sooting ethylene flames at elevated pressure conditions would enhance fundamental understanding of the soot formation processes in hydrocarbon flames [102], the current study aims to investigate the soot and the PAH formation processes for counterflow non-premixed ethylene flames at elevated pressure conditions.

1.2 Organization of this dissertation

Chapter 2 describes in detail the experimental apparatus and procedures used in this work, as well as the computational methods and chemical kinetic mechanisms used for the accompanying simulations. The theoretical details of the soot formation process and state-of-the-art optical diagnostic techniques are provided. The justifications of using the parameters used in the experiments have also been discussed in detail.

Chapter 3 provides the detailed discussion of the experimental results of soot formation studies for butane and butanol isomers. The discussion includes the effects of various parameters, such as fuel loading, oxidizer loading and strain rate, on the soot formation process. These experimental results are accompanied by a computational analysis. The discussion of the computational results includes flame structure, concentrations of soot precursors, and chemical pathway analyses based on gas-phase chemistry.

Chapter 4 provides the detailed discussion of the experimental results of soot and polycyclic aromatic hydrocarbon (PAH) formation studies for butane and butanol isomers. The fuel structure effects on PAH formation are presented. Additional experimental results on PAH formation are presented for the binary fuel blends, by blending the branched chain isomer with

the baseline straight chain isomer. These results are compared with the computational results. The pathway analysis for the PAH formation process have also been conducted.

Chapter 5 includes the details of the experimental results of soot and PAH formation for ethylene flames at elevated pressure. The results are analyzed to find the pressure scaling effect on soot and PAH formation process. A chemical kinetic mechanism has been adopted to provide the computational insight on the pressure effect on the soot formation process and this is included in the discussion.

Chapter 6 summarizes the conclusions reached in this dissertation, and suggests future research work that may take advantage of the non-premixed counterflow flame configuration to develop soot models detailing the gas phase chemistry and gas-solid phase chemistry, including the surface growth processes.

1.3 List of publications

Publications associated with this dissertation:

1. P. Singh, X. Hui, and C. J. Sung, Soot formation in non-premixed counterflow flames of butane and butanol isomers, Combustion and Flame, 164, 167-182, 2016.

2. P. Singh, C. J. Sung, PAH formation in counterflow non-premixed flames of butane and butanol isomers, Combustion and Flame, 170, 91-110, 2016.

3. P. Singh, C. J. Sung, Measurement of soot and polycyclic aromatic hydrocarbons in counterflow non-premixed ethylene flames at elevated pressures, under preparation.

Chapter 2 Experimental and Numerical Specifications

2.1 Counterflow burner facility

A counterflow burner facility was used to establish a non-premixed flame, the burner has been shown in Fig. 2.1. The burner consisted of two aerodynamically converging opposing nozzles of 10 mm exit diameter with a separation distance of L=11 mm, as shown in Fig. 2.2. The high pressure chamber body was made of 12.7 mm thick stainless steel with 330.2 mm height and 254 mm diameter. The pressure inside the chamber was controlled by regulating a back pressure regulator. The burner has been demonstrated to achieve stable premixed counterflow flames up to a pressure of 3 atm for liquid fuels [103, 104] and is designed to operate up to 20 atm pressure. More details on this burner facility can be found in [104, 105], and hence a brief description of the system setup is given below. The experimental setup consisting of burner facility including the fuel and oxidizer supply and the laser induced incandescence (LII) setup has been shown in Fig. 2.3. Further details on LII setup will be provided in Section 2.2 of this chapter. Liquid fuels were injected using a high precision liquid fuel pump, and were vaporized by providing heated annular coflow of heated nitrogen in the vaporization chamber. The gaseous fuels, namely butane isomers, were introduced using a mass flow controller, capable of controlling flow rates as low as 20 standard cubic centimeters per minute. Another, gaseous fuel, ethylene was controlled by the pressure gauge and the calibrated sonic nozzles. The fuel/nitrogen mixture was introduced from the bottom nozzle, while nitrogen and oxygen were mixed in a separate line and introduced from the top nozzle. Supply lines from the flow panel to the bottom nozzle were maintained at an appropriate temperature by using heating tapes to prevent condensation of liquid fuels.

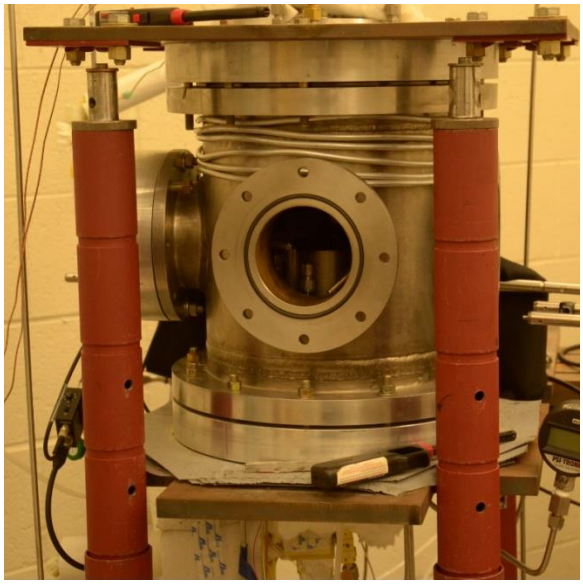

Figure 2.1: High pressure counter-flow flame burner designed to operate at elevated pressure up to 20 atm.

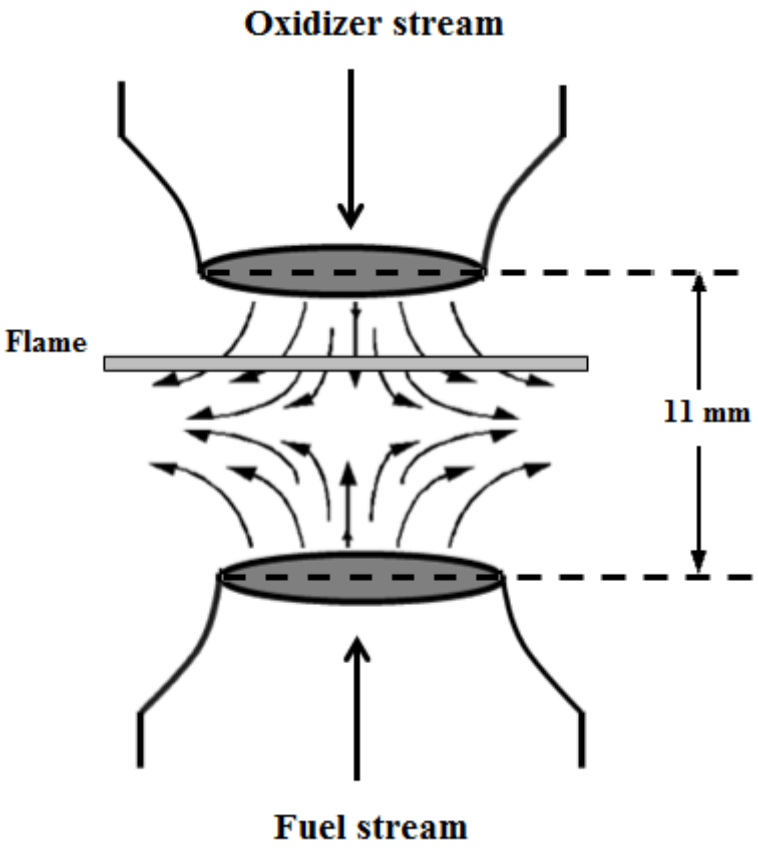

Figure 2.2: Schematic of the counterflow non-premixed flame. Two opposing nozzles have been separated by a distance of 11 mm.

2.2 Laser induced incandescence (LII)

Laser Induced Incandescence (LII) has been widely used technique for soot measurements e.g., [106-128], which is shown in Fig. 2.3 along with the burner and the flow system. In the LII technique, a Continuum Powerlite 8010 Nd:YAG laser was used to provide a laser output of 532 nm wavelength (the second harmonic) at 10 Hz repetition rate. This visible wavelength facilitates precise laser sheet alignment in the center of the burner, which is crucial in soot measurements as the soot volume fraction varies radially and axially. Since the primary soot particle sizes are expected to be in the range of 2–90 nm, the wavelength of 532 nm also fulfills the Rayleigh absorption criterion of $\frac{\pi D}{\lambda} \ll 1$, where D is the diameter of the soot particle and λ is the laser wavelength. The laser beam has a Gaussian profile with the least square factor of 0.95, and the laser power used for the LII measurements was 220 mW. The short laser pulse width of 7 ns results in rapid heating of soot particles, as seen from a representative temporal profile of LII signal shown in Fig. 2.4. It is noted that the LII signal profile in Fig. 2.4 is normalized with the maximum LII signal. The laser beam was guided in the sooting zone using dichroic mirrors. The propagating laser beam has a uniform beam diameter of 8 mm, as the Gaussian beam remains uniform with a very small beam divergence angle of 0.45 mrads. A laser sheet was formed by expanding the laser beam vertically with an expansion factor of 15, through the use of a cylindrical plano-concave lens with a focal length of f=−25.7 mm and a cylindrical plano-convex lens of f=250 mm. Due to the large vertical expansion, the energy distribution in the laser sheet along the vertical direction was uniform. An iris was also used to focus the central part of the laser sheet between the fuel and oxidizer nozzles.

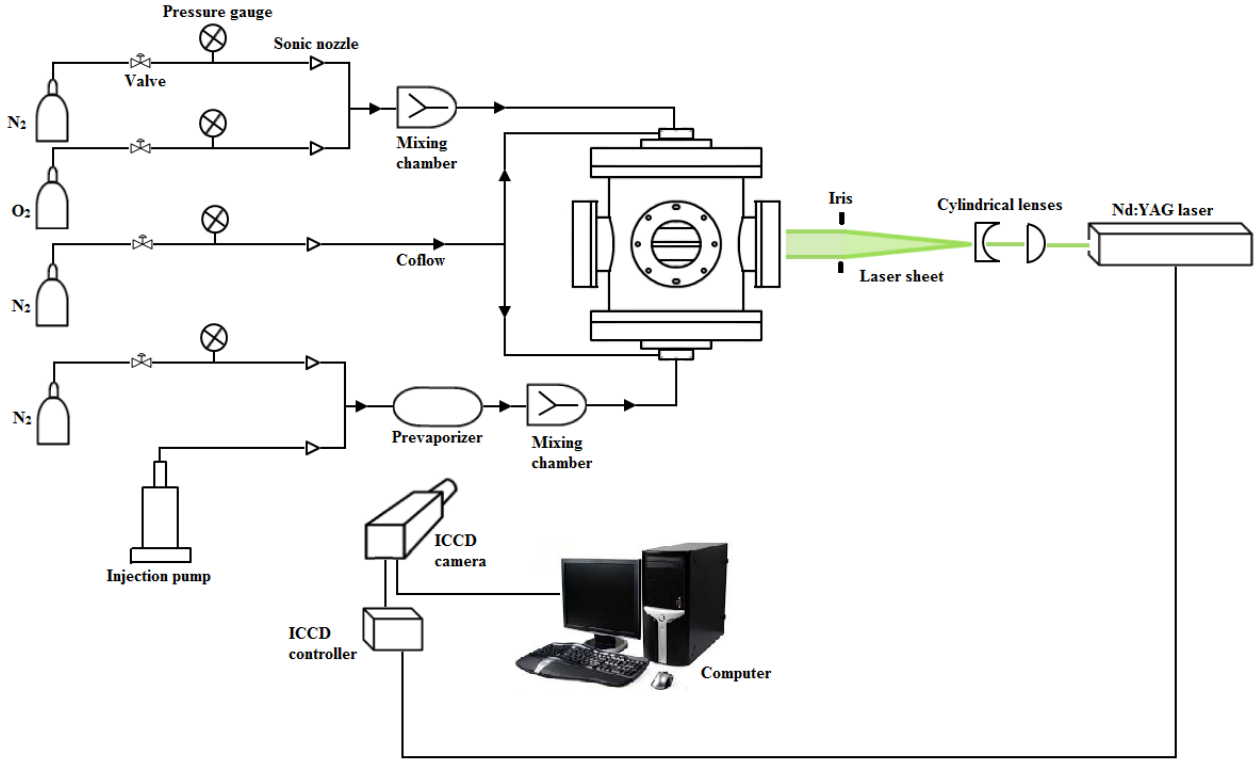

Figure 2.3: Schematic of experimental setup of counterflow non-premixed flame with LII laser diagnostic technique.

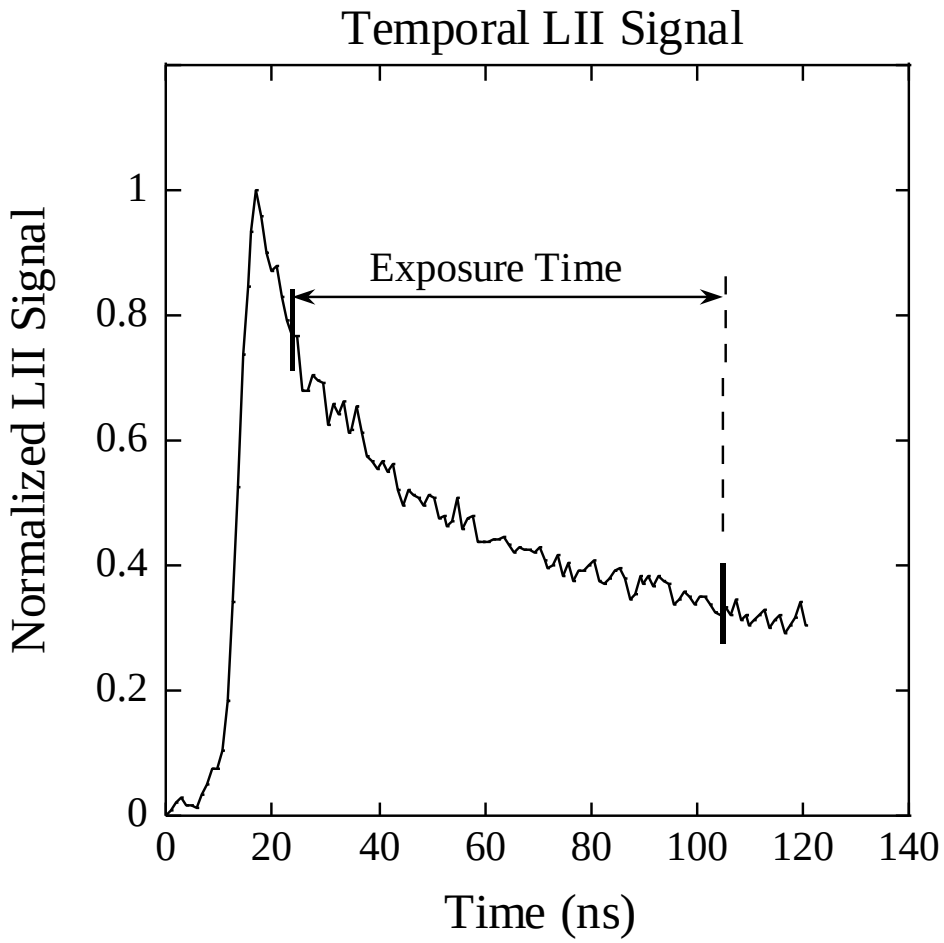

Figure 2.4: Temporal profile of LII signal obtained for an ethylene flame. Normalization is based on the maximum LII signal.

The LII signal was detected in a Peltier cooled intensified CCD camera (Princeton Instrument, PIMAX-3), which has a quantum efficiency of 15% for the detection wavelength of 450 nm. The selection of this particular wavelength will be discussed later in detail. With the current optical setup, the spatial resolution was 0.0384 mm/pixel. The intensified CCD camera was synchronized with the laser using an external trigger from the laser. While the delay settings on the camera will be described in due course, briefly, its selection was set such that the camera shutter would open after the laser pulse arrives in the sooting zone and after the heating of soot particles is achieved. Although the laser pulses reached the sooting zone at a repetition rate of 10 Hz, the soot measurements were conducted at the nanosecond time scale. Such nanoscale measurements permit sufficient time for LII detection between two consecutive laser pulses.

The theoretical basis of LII process is based on transient energy balance mechanism. When soot particles are heated up due to absorption of laser energy, there is a rapid increase in internal energy of the soot particle. The sudden heating of soot particle raises the particle temperature to approximately 4000 K [119]. After attaining such a high temperature, the soot particles cool down due to sublimation, convection, and radiation. The nearly blackbody emission signals due to the radiative cooling process of the soot particles are detected as the LII signals [120]. Because of very high temperatures, sublimation of C_2 species occurs from the soot particle surface, which generates spectroscopic emissions [123]. These C_2 emissions have a wavelength range of 420−650 nm in the Swan band [123], they are a major cause of interference in the LII signal.

In order to determine the exact settings of gate delay and gate width for the experiments, the temporal measurement of LII signal was first analyzed. Figure 2.4 shows a temporal profile of LII signal, with time “0” corresponding to the time when the laser pulse arrives the sooting zone

This profile shows a sharp rise in the LII signal as the soot particles are heated rapidly by a short (7 ns) laser pulse. There is about ~10 ns delay in the signal before it has a sharp rise, this delay is due to the finite temporal laser pulse of 7 ns. After attaining a peak value, the LII signal first decays sharply due to the rapid sublimation cooling process of soot particles [120, 123], and then decays slowly after around 40 ns, as the cooling is subsequently dominated by the slower convective heat transfer process. It is further noted that the cooling rate of a soot particle is proportional to its surface area/volume ratio, which can be expressed as $\frac{D^2}{D^3} \sim \frac{1}{D}$. Thus, smaller soot particles cool down faster, creating a bias towards larger soot particles when a long gate width is used. Two gating approaches, namely prompt and delayed gatings, have been adopted by various researchers [119, 120, 123] for the LII signal. In the prompt gating approach, the gate width opening time is right at the peak of the LII signal. After this peak the cooling process starts. Although the advantage of this approach is that the LII signal avoids the bias created by the particles of larger sizes, however it cannot avoid interferences due to the C_2 emissions. In the delayed gating approach, the gating starts after rapid cooling process is over in the LII signal, e.g., around 40 ns in Fig. 2.4. This gating approach is capable of avoiding the C_2 interferences; however, it tends to include bias due to the slower cooling rate of larger soot particles as discussed earlier. Therefore, a balanced approach of choosing a setting between prompt and delayed gatings was adopted herein to optimize the LII signal [119, 120, 123].

As mentioned earlier, at the onset of the sublimation process, the C_2 emissions due to fluorescence process start, but such interferences have a very short lifetime of approximately 5 ns scale. Since the LII signal peaks at 20 ns, as shown in Fig. 2.4, in the present study the LII data were measured at a gate delay of 25 ns for the atmospheric pressure measurements. This further 5 ns delay from the peak LII signal was found to be adequate in avoiding the C_2 Swan

band interferences from vaporized soot particles. In addition, a gate width of 80 ns was selected to avoid the particle size bias in the LII signal. This gate width was not shortened further as it was observed that the 80 ns gate width was sufficient in providing strong LII signals for all the flame conditions investigated in this study. This gate width was determined by making a comparison of the LII measurements with the LE measurements for varying gate widths. It was found that for our system, and the 80 ns gate width showed a very good agreement between LE and LII measurements. The LE calibration has been described in details in the Section 2.3.

To examine the dependence of the LII signal on varying laser fluence, the laser pulse energy was varied with adjustments of Q-switch delay of the Nd:YAG laser. Laser fluence was calculated as per standard practice of fluence per pulse energy [123]. Since there are soot particles of different sizes and the cooling rate of a particle is dependent on the particle diameter, the LII signal from particles of different sizes may have varying response to the laser fluence. Hence, when determining experimentally-viable laser fluence, the LII signal was integrated for the entire flame, including soot particles of various diameters, so that the spatially-integrated LII signal addresses any bias due to varying particle sizes. This LII profile versus laser fluence has been shown to be independent of the gate width and the fuel type, as shown by Shaddix and Smyth [123] for methane and ethylene flames, and 19 ns and 85 ns gate width. Another type of pressure independence has been demonstrated by Hofmann *et al.* [106] for this same profile. Thus, the LII versus fluence holds good for the different fuels, varying fuel loading, pressure and other parameters due to an insignificant change in the soot morphology, particle diameter, and soot composition. Figure 2.5 shows that an increase in laser fluence results in stronger integrated LII signal, due to the increase in temperature of the soot particles. When the internal energy increases up to a certain point, soot particles attain a temperature where sublimation process

starts, and further increasing the laser fluence does not increase the integrated LII signal anymore [119, 121, 122, 124]. Again, the integrated LII signal in Fig. 2.5 is normalized with the maximum value. As shown in Fig. 2.5, LII signal saturates for the laser fluence beyond a threshold value of ~0.50 J/cm^2. Selecting laser fluence below the threshold value leads to unwanted LII signal-to-signal variation as the soot particle heating process has not yet attained the steady state [120, 123]. Hence, the laser fluence of 0.58 J/cm^2 was chosen for the current experiments. We further note that in Fig. 2.5 a decrease in the LII signal beyond 0.6 J/cm^2 is observed, which may be caused by the particle size reduction due to the sublimation from the surface of the soot particle at higher fluence [125]. As the laser sheet passes through the flame, some of the laser energy is absorbed by the soot particles along the pathway. This absorption may result in bringing the laser fluence below the threshold value across the flame. However, as it is evident from the symmetrical profile of the LII signal shown in Fig. 3.1 (to be discussed in due course in Section 3.2) that the laser fluence of 0.58 J/cm^2 was sufficient to maintain the laser fluence above the threshold value. Statistical measurements of 20 frames were taken, which were averaged. Each frame is recorded after the trigger from the laser for each laser pulse, hence shot to shot variation effect of laser energy is taken into the account. These averaged signals have been compared with the LE measurements using abel's inversion and a good agreement has been observed. This is discussed and shown in details in Section 3.2.

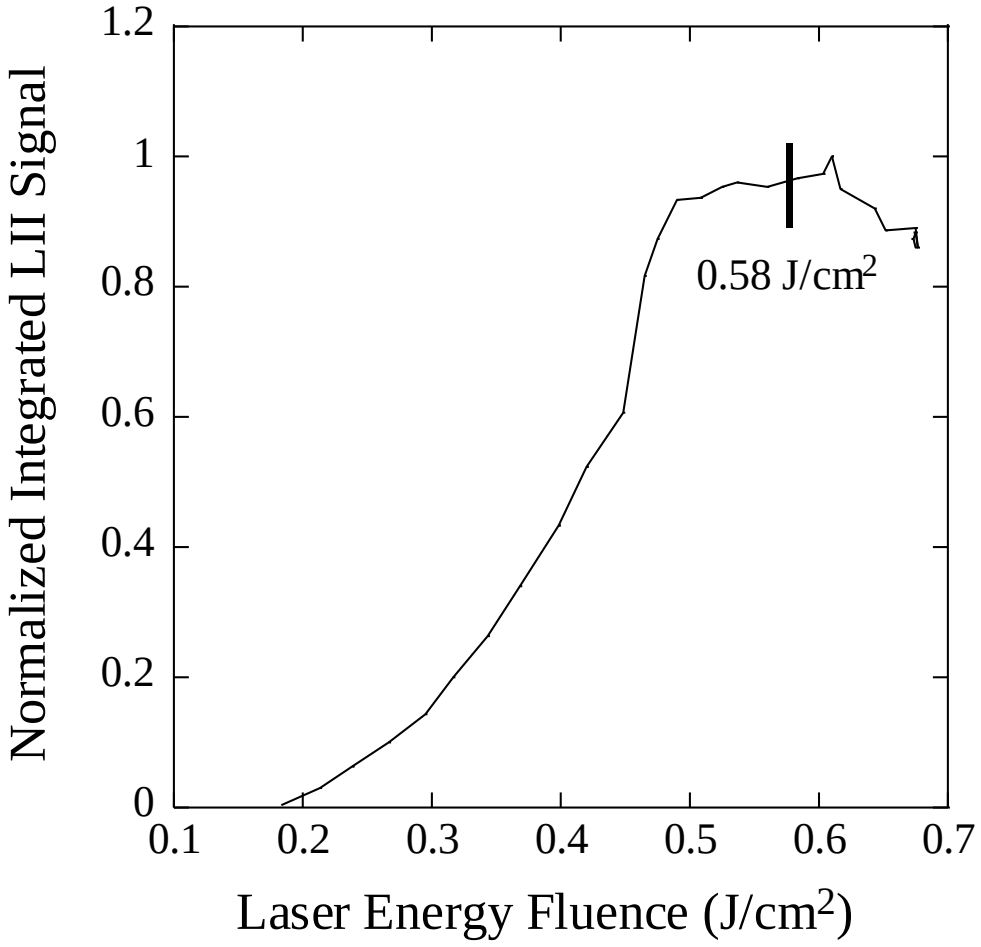

Figure 2.5: Fluence dependence of normalized integrated LII signal measured for an ethylene flame.

A narrow band filter centered at 450±10 nm was used for the present LII measurements. This detection wavelength was selected to avoid/minimize the C_2 Swan band emissions [123]. Polycyclic aromatic hydrocarbons (PAHs) are also known to absorb laser in the UV and visible range, and their fluorescence signals are red shifted [126]. In particular, absorption of 532 nm wavelength laser light by PAHs would emit fluorescence at wavelengths greater than 532 nm. Thus, the use of this narrow band filter centering at 450 nm for LII detection also avoids the PAH fluorescence [126]. We further note that blue-shifted laser induced fluorescence (LIF) signal has been observed in recent studies [129, 130]. Especially, Bejaoui *et al.* [129] showed that excitation at 532 nm results in fluorescence emission in the range of 370–720 nm. However, since LIF signal is typically short lived (~10 ns), the use of delayed gating of 25 ns in the present LII measurements can avoid the potential interference of blue-shifted LIF signals. The avoidance of the noise due to these discussed possibilities of fluorescence sources has been confirmed by comparing the LII measurements with LE measurements for varied fuels and experimental conditions. A good agreement between the LII and LE signals shows that the chosen parameters to avoid the effect of fluorescence were sufficient. In Section 3.2 this calibration process between LII and LE techniques has been discussed in details.

There have been many theoretical and experimental studies conducted to correlate the LII signal with the soot volume fraction. Primary soot particle sizes are small enough to fulfill the critical Rayleigh criterion of scattering, $\frac{\pi D}{\lambda} \ll 1$, with λ=532 nm. Following the study of [127], Eq. (1) defines the theoretical approach of LII measurement:

$$LII \propto \pi D^2 N \int_0^{\tau} M(t) w(t) \int_{\lambda_1}^{\lambda_2} G_r(\lambda)\, \varepsilon(D,\lambda) E_b(T,\lambda) d\lambda dt, \quad (1)$$

where *LII* is the LII signal intensity, N is the soot particle number density, $M(t)$ denotes the mass concentration as a function of time, $w(t)$ is a window function representing the signal

collection gate width, whose duration is τ, $G_r(\lambda)$ is the relative response of the detector and the filter used, which is a function of detection wavelength, $\varepsilon(D,\lambda)$ is the emissivity of soot particle, which is a function of soot particle diameter and detection wavelength, and $E_b(T,\lambda)$ denotes spectral radiance which is a function of wavelength and absolute temperature T. Further, the LII signal in Eq. (1) is shown by [122] to be proportional to the soot volume fraction, f_v, as expressed in Eq. (2):

$$LII \propto f_v = N\frac{\pi D^3}{6}. \quad (2)$$

Theoretical model developed by Melton [128] using the energy balance equation for soot particles has shown that the LII signal detected at wavelength λ_{det} (in μm) is proportional to $D^{3+0.154/\lambda_{det}}$. Selection of λ_{det}=0.450 μm brings the LII signal to be proportional to D^3, i.e. the soot particle volume. A good agreement has been shown between the soot volume fraction measured using the laser light extinction technique and the LII results using 450 nm (0.450 μm) detection wavelength [120, 122]. Experimentally, many studies e.g., [122, 126] have also shown that the LII signal is proportional to the soot volume fraction.

Important questions relating to the application of the LII technique at high pressure need to be addressed. Regarding the interference from the PAH fluorescence signal, the use of an appropriate narrow-band filter, as well as settings in gate width and time delay, to avoid such an interference have been discussed in [131, 132]. Since the increase in pressure increases the PAH fluorescence quenching rate, the PAH fluorescence signal decreases. As such, the interference (if any) in the LII signal due to PAH fluorescence decreases with increasing pressure. Regarding the choices of gate delay and gate width for LII signal detection, it is noted that the time-resolved LII signal is dependent on pressure, as described in [131, 133-135]. After reaching the peak intensity because of laser heating, this time-resolved LII signal decay rate is controlled by the heat

conduction mechanism. The heat conduction depends on the local gas kinetics conditions, and is determined by the pressure dependency of the mean free path and soot particle diameter [98]. Due to the vaporization dominant heat loss mechanism [134, 135], the time-resolved LII signal decays are self-similar during the first 30 ns at all investigated pressures. Beyond 40 ns, the LII signals show a mono-exponential decay, which is dominated by the heat conduction as shown in Fig. 2.4. During this mono-exponential decay regime, the LII signal profiles are shown to diverge with pressure, as the conduction rate is higher for higher pressure. To avoid pressure dependence on the LII signal, it has been suggested [135-138] that the data to be taken are within the initial 30 ns of decaying, i.e. the vaporization dominant heat loss regime. In the current work, the gate width was kept at 30 ns, but with a delay of 5 ns after the peak LII signal to avoid the interference from the C_2 emisisons [131]. Nevertheless, the present 30 ns window for collectiong the LIII signal is during the pressure-independent, sublimation cooling process. As this gate width of 30 ns is smaller than 80 ns used in our previous study [131], a higher ICCD camera gain needs to be properly set in order to ensure a good strength of the LII signal, as well as avoid any spillover of the electronics noise in the ICCD detector. All the settings were optimized so that the current LII signal strength was similar to that of [131]. Furthermore, 20 LII images were averaged in this study.

A plot of LII signal versus laser fluence shows a maximum plateau region as described in [131] and the laser fluence is supposed to be in that plateau region for it be immune to the laser fluence effect [131, 132]. This plateau is envisaged to shift with the increase in pressure as the conduction rate increases and as per the Clausius-Clapeyron principle the vaporization temperature also increases. The laser heating is supposed to be in equilibrium with the particle cooling for the LII signal to be proportional to the soot volume fraction measurement [128].

However, contrary to this Clausius-Clapeyron principle and hence the vaporization temperature effect, experimental measurements by [136, 139, 140] have shown that there is no systematic change in the dependence of the LII signal versus laser fluence within the investigated pressure range of 1–15 atm. This independence is explained by the importance of non-equilibrium effects such as thermal annealing, delayed vaporization, superheating, stephan flow, and plasma formation [106]. In the current experiments, the laser fluence was therefore chosen as 0.58 J/cm^2, as discussed in details in [131]. Experimental measurement by Hofmann *et al.* [106] has also shown that the calibration using the light extinction (LE) technique for the LII measurements did not show any pressure effect. The calibration process using the LE technique conducted at elevated pressure in the current study will be shown and discussed later in detail.

2.3 Laser light extinction (LE)

The light extinction (LE) technique, shown in Fig. 2.6., is a traditional in-situ non-intrusive diagnostics to measure the soot volume fraction quantitatively [128, 141]. This technique is a line-of-sight measurement. Here, a helium-neon (He-Ne) laser was used, which provided continuous laser beam at 632.8 nm wavelength. As such, this light extinction technique also relies on the Rayleigh absorption criterion discussed earlier.

The He-Ne laser beam was focused in the flame using a biconvex lens of focal length f=170 mm. A mechanical chopper was used to modulate the laser beam at 1000 Hz, and a photodetector was used to detect the signal. In order to prevent the noise in the signal due to the flame luminosity and the room light, a laser line interference filter centered at 632 nm was installed in front of the detector. The reference frequency of laser beam modulation from the mechanical chopper was sent to a lock-in-amplifier. Only the laser signal at 1000 Hz was processed by the lock-in-amplifier, rejecting any noise present in the signal. Then, the signal from the lock-in-

amplifier was read in a computer using the LabView software to determine the absorption ratio. A vertical translation stage with minimum step size of 0.01 mm was used to adjust the height of measurement in the flame. A horizontal translation stage with minimum step size of 0.01 mm was also used to scan the flame radially.

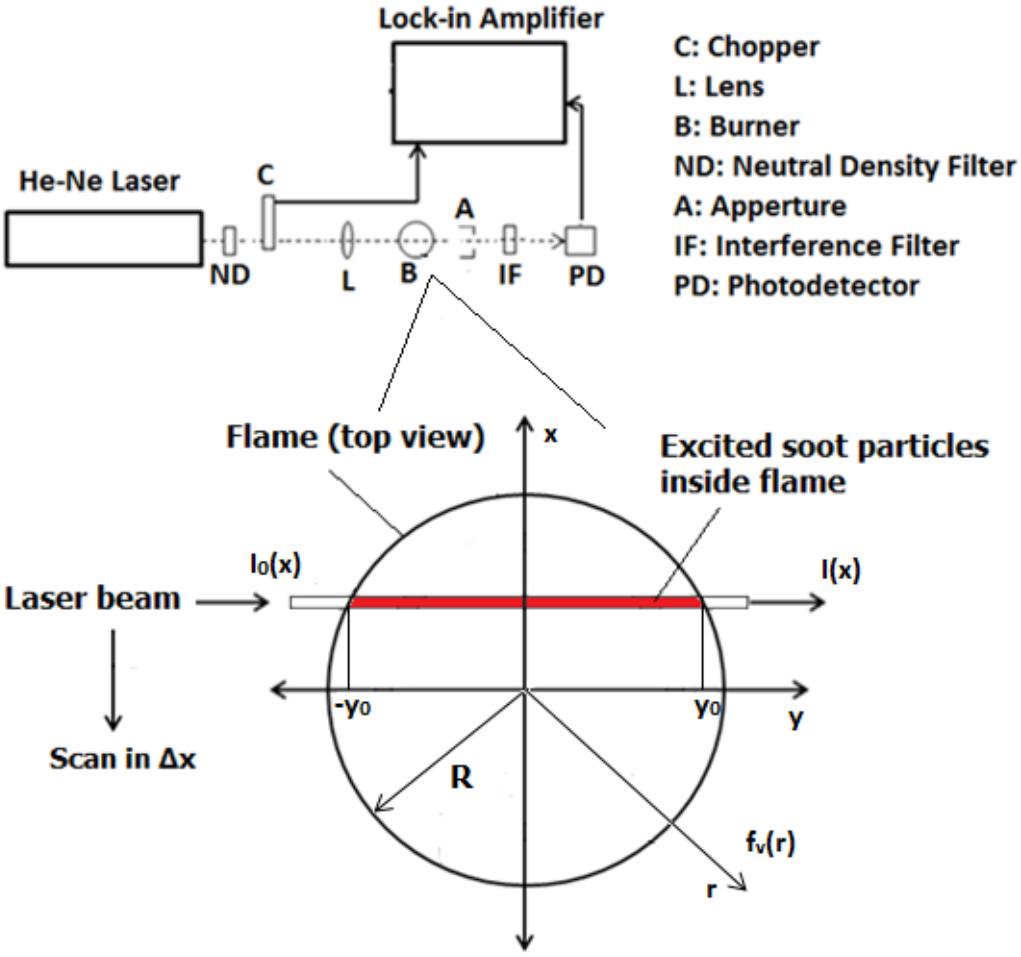

Figure 2.6: Schematic of experimental setup of counterflow non-premixed flame with LE laser diagnostic technique used for the calibration.

The absorption of laser light across the flame in the finite path length, ℓ, as per the Bouguer's Law, is given by Eq. (3):

$$\frac{I}{I_o} = e^{-K_{ext}\ell}, \quad (3)$$

where I_o is the intensity of the incident laser beam, I is the intensity of laser beam after absorption by soot particles, and K_{ext} is the extinction coefficient. As the scattering is small compared to the absorption in the Rayleigh limit, K_{ext} is approximated by the following expression:

$$K_{ext}(r) = K_{abs}(r) = \frac{6\pi E(m)}{\lambda} f_v(r). \quad (4)$$

In Eq. (4), $K_{abs}(r)$ is the absorption coefficient, λ is the laser beam wavelength, r is the radial distance from the center of the flame, and $E(m)$ is the function of refractive index of soot particles, m, as defined by Eq. (5):

$$E(m) = -Im\left(\frac{m^2-1}{m^2+2}\right). \quad (5)$$

Employing Abel's inversion to transform Eq. (4), a relationship for the local absorption coefficient and the soot volume fraction can be established as follows:

$$f_v(r) = \frac{\lambda}{6\pi^2 E(m)} \int_r^R \frac{d[ln(I(x)/I_o)]}{dx} \frac{dx}{\sqrt{x^2-r^2}}, \quad (6)$$

where x is along the optical path and R is the radius of the flame. The refractive index used for the current measurements is $m = 1.57 - 0.56i$, which is widely used in the literature e.g., [142, 143]. This refractive index has been validated against a wide range of fuels and flame environments [142-149]. Other refractive index values reported in the literature include $m = 1.90 - 0.55i$ [150] and $m = 1.75 - 1.03i$ [151]. Using these two refractive index values of [150] and [151], calculations based on Eq. (5) show that the value of $E(m)$ would differ by a factor of 0.74 and 1.436, respectively. In a study on oxygenated ester fuels [152], $m = 1.58 -$

$0.57i$ was used. Based on the refractive index value of [152], the value of $E(m)$ would differ by a factor of 1.008. Nevertheless, the soot formation ranking determined by using either of these refractive index values would be unaffected.

2.4 Planar laser induced fluorescence (PLIF) for the PAH measurements

For the PAH measurements, planar laser-induced fluorescence (PLIF) technique was used, involving a Nd:YAG-pumped dye laser (Continuum ND 6000) and a UV tracker (Continuum UVT-1), in addition to the equipments and instruments used for the LII measurements. The schematic for the present PAH-PLIF experimental setup is shown in Fig. 2.7. In the dye laser, the Rhodamine-590 dye was used, which has an emission peak wavelength at 560 nm. The grating in the dye laser was adjusted to 566 nm output, and then the UVT was used to frequency double the laser beam output from the dye laser to achieve a UV laser beam at 283 nm wavelength. Two UV cylindrical lenses, plano-concave (f = –25 mm) and plano-convex (f = 300 mm), were used to create a laser sheet.

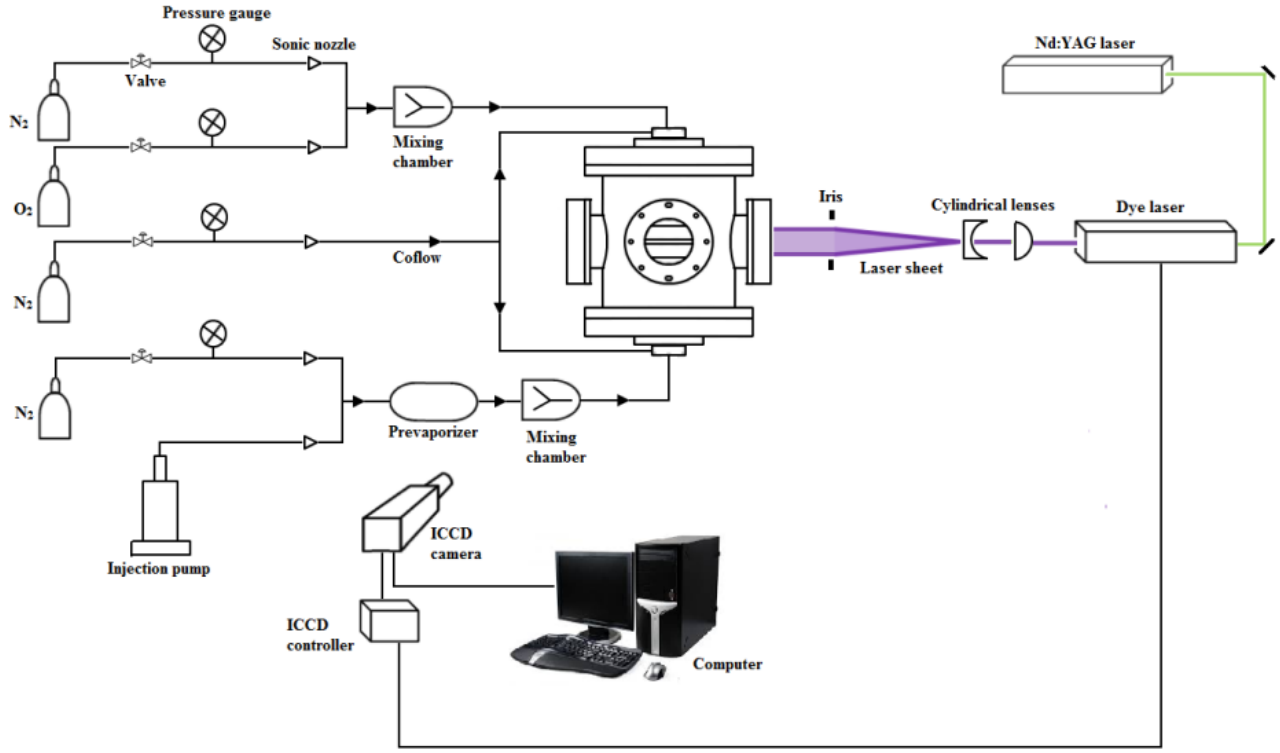

Figure 2.7: Schematic of experimental setup of counterflow non-premixed flame with PAH-PLIF laser diagnostic technique.

Since a relatively low laser fluence for the PAH-PLIF measurements was maintained at 250 mJ/cm^2 to avoid the incandescence of soot particles [73], it circumvented the noise due to the soot incandescence in the PAH-PLIF signal. In both the LII and PAH-PLIF techniques, the laser sheet was passed through the centerline between two opposed nozzles. In the LII measurements, the ICCD camera detected 450 nm signal that was part of the broadband radiation generated by the soot particles. Reasons to select the 450 nm detection wavelength for the LII experiments were delineated in [131]. Detection wavelenghts of 334 nm, 400 nm, 450 nm, and 492 nm were used in the PAH-PLIF experiments. Further details on mapping these detection wavelegths to the aromatic ring sizes of PAHs will be discussed in due course. In both the LII and PAH-PLIF experiments, 3 sets of 20 images were averaged to take the measurements. In these experiments all the filters used for detection were narrow band-pass filters (FWHM = ±10 nm), which ensured minimal interference in the detected signal due to the other noise sources. With the current optical setup, the spatial resolution was 0.0384 mm/pixel.

Since the LII technique used here has been described in detail elsewhere [131], the present focus is on the description of the PAH-PLIF technique for PAH measurements. The theoretical background behind the PAH-PLIF technique is as follows. The PAH molecules are known to have good absorption cross sections over a wide range of excitation wavelengths from UV to visible [153]. Upon absorbing the UV excitation provided by the lasers, these PAH molecules undergo ro-vibronic transitions from the electronic ground state (S_0) to electronic excited states (S_2 or higher). Then from these excited states, these PAH molecules relax to the electronic state S_1 by the internal conversion and the ro-vibrational relaxation processes. Further, these excited PAH molecules provide fluorescence by relaxing back to the ro-vibrational levels of S_0 [154, 155]. In addition, the emission wavelength from an excited PAH molecule depends on the

number of aromatic rings this molecule possesses, while the emission wavelength is larger for a molecule with higher number of aromatic rings [154-156]. It is also known that the emission characteristics of the PAH molecules do not vary for an excitation wavelength in the range of 265–297 nm [156]. Researchers have attempted to provide quantitative measurements for the PAHs with limited success, as it is difficult to make a spectral distinction between aromatics, with the same number of rings, but different chemical structures [155, 157], due to the broadband nature of emission spectra from these PAHs.

The optical diagnostic technique adopted here for the PAH measurements faces challenge as the signals of the PAH fluorescence and the LII overlap spectrally [155-159]. Moreover, the UV excitation used for the PAH-PLIF can be absorbed by the soot particles [155-159]. To resolve this, the following twofold steps were taken. First, the laser excitation energy was controlled to a low fluence to avoid the incandescence of the soot particles [73, 159]. As mentioned earlier, the UV laser fluence was kept at low level of 250 mJ/cm^2 in the present study. Second, the detection of the PAH fluorescence signal was accomplished by integrating the prompt fluorescence signal, in a short detection gatewidth of 30 ns, right after the absorption of the laser pulse. This detection gated width has been chosen based on the one used in the Refs. [73, 131, 159], which is selected by making a comparison with other detection gate widths. Since the fluorescence signal is short lived, hence compared to the LII signal, the shorter detection gatewidth avoids the noise due to the LII signal (if any). Furthermore, researchers have provided the spectral resolutions for the PAH molecules by grouping them according to the number of the aromatic rings. It has been shown that the signals of 2- and 3-aromatic ring PAHs (naphthalene, anthracene, and derivatives) attribute to a wavelength close to 330 nm [160-162]. Using several ethylene coflow flames with different partially-premixing levels, McEnally and Pfefferle [163] compared the PAH-PLIF

signals for naphthalene ($C_{10}H_8$) with its concentrations measured using the photoionization/time-of-flight mass spectrometer (PTMS), and demonstrated that the PAH-PLIF signals provide qualitative measurements of the naphthalene concentrations. To detect 2- and 3-ring aromatics, a detector of 334 nm wavelength was used in the current study. In addition, the detection wavelength of 400 nm has been known to correspond to the 4-aromatic ring (A_4) such as pyrene ($C_{16}H_{10}$) [164], and hence it was used to detect the 4-ring aromatics. The other two detection wavelengths of 450 nm and 492 nm qualitatively represent the larger ring PAH molecules [156, 165]. These wavelengths have not been directly related to the PAH ring sizes, as for the longer detection wavelengths the spectral separation of the fluorescence signals from large PAHs becomes complex [156, 160, 165]. It was observed in [158, 166-170] that the PAH fluorescence signal using the 500 nm detection was spatially closest to the LII signal. As such, in our study, a 492 nm detection wavelength represents large PAH molecules formed right before the soot particle formation, which will be demonstrated later.

For the PAH measurements at elevated pressure conditions, although the quenching effect would result in pressure broadening at elevated pressures, the PLIF measurements are used in this study for broader qualitative measurements as previously adopted by Menon [171]. Due to the lack of information on the quenching rate databases for the PAHs, quantitative measurements are not feasible [171]. The quantitative measurements of these PAHs are also limited due to the lack of information on the detection wavelengths to spectrally-resolve those species with the same number of aromatic rings, but different chemical structures [156].

2.5 Definitions of stoichiometric mixture fraction, strain rate and pressure-weighted strain rate

The stoichiometric mixture fractions, Z_{st}, defined as:

$$Z_{st} = \left(1 + \frac{Y_F W_{O_2} \nu_{O_2}}{Y_{O_2} W_F \nu_F}\right)^{-1} = \left(\frac{X_{O_2}}{W_L \nu_{O_2}}\right) / \left(\frac{X_{O_2}}{W_L \nu_{O_2}} + \frac{X_F}{W_0 \nu_F}\right), \quad (7)$$

for different mixture conditions are also listed in Table 2. In Eq. (7), Y_F is the mass fraction of fuel at the fuel stream boundary, Y_{O_2} is the mass fraction of O_2 at the oxidizer stream boundary, W_F and W_{O_2} are the molecular weights of fuel and O_2, respectively, ν_{O_2} and ν_F are the stoichiometric coefficients of O_2 and fuel, respectively, and W_L and W_0 are the average molecular weights of the mixtures at the oxidizer (z=L) and fuel (z=0) stream boundaries, respectively. In combustion theory, the mixture fraction is a normalized coupling function with the mixture fractions of 0 and 1 defining the oxidizer and fuel stream boundaries, respectively [172]. In the flame sheet limit, combustion is considered to be stoichiometrically concentrated and completed at the mixture fraction value of Z_{st}.

Soot formation is a rate-limiting process, and hence it depends on the strain rate that characterizes the residence time experienced by the reactants in the combustion zone of a counterflow non-premixed flame. A higher strain rate implies a shorter residence time experienced by the combustion reactions. In this study, since the nozzle-generated exit flow is plug-like, the global strain rate (K), based on the relation of Seshadri and Williams [173]:

$$K = \frac{2V_L}{L}\left(1 + \frac{V_0\sqrt{\rho_0}}{V_L\sqrt{\rho_L}}\right), \quad (8)$$

is used to represent the strain rate effect. In Eq. (8), V is the bulk velocity at the nozzle exit, ρ is the density, and the subscripts 0 and L represent the fuel (z=0) and oxidizer (z=L) stream boundaries, respectively. Equation (8) also takes the effects of varying density at two boundaries into account.

Since the effects of pressure on the soot formation process have also been investigated in this study, it is required to isolate the change in the overall flame structure due to the pressure

variation to make the comparisons. Kreutz and Law [174] has shown that the width of the mixing layer in the counterflow non-premixed arrangement scales as $(\rho K)^{-1/2}$, such that for a constant strain rate *K*, the change in ambient pressure will result in appreciable variation in the overall flame thickness (in terms of temperature and concentration profiles). Thus, in order to isolate the chemical effect of pressure variation from the effect of flame structure variation, the strain rate must be set such that the overall flame thickness remains approximately constant. This can be accomplished by the use of the pressure-weighted strain rate, as used experimentally in the work of Fotache *et al.* [175], and defined in Eq. (5) below:

$$K' = \frac{P}{P_o} K, \tag{9}$$

where K' is the pressure-weighted global strain rate, P is the chamber pressure, P_o is a reference pressure, taken throughout this work as 1 atm, and K is the global strain rate as defined in Eq. (8).

2.6 Computational specifications

The counterflow flames were simulated using the OPPDIF module in CHEMKIN-PRO [169], which is based on the plug-flow formulation of Kee *et al.* [170]. The counterflow flame model includes the GAS-PHASE KINETICS subroutine library and TRANSPORT package subroutines. Although a detailed soot modeling considering soot particle inception, coagulation, and growth, such as in Refs. [8, 78, 90], were not incorporated here, the computed spatially-resolved profiles of soot precursors (e.g., C_2H_2 and C_3H_3) using the literature reaction mechanisms for butane and butanol isomers would still provide insight into the sooting propensity ranking for the fuels of interest. In addition, these literature reaction mechanisms

were used to make a comparison of the reaction pathways of fuel breaking and key soot precursors such as C_2H_2 and C_3H_3.

To simulate butane and butanol flames for soot formation process, detailed in Chapter 3, three mechanisms were used. To simulate butane flames, the chemical kinetic models of USC Mech II [1] and Merchant *et al.* [3] were used. The USC Mech II [1] consists of 111 species and 784 reactions, and is relevant to high-temperature oxidation of hydrogen, carbon monoxide, and C_1−C_4 hydrocarbons. The chemical kinetic model of Merchant *et al.* [3] consists of 372 species and 8723 reactions, and was also used for both butane and butanol flame simulations. Another chemical kinetic model used for simulating counterflow flames of butanol isomers was that of Sarathy *et al.* [2], consisting of 426 species and 2335 reactions.

The OPPDIF simulations for the PAH formation for butane and butanol flames which are detailed in Chapter 4, were performed by adopting the Primary Reference Fuels + PAH + Alcohols + Ethers mechanism (Version POLIMI_PRF_PAH_ALCOHOLS_ETHERS_HT_1412, December 2014) of the Chemical Reaction Engineering and Chemical Kinetics (CRECK) Modeling Group [4-7]. This mechanism was employed in the current study because it can predict the formation of soot precursors up to the four-ring aromatics for butane and butanol isomers. The mechanism includes 317 species and 12353 reactions, and is referred as the POLIMI mechanism hereafter. While a detailed soot modeling considering the soot particle inception, coagulation, and growth processes was not incorporated herein, the computed spatially-resolved profiles of those PAHs included in the POLIMI mechanism would still provide insight into the PAH/soot formation for the C_4 fuels investigated.

The OPPDIF simulations at elevated pressures for ethylene counterflow non-premixed flames were performed by adopting a reaction mechanism for ethylene combustion and PAH

formation, growth, and oxidation. The mechanism was taken from Wang and Frenklach [8], including the modeling of Wang *et al.* [176-178] for aromatic formation, growth, and oxidation; this mechanism is denoted the WF-PAH mechanism hereafter. The WF-PAH mechanism includes 99 species and 533 reactions, and can predict the formation of soot precursors up to the four-ring aromatics. While a detailed soot modeling considering the soot particle inception, coagulation, and growth processes was not incorporated herein, the computed spatially-resolved profiles of those PAHs included in the WF-PAH mechanism [8] would still provide insight into the PAH/soot formation for the ethylene non-premixed flames investigated here.

Chapter 3: Soot formation in butane and butanol isomer flames

3.1 Introduction

Counterflow non-premixed flame is known to provide an aerodynamically-clean and well-characterized configuration for experiments and simulations. With judicious mixture compositions for the fuel and oxidizer streams, the resulting non-premixed flame can be situated at different locations relative to the stagnation surface so that it is possible to separate the processes of soot formation and oxidation for further characterization. In this study, the sooting behavior of butane and butanol flames have been characterized and determined by measuring their spatially-resolved soot volume fraction profiles.

Previously, Camacho *et al.* [71] studied the sooting characteristics of *n*-butane, *iso*-butane, *n*-butanol, and *iso*-butanol in a burner stabilized stagnation premixed flame configuration to investigate the impact of fuel bound hydroxyl group, as well as the effect of fuel structure. They found that under the same C/O ratio, butanol flames nucleate sooner than butane flames. It was concluded by Camacho *et al.* [71] that the sooting behavior in the premixed flames at the nucleation stage can be predicted by the soot precursors, while at the mass growth stage the relationship between the predicted benzene concentration and the sooting behavior becomes less clear, considering the complexity of soot formation process. McEnally and Pfefferle [179] studied the sooting behavior of butanol isomers by doping 3500 ppm of each of butane and butanol isomers in a coflow methane-air non-premixed flame. They found that benzene formation is directly linked to propargyl (C_3H_3) species concentration. It is noted that both the studies of Camacho *et al.* [71] and McEnally and Pfefferle [179] have focused on the incipient

soot formation process. To our knowledge, none of the literature studies have been conducted to investigate the soot formation of these butanol isomers in a non-premixed counterflow flame configuration, and all the butanol isomers have not been compared with the butane isomers in such a sooting flame configuration.

Various techniques of soot measurement, such as gravimetric sampling, condensation particle counters, differential mobility particle sizer, and transmission electron microscopy using thermophoretic sampling, have been developed [180]. These techniques rely on the collection of soot particles manually, examining them by their physical parameters, such as weight, particle mobility in an electric field, etc., and the use of a microscope. As such, these sampling techniques are time consuming and some of them are intrusive. Faster, non-intrusive optical techniques have been developed to characterize soot formation in combustion. Two such laser-based techniques of soot particle measurements, namely Laser Induced Incandescence (LII) and Light Extinction (LE), have been used for the quantitative soot volume fraction measurements. In particular, the use of planar LII imaging in conjunction with line-of-sight LE calibration technique provides very fast, quantitative, and spatially-resolved soot volume fraction measurements.

3.2 LII signal calibration

The calibration for the present LII signal was performed using counterflow non-premixed ethylene and *n*-butanol flames. The fuel stream was composed of a fuel/N_2 mixture with the fuel mole fraction of X_F=0.28 for the ethylene flame and X_F=0.29 for the *n*-butanol flame, while the O_2/N_2 oxidizer stream for both the flames was maintained at an oxygen mole fraction of

X_{O_2}=0.90. For the experimental conditions, a yellow luminous sooting zone was observed towards the fuel nozzle followed by a thin blue flame towards the oxidizer nozzle.

Figure 3.1(a) plots the radial profiles of soot volume fraction at five different axial locations (z) from the bottom fuel nozzle for the ethylene flame and Fig. 3.1(b) shows such profiles at three axial locations for the *n*-butanol flame. In Fig. 3.1, the solid symbols/black lines represent the LE measurements using the abel's inversion and the hollow symbols/gray lines represent the LII signals. Firstly, the LII signal, averaged over 20 images, was compared with the quantitative measurement of soot volume fraction at the 'Calibration Point' indicated in Fig. 3.1 (a), with the comparison made for z=3.35 mm, for the ethylene flame. With the similar process for the *n*-butanol flame, the LII signal was also compared with the quantitative measurement of soot volume fraction at the 'Calibration Point' indicated in Fig. 3.1(b), with the comparison made for z=4.84 mm. Calibration factors were calculated with these comparisons. The calibration factor values were 3.05×10^8 and 3.11×10^8 for the ethylene and *n*-butanol flames, respectively. The similarity of these two values indicates that the experiments compare well for non-oxygenated (ethylene) and oxygenated (*n*-butanol) flames. Using the calibration factor for each flame, the quantitative values for the LII signals at other (r, z) locations were then calculated. It can be seen from Fig. 3.1 for both the ethylene and *n*-butanol flames that the radial distributions of soot volume fractions determined from both the LII and LE techniques compare well for all the other axial locations. Another aspect of comparing the radial distribution is its symmetry, thereby suggesting that the variation in optical properties of soot is deemed insignificant as the soot volume fraction distributions compare well.

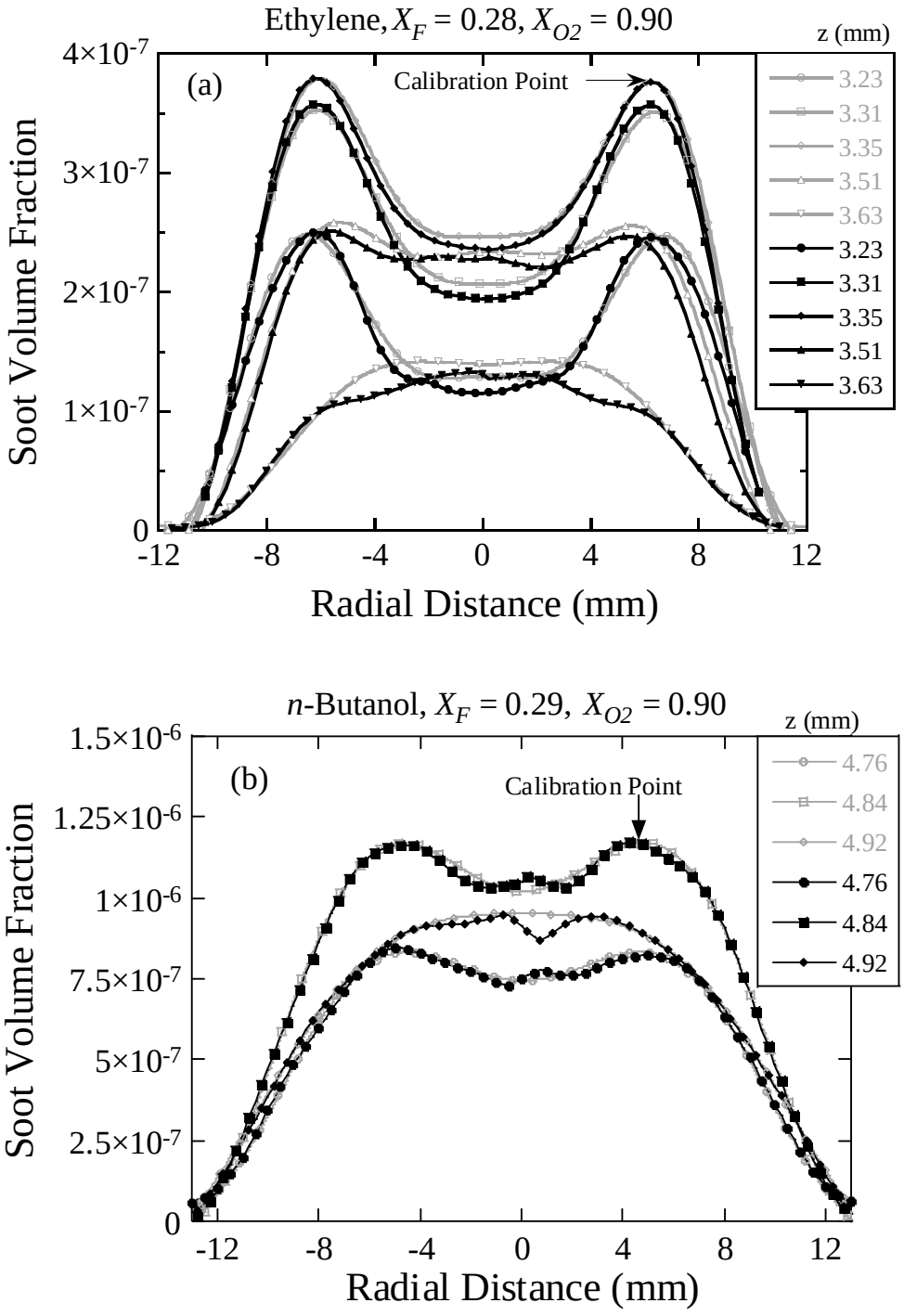

Figure 3.1: Soot volume fraction profile comparison of LII and LE measurements for (a) a counterflow ethylene flame at five different heights and (b) a counterflow *n*-butanol flame at three different heights, where *z* represents the distance from the fuel nozzle. Solid symbols/black

lines for LE measurements using abel's inversion and hollow symbols/gray lines for LII measurements.

With the above-mentioned calibration, the use of LII technique facilitates the mapping of soot volume fraction distribution profiles as shown in Fig. 3.2 for the ethylene flame. It is seen that the overall soot volume fractions increase from z=2.99 mm to z=3.35 mm (cf. Fig. 3.2(a)), and then decrease from z=3.35 mm to z=3.71 mm (cf. Fig. 3.2(b)). As such, Fig. 3.2 (a) represents the soot inception and growth zone, while Fig. 3.2 (b) represents the soot oxidation zone. At the onset of soot formation, more soot is formed at the radially outward locations than the center, as shown in Fig. 3.2 (a). This is due to longer residence time in the radially outward locations than the center. Moreover, this higher residence time provides more time to the soot formation and growth process. Figure 3.2 (a) also shows that the amount of soot formed increases while moving upwards (towards the flame), both at the center and radially outward locations. Further moving upwards from z=3.35 mm to z=3.47 mm, Fig. 3.2 (b) shows that although the amount of soot continues to grow near the center, the amount of soot decreases at the radially outward locations. This is due to less availability of fuel in the radially outward direction as it is consumed rapidly and possibly diluted by the shroud flow. Then moving upwards from z=3.51 mm, the overall soot volume fractions decrease due to oxidation, both at the center and radially outward locations.

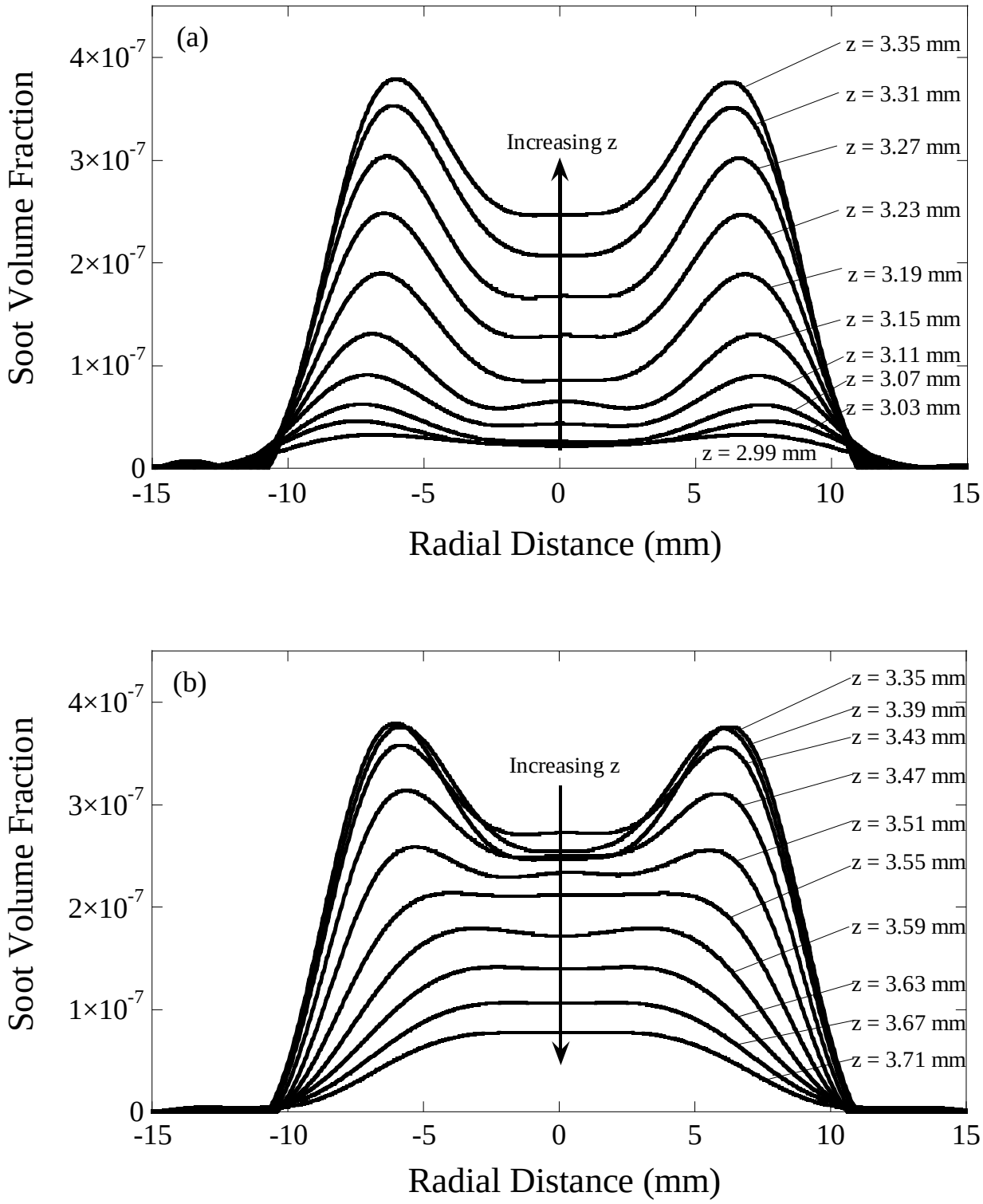

Figure 3.2: Soot volume fraction distribution in a counterflow ethylene flame: (a) soot formation and growth zone (b) soot decomposition and oxidation zone, where *z* represents the distance from the fuel nozzle.

Similar trend of soot volume fraction distributions in the counterflow non-premixed configuration as Fig. 3.2 was also observed for other fuels investigated in this study. However, only the axial variations of soot volume fraction along the centerline will be presented and compared in the following discussions.

3.3 Soot volume fraction results with fuel loading, oxygen level, and strain rate variation

In order to assess the molecular structure effects on soot formation in butane and butanol flames, soot volume fraction profiles for these flames were measured and compared in the current non-premixed counterflow burner facility. The exit temperatures of the fuel and oxidizer nozzles were maintained at T_{in}=400 K. Moderately sooting flame conditions were chosen in this study, as the LII measurement technique is not suitable for heavily sooting flames. This is because that under heavily sooting conditions the laser fluence threshold cannot be maintained for the entire measurement domain due to the absorption of the laser power by the soot particles. It is also noted that for lightly sooting flames, the sparse density of soot particles results in weaker LII signal strength, which would not be sensitive enough for the LII measurements. Based on the above considerations, experimental conditions of X_F =0.21−0.29 and X_{O_2}=0.70−0.90 for the fuel and oxidizer streams, respectively, were employed.

Table 2 lists the calculated adiabatic flame temperatures (T_{ad}) for all the tested fuels at varying X_F and X_{O_2} using the thermodynamics database of Merchant *et al.* [3]. While the reaction kinetics of fuel pyrolysis and oxidation, aromatics formation, PAH mass growth and oxidation, and soot chemistry are temperature sensitive, for a given set of X_F and X_{O_2} the slight differences in T_{ad}, within the isomers and between butane and butanol, are not expected to have an impact on the soot formation processes in different fuels. For all the mixture compositions

investigated herein, Z_{st}<0.5, as shown in Table 2, and hence the "flame sheets" are all situated on the oxidizer side of the stagnation plane. Although Z_{st} has been shown to have a significant effect on soot formation [181-185], for a given set of X_F and X_{O_2} the difference in Z_{st} due to the small differences in molecular weights and stoichiometric coefficients for butane and butanol is not significant. Therefore, when comparing the sooting propensity, the effect of Z_{st} on the soot volume fraction is not considered in the present study.

Table 2: Calculated adiabatic flame temperatures (T_{ad}) and stoichiometric mixture fractions (Z_{st}) for the mixture conditions investigated in the present study.

Fuel Stream		**Oxidizer Stream**		**Adiabatic Flame Temperature T_{ad} (K)**						**Stoich. Mixture Fraction Z_{st}**	
X_F	X_{N_2}	X_{O_2}	X_{N_2}	*n*-butane	*iso*-butane	*n*-butanol	*iso*-butanol	*sec*-butanol	*tert*-butanol	butane isomers	butanol isomers
0.21	0.79	0.90	0.10	2944	2941	2898	2895	2892	2885	0.417	0.460
0.22	0.78	0.90	0.10	2949	2947	2904	2901	2898	2890	0.408	0.451
0.23	0.77	0.90	0.10	2955	2952	2910	2907	2904	2896	0.399	0.443
0.24	0.76	0.90	0.10	2961	2958	2915	2912	2910	2902	0.391	0.436
0.25	0.75	0.90	0.10	2966	2964	2921	2918	2915	2908	0.384	0.429
0.26	0.74	0.90	0.10	2972	2969	2927	2924	2921	2914	0.376	0.422
0.27	0.73	0.90	0.10	2978	2975	2933	2930	2927	2920	0.369	0.415
0.28	0.72	0.90	0.10	2984	2981	2939	2936	2933	2926	0.363	0.409
0.29	0.71	0.90	0.10	2989	2987	2945	2942	2939	2932	0.357	0.404
0.29	0.71	0.80	0.20	2958	2955	2915	2912	2909	2902	0.333	0.379
0.29	0.71	0.70	0.30	2919	2916	2877	2874	2872	2864	0.307	0.351

The soot volume fraction profiles along the centerline of various flames at the experimental conditions of X_F=0.29, X_{O_2}=0.90, and K=57 s^{-1} (V_0=V_L=14.9 cm/s) are presented and compared in Fig. 3.3. In Fig. 3.3 (a) the soot profiles for all the fuels are shown with a y-axis scale of 10^{-5}– 10^{-4}, while in Fig. 3.3 (b) these are shown using a y-axis scale of 10^{-7}– 10^{-6} so that the profiles for *n*-, *iso*-, and *sec*-butanol can be more prominent. In general, the soot volume fraction

profile can be divided into three zones, namely inception, growth, and oxidation for soot. The soot inception zone exists towards the fuel side, where due to the higher concentrations of soot precursors, initial single ring aromatics formation takes place. Further growth in soot is due to various parallel pathways of soot formation and growth, such as aromatic condensation, hydrogen-abstraction/carbon-addition (HACA), etc. The maximum soot volume fraction in Fig. 3.3 is attained near z=4.85 mm from the fuel nozzle. After the peak, in the soot oxidation zone, there is a decrease in the soot volume fraction along the centerline, as the soot particles are oxidized due to high temperature.

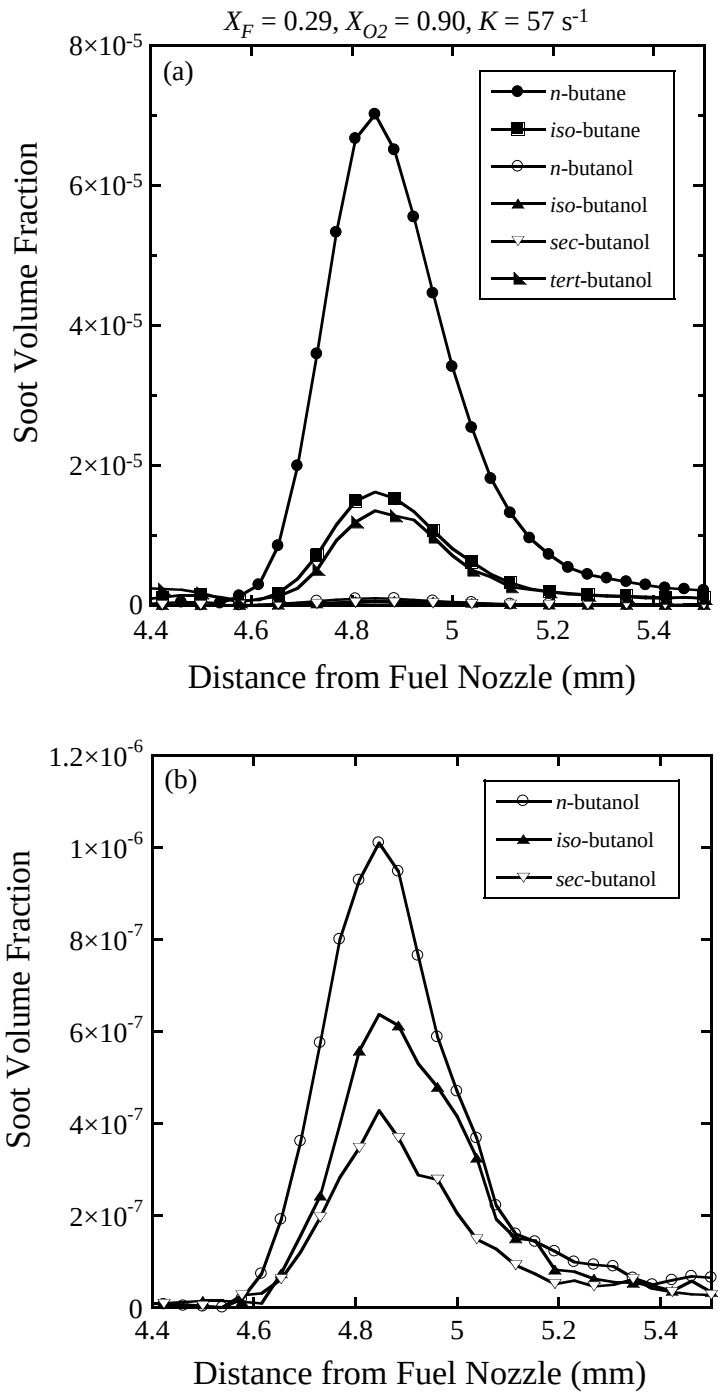

Figure 3.3: Spatial profiles of soot volume fraction measurements along the centerline for butane and butanol isomers: (a) all the butane and butanol isomers (b) *n*-butanol, *iso*-butanol, and *sec*-butanol isomers on an appropriate scale. Conditions: X_F = 0.29, X_{O2} = 0.90, and K = 57 s^{-1}.

The sooting propensity for counterflow non-premixed flames can be ranked based on the maximum soot volume fraction along the centerline of the flame [152]. As such, the sooting propensities of butane and butanol isomers can be inferred from Fig. 3.3 as *n*-butane > *iso*-butane > *tert*-butanol > *n*-butanol > *iso*-butanol > *sec*-butanol. In previous studies of [71, 179, 186-189], the sooting propensities were defined by the measurements of the incipient soot particles or the sooting limits. These studies generally noted a higher sooting tendency for butanols than butanes, as well as a higher sooting tendency for the branched chain isomers than the straight chain isomers. In addition, such observations at the incipient stage were found to be correlated with the tendency of fuel to form soot precursors of acetylene and propargyl. In the current study, sooting propensity is defined by comparing the maximum soot volume fractions in moderately sooting flames involving complex soot growth pathways, such as soot particle nucleation, surface reactions, coagulation, and oxidation [76, 190-195]. Based on the flame configuration (e.g., premixed versus non-premixed combustion or counterflow non-premixed versus coflow flames), the sooting behaviors of fuels may also change [196]. Due to the complexities involved with the soot formation process, the incipient soot formation stage may not be the rate limiting process [197-200], and hence the difference in sooting propensity ranking.

With X_{O_2}=0.90 and K~57 s^{-1} (V_0=V_L=14.9 cm/s), Fig. 3.4 further compares the sooting propensities for butane and butanol isomers by plotting the maximum soot volume fraction along the centerline as a function of X_F varying from 0.21 to 0.29. The error bars are plotted based on twice the standard deviation of the repeated measurements. For all the fuels investigated, it is observed that the maximum soot volume fraction increases as X_F is increased, while keeping X_{O_2} and K fixed. The increase in the fuel mole fraction increases the amount of soot precursors and hence an increased soot volume fraction. Under the present experimental conditions, the

observed sooting propensity ranking remains the same as in Fig. 3.3; however the slopes for different fuels shown in Figs. 3.4 vary. Since the butane isomers have higher sooting propensity than butanol isomers, this difference can be attributed to the presence of hydroxyl group (-OH) in butanol isomers. Within the isomers, the sooting propensity differs and that can be attributed to the structural differences in isomers. Those molecular structural effects on soot formation will be discussed in due course.

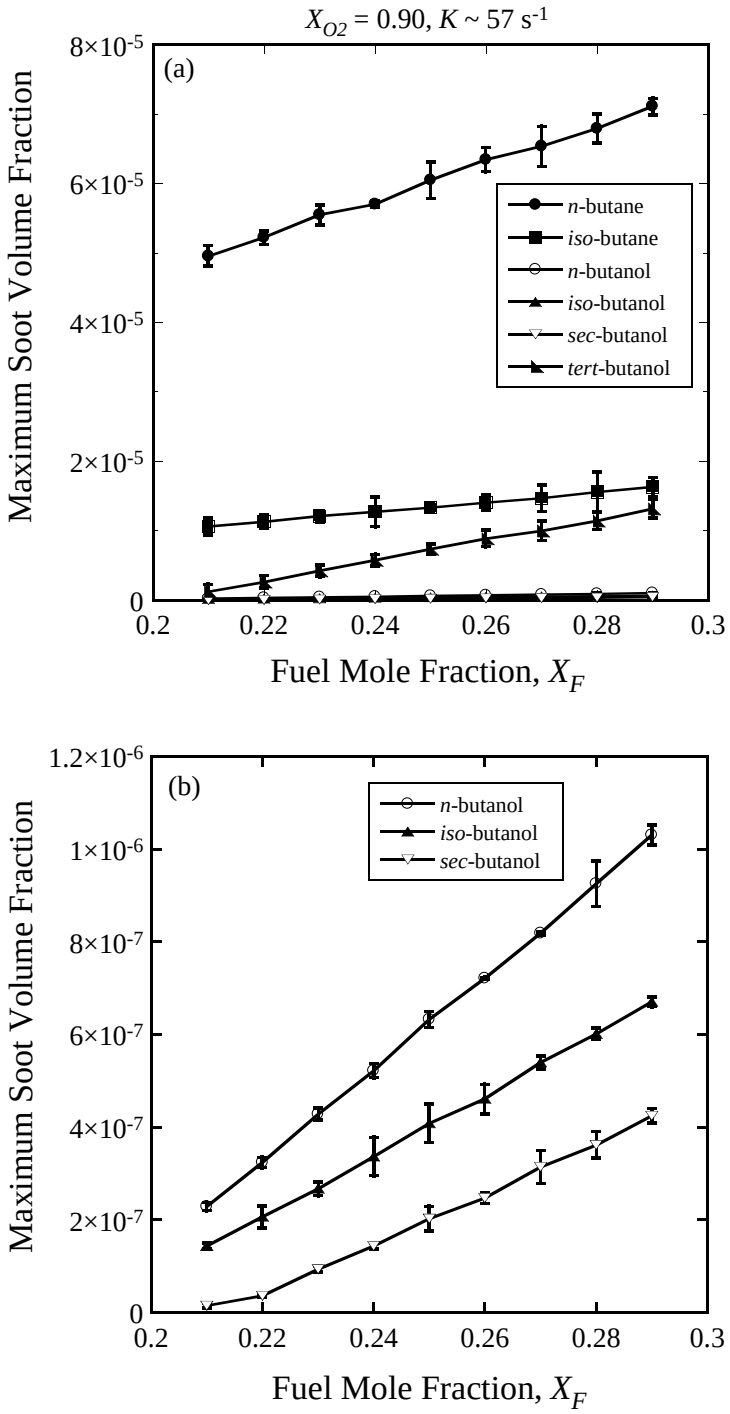

Figure 3.4: Maximum soot volume fraction measurements along the centerline for varying fuel mole fractions: (a) all the butane and butanol isomers (b) *n*-butanol, *iso*-butanol, and *sec*-butanol isomers on an appropriate scale. Conditions: X_{O2} = *0.90*, and K = 57 s^{-1}. Lines are connected to guide the discernment.

In Fig. 3.5 the effect of strain rate in the sooting zone for *n*-butanol is shown for X_F=0.29, X_{O_2}=0.90, and K=32−94 s^{-1} (V_0=V_L=8.3–24.8 cm/s), by plotting and comparing the soot volume fraction profiles along the centerline of the flames. As expected, both the sooting zone thickness and the overall soot loading decrease with increasing strain rate due to the reduction in characteristic residence time within the flame. Although not shown here, similar strain rate effects were also observed for other fuels. In Figs. 3.6(a) and 3.6(b), the maximum soot volume fractions along the centerline at varying strain rates are shown for the butane and butanol isomers. Again, the experimental conditions were kept at X_F=0.29 and X_{O_2}=0.90. It is seen from Figs. 3.6 that the maximum soot volume fraction decreases with an increase in strain rate for all the fuels. Within the same isomeric class, it is of interest to note that the fuels exhibit disproportionate decrease in maximum soot volume fraction with an increase in strain rate.

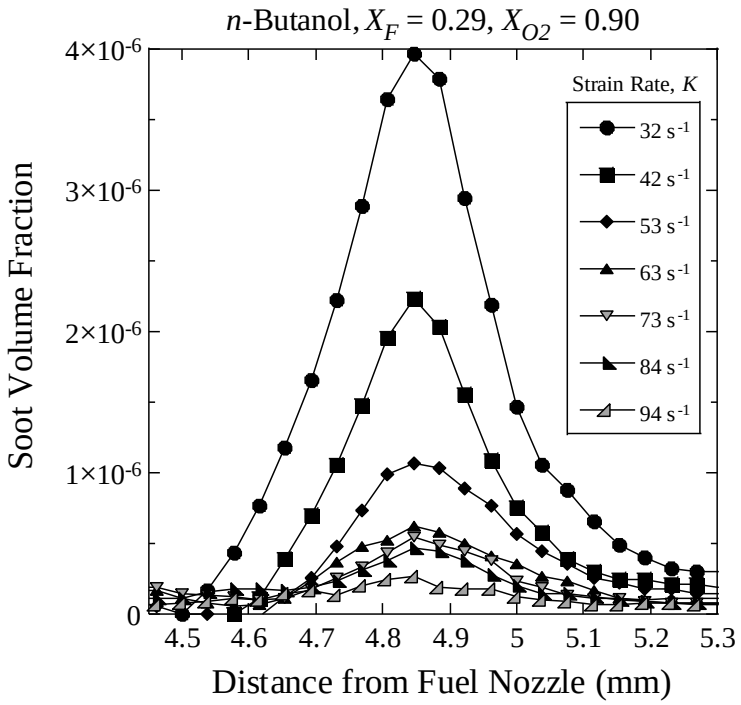

Figure 3.5: Strain rate effect on soot volume fraction profile along the centerline for *n*-butanol flames. Conditions: X_F = 0.29 and X_{O2} = 0.90.

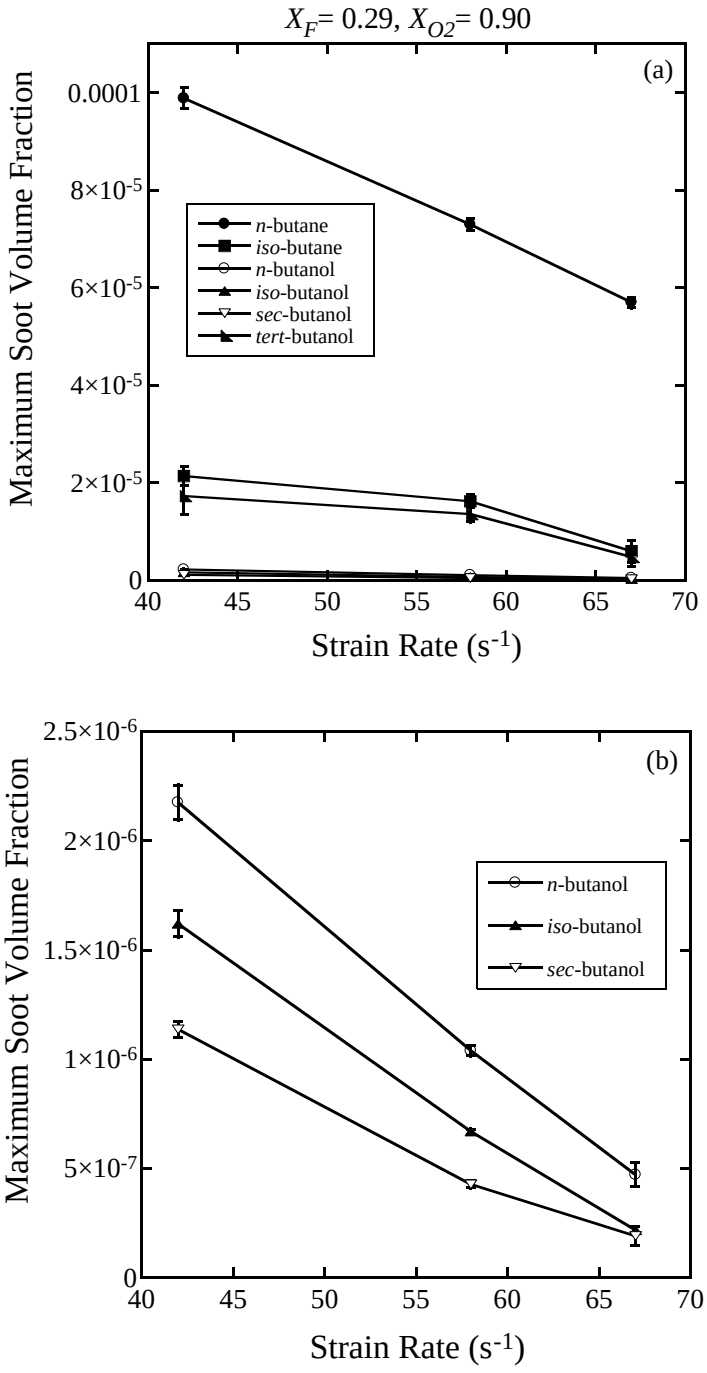

Figure 3.6: Strain rate effect on maximum soot volume fraction along the centerline for butane and butanol isomers: (a) all the butane and butanol isomers (b) *n*-butanol, *iso*-butanol, and *sec*-butanol isomers on an appropriate scale. Conditions: X_F = 0.29 and X_{O2} = 0.90. Lines are connected to guide the discernment.

Effects of change in oxygen mole fraction in the oxidizer stream on soot formation were also measured. Figure 3.7 shows and compares the soot volume fraction profiles along the centerline of the *n*-butanol flames for X_F=0.29 and X_{O_2}=0.70−0.90. As listed in Table 2, the Z_{st} values for X_{O_2} of 0.70, 0.80, and 0.90 are 0.351, 0.379, and 0.404, respectively. An increase in X_{O_2} leads to an increase in Z_{st}, indicating that the flame shifts away from the oxidizer boundary and towards the stagnation plane. The shift in flame location results in a shift in peak temperature location, which causes the location of maximum soot volume fraction to shift towards the fuel boundary with an increase in X_{O_2}. In addition, while the overall thicknesses of the sooting zone are comparable because of the same V_0=V_L=14.9 cm/s and the resulting similar strain rate values (K=57−60 s^{-1}), Fig. 3.7 shows a slight increase of the maximum soot volume fraction with increasing X_{O_2}.

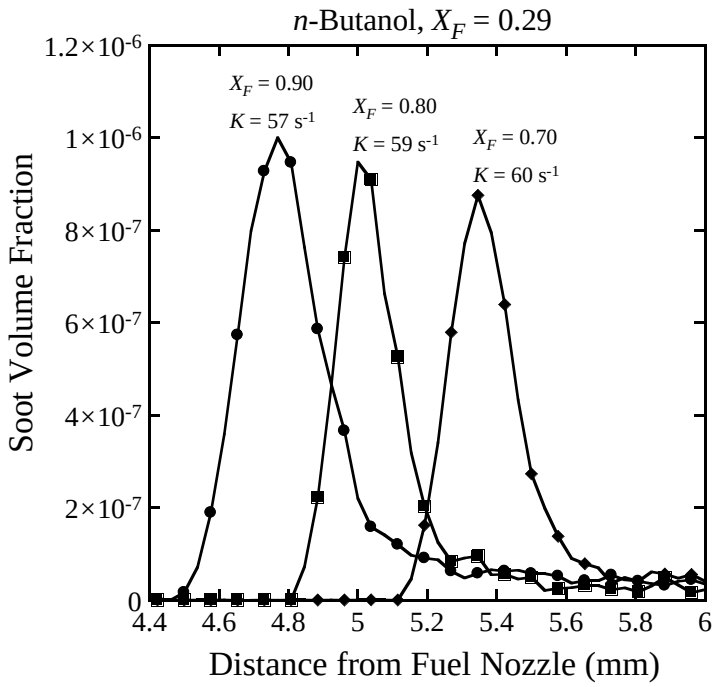

Figure 3.7: Oxygen mole fraction effect on soot volume fraction profile along the centerline for *n*-butanol flames with X_F = 0.29.

Figure 3.8 demonstrates the variations of maximum soot volume fraction along the centerline with X_{O_2} for these isomer fuels. Again, for clarity, in Fig. 3.8(b) *n*-, *iso*-, and *sec*-butanol are shown which produce soot on a smaller scale and all the isomers are shown in Fig. 3.8(a). The experimental conditions investigated were for a fixed fuel mole fraction of X_F=0.29 and varying oxygen mole fractions from 0.70 to 0.90. For all the fuels with an increase in X_{O_2}, an increase in the maximum soot volume fraction is observed. As shown in Table 2, the increase in X_{O_2} from 0.70 to 0.90 leads to an increase in T_{ad} by ~70 K, thereby facilitating the fuel pyrolysis to increase the amount of soot precursors and promote soot growth mechanisms. In addition, it can be seen from Fig. 3.8 that the increase in the maximum soot volume fraction for these fuels have a disproportionate response to the change in X_{O_2}. Such a fuel specific sooting response to the increase in oxygen mole fraction is expected to be related to different fuel breakdown pathways that are likely caused by the structural effects due to different bond strengths within isomers and the presence of the hydroxyl functional group.

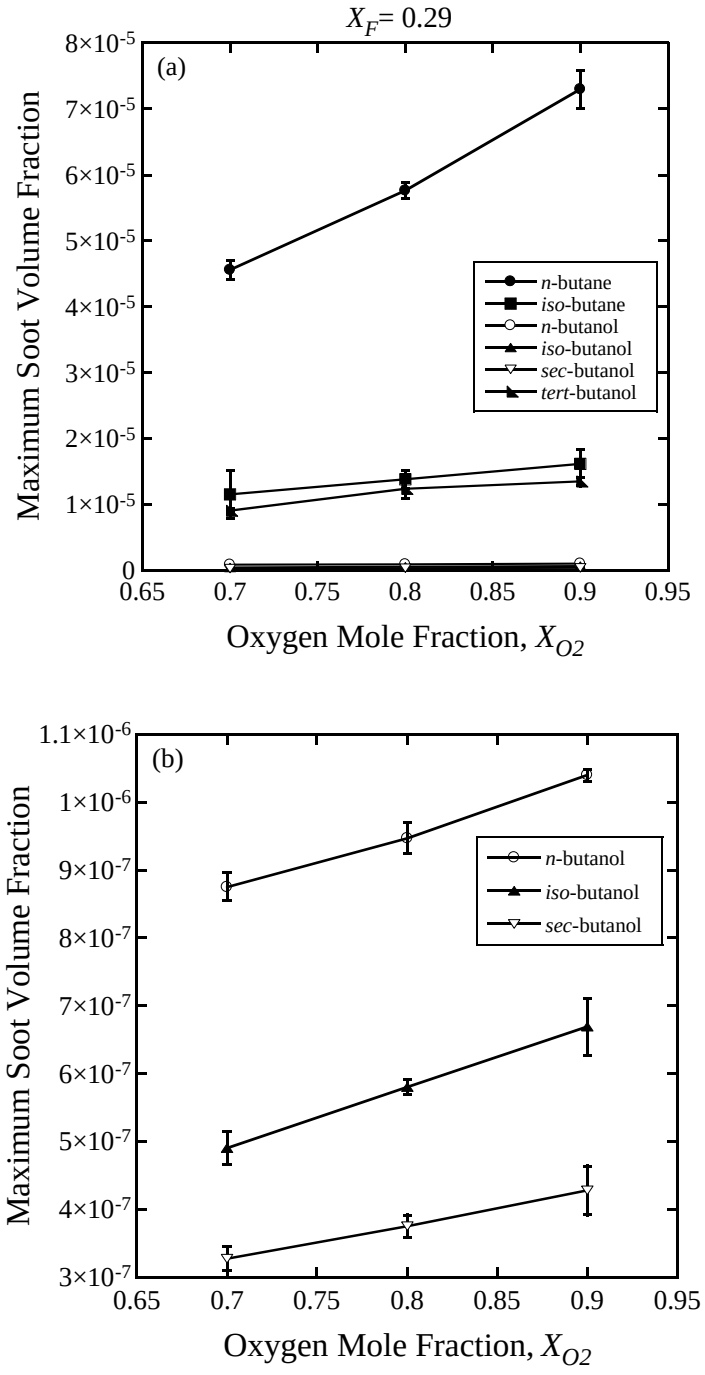

Figure 3.8: Oxygen mole fraction effect on maximum soot volume fraction along the centerline for butane and butanol isomers with X_F = 0.29: (a) all the butane and butanol isomers (b) *n*-butanol, *iso*-butanol, and *sec*-butanol isomers on an appropriate scale. Lines are connected to guide the discernment.

3.4 Isomeric structure effects on soot formation

It is established that the soot formation process is dependent on the gas phase chemistry of the fuel, as the soot precursors such as acetylene (C_2H_2) and propargyl (C_3H_3) play important roles in soot inception and growth chemistry. In addition, it is widely accepted that soot growth is a complex process of competing reactions between HACA and aromatic condensations. Moreover, the formation of soot precursors depends on the intermediate species formed during the fuel breaking process.

To understand the effect of the presence of hydroxyl (-OH) group in butanol isomers on sooting propensity, a comparison is made between butane and butanol isomers. Experimental results of Fig. 3.4 show that under the investigated conditions butane isomers have a higher sooting tendency than butanol isomers. As the butane isomers do not contain an oxygen atom, the initial decomposition of butane isomers produces intermediates, such as ethyl, propyl, butyl, *iso*-butyl radicals. The chemical structures for some intermediate species are given in Appendix. Since these intermediate species do not contain an oxygen atom, further decomposition of these intermediate results in butene, propene, and ethylene formation. Butene, propene, and ethylene easily convert into soot precursors such as acetylene and propargyl [179]. Longer chain species like butene and propene are more likely to form propargyl, whereas the shorter chain species like ethylene mostly forms acetylene [179]. On the other hand, due to the presence of a hydroxyl group, a substantial amount of butanols decomposes to form oxygenated intermediate species. These oxygenated intermediates further decompose to form aldehydes and ketones. As compared to the butene, propene, and ethylene, aldehydes and ketones are relatively stable intermediates, thereby producing less soot precursors. From the initial steps of fuel breaking, it can be inferred that the route taken to form soot precursors by butane and butanol isomers would differ.

Different fuel breaking pathways have been observed experimentally to lead to differences in incipient soot particle formation e.g. [71, 179].

Strong structural effects within the butane and butanol isomers were observed in the present experiments. Figure 3.4(a) shows that *n*-butane has higher sooting propensity than *iso*-butane. Initial fuel breaking of *n*-butane due to direct decomposition and H-abstraction produces methyl, ethyl, propyl, and butyl radicals. On the other hand, initial breaking of *iso*-butane takes a different route in comparison to *n*-butane, and produces methyl, propyl, and *iso*-butyl radicals by direct decomposition and H-abstraction. Since different initial fuel decomposition pathways are expected to lead to the dissimilar amount of soot precursors, there could be two possible reasons of *n*-butane exhibiting the greater sooting propensity. One of the possibilities is that *n*-butane overall forms substantially larger amount of soot precursors than *iso*-butane. Another possibility is that either of the HACA or propargyl recombination is highly competitive for *n*-butane. To validate these possibilities further investigations would be required, such as tracking the pathways of PAH growth or direct measurements of acetylene and propargyl precursors.

As per our experimental results in Fig. 3.4, amongst all the butanol isomers, the sooting propensity ranking from the highest to the least follows *tert*-butanol, *n*-butanol, *iso*-butanol, and *sec*-butanol. A closer look at the initial decomposition pathways for these fuels suggests that these isomers would produce dissimilar amount of soot precursors. One of the pathways of fuel breaking of *tert*-butanol is through the complex fission to eliminate H_2O, as the hydroxyl group in *tert*-butanol has nine neighboring hydrogen atoms available to form complex bonds [179]. In the complex fission process the dissociation of fuel occurs by breaking and forming of multiple bonds within the fuel [179]. The result of a complex fission process is to form *iso*-butene intermediates. Other fuel breaking pathways for *tert*-butanol are through direct decomposition

and H-abstraction to form the methyl, 2-hydroxy-2-methyl-propyl, *tert*-butoxy, and 1-hydroxy-1-methyl-ethyl radicals. Most likely, the pathway of the soot precursor formation for *tert*-butanol emanates from *iso*-butene, which converts easily into propargyl [28]. See the Appendix for the chemical structures of some intermediate species. In contrast to *tert*-butanol, *n*-butanol takes completely different initial fuel breaking pathways. Direct decomposition and H-abstraction are the major initial fuel breaking pathways for *n*-butanol. After the first step of fuel breaking, it produces methyl, ethyl, propyl, 2-hydroxy-ethyl, 3-hydroxy-propyl, 1-hydroxy-methyl, 1-butene, 3-hydroxy-1-methyl-propyl, 4-hydroxy-butyl, 1-hydroxymethyl-propyl, and 4-hydroxy-butyl. Since *iso*-butanol has branched structure similar to *tert*-butanol, the complex fission process for this isomer is one of the fuel breaking possibilities which results in *iso*-butene formation [179]. However, unlike *tert*-butanol, *iso*-butanol has five neighboring hydrogen atoms to form a complex bond so the fuel breaking pathways for these two isomers differ. Apart from complex fission, the fuel breaking pathways for *iso*-butanol are through direct decomposition and H-abstraction. Initial breaking of *iso*-butanol through these pathways results in methyl, 2-hydroxy-1-methyl-ethyl, 1-methyl-ethyl, 1-hydroxy-methyl, 3-hydroxy-2-methyl-propyl, 2-hydroxy-1-methyl-ethyl, and 1-hydroxy-2-methyl-prophyl radicals. Lastly, the availability of one neighboring hydrogen atom provides a complex fission pathway for *sec*-butanol to form 2-butene and 1-butane intermediates [179]. Other breaking pathways for *sec*-butanol are also direct decomposition and H-abstraction. These pathways lead to methyl, ethyl, 1-hydroxy-ethyl, 2-hydroxy-2-methyl-ethyl, 3-hydroxy-3-methyl-propyl, 2-hydroxy-1-methyl-propyl, 2-hydroxy-butyl, and 1-hydroxy-1methyl-propyl radical formation. Hence, from these fuel breaking pathways it is expected that the amount of soot precursors formed by these isomers would not be

similar, and the soot formation by these fuels can differ, which has been demonstrated in our experimental results.

3.5 Fuel decomposition pathway analysis

Recognizing that the success of a chemical kinetic model in predicting the sooting tendency for a fuel depends on its ability to predict the soot precursors, several literature gas-phase kinetic models were employed to simulate the experimental conditions and their predicted results of soot precursors were compared and discussed in the following. For butane isomers, two available models compared were taken from USC Mech II [1] and Merchant *et al.* [3]. For X_F=0.29, X_{O_2}=0.90, and K=57 s^{-1} (V_0=V_L=14.9 cm/s), computed spatially-resolved mole fraction profiles of acetylene using these two chemical kinetic models are shown and compared in Fig. 3.9. For *n*-butane the peak acetylene mole fraction for the Merchant model is 0.045, whereas for the USC Mech II it is 0.050. A comparison for *iso*-butane shows that the peak acetylene mole fraction predicted by these Merchant and USC Mech II models are 0.038 and 0.049, respectively. Although both of the models predict the higher acetylene mole fraction for *n*-butane than *iso*-butane, the quantitative values have differences between the two models. In addition, the much larger difference in the measured soot loading of butane isomers is not seen to match the difference in the amount of soot precursors produced. This can be understood that as the soot formation being a complex process of various reaction pathways, it may not correlate proportionally with the predicted amount of precursors formed.

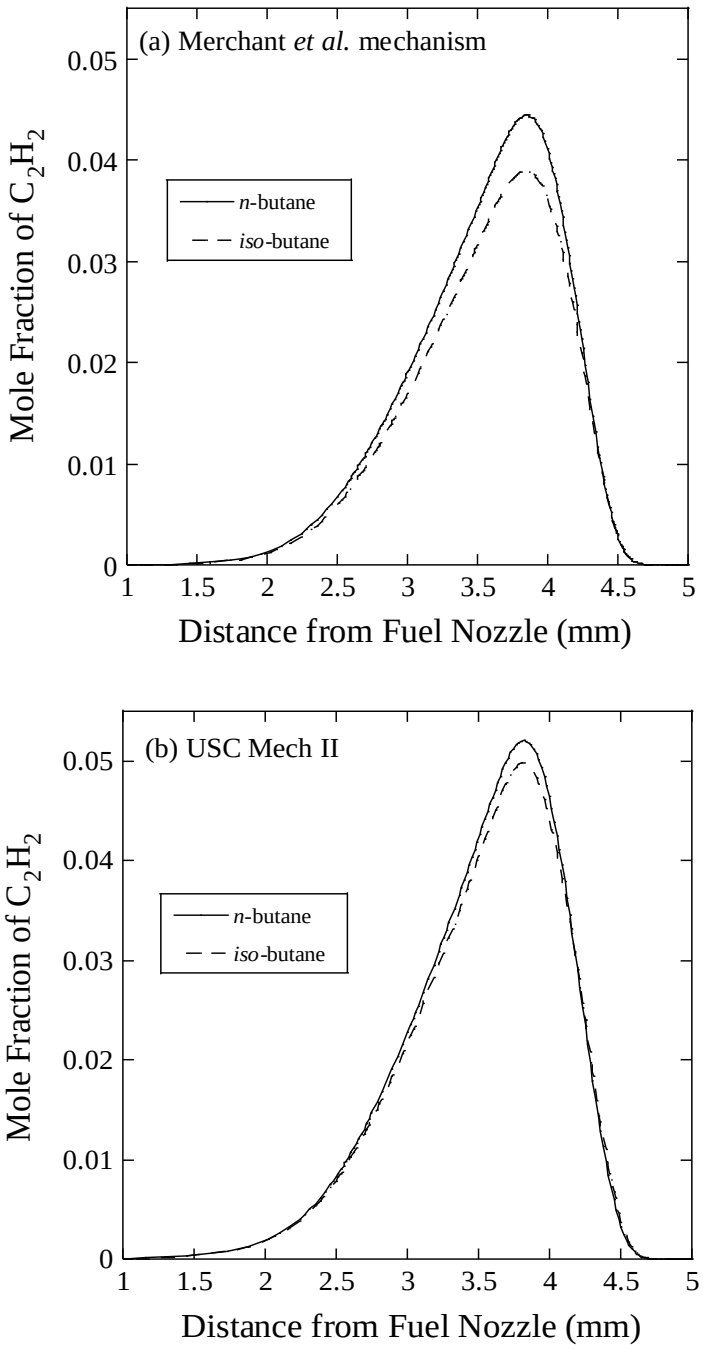

Figure 3.9: Comparison of computed mole fraction profiles of acetylene for *n*-butane and *iso*-butane isomers using the chemical kinetic models of (a) Merchant *et al.* [3] and (b) USC Mech II [1]. Conditions: $X_F = 0.29$, $X_{O2} = 0.90$, and $K = 57\ s^{-1}$.

Similarly, when the mole fraction profiles of propargyl are compared for *n*-butane, as shown in Fig. 3.10, the Merchant mechanism predicts a peak value of 0.0012, whereas for the USC Mech II it is 0.00075. For *iso*-butane in Fig. 3.10, the peak propargyl mole fractions predicted by the Merchant and USC Mech II models are 0.0015 and 0.0009, respectively. Although the trend of *iso*-butane producing more propargyl than *n*-butane holds for both of the models, the amounts predicted differ between the two models. Major initial fuel breaking pathways for the two models are further shown and compared in Fig. 3.11 for *n*-butane and *iso*-butane. Overall, the Merchant mechanism predicts that 41.3% fuel breaking is through direct decomposition of *n*-butane, wherein the USC Mech II shows a 25.5% contribution from this pathway. The major contribution of fuel breaking pathway for the USC Mech II comes from H-abstraction, which is 72.4%. Similarly for *iso*-butane the direct decomposition pathway has 54.2% and 39.9% contributions for the Merchant and USC Mech II models, respectively. For *iso*-butane, H-abstraction leads to fuel breaking with 45.7% contribution for the Merchant model and 60% contribution for the USC Mech II. Interestingly, it is noticed that although these two models differ in predicting the soot precursors, their predicted profiles of the major species and temperatures match well with each other. It is clear that further investigation is needed to reconcile the discrepancies between the two models, as accurate descriptions of the amount of soot precursors are imperative in soot formation mechanisms.

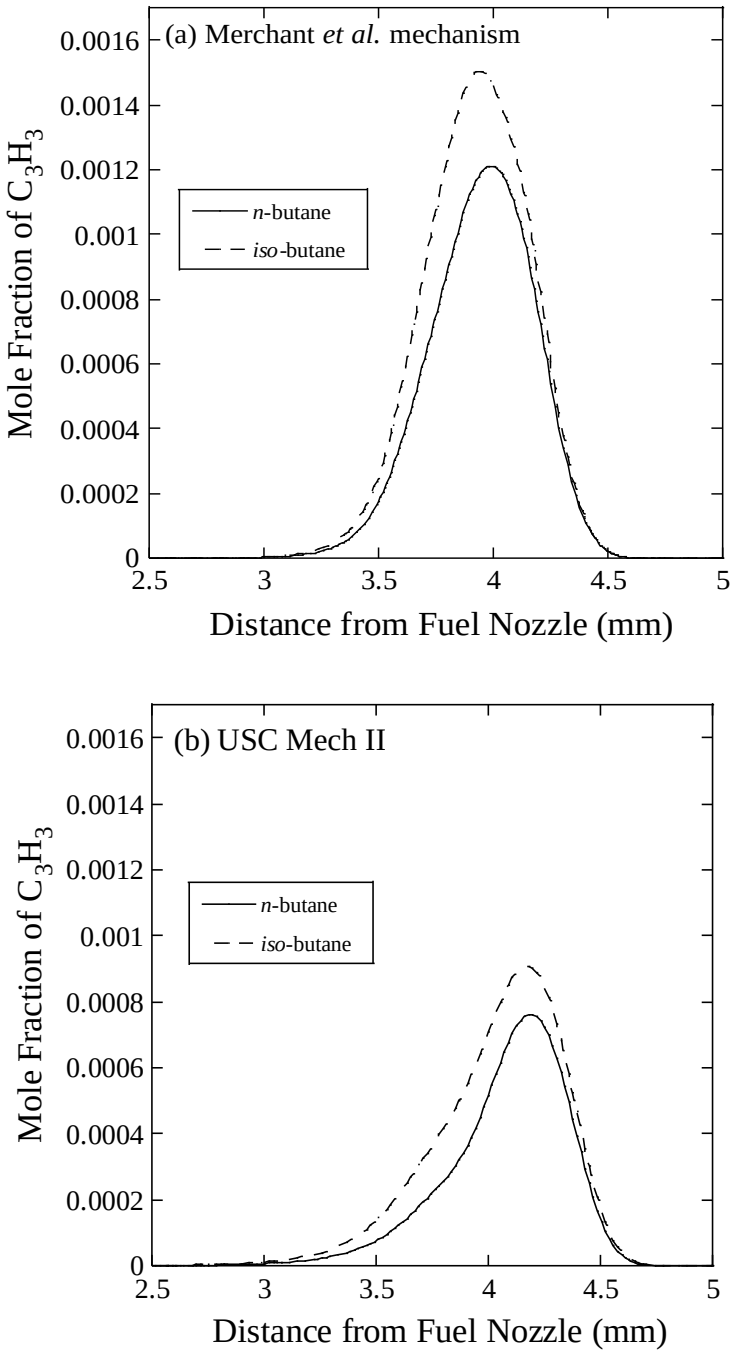

Figure 3.10: Comparison of computed mole fraction profiles of propargyl for *n*-butane and *iso*-butane isomers using the chemical kinetic models of (a) Merchant *et al.* [3] and (b) USC Mech II [1]. Conditions: $X_F = 0.29$, $X_{O2} = 0.90$, and $K = 57\ s^{-1}$.

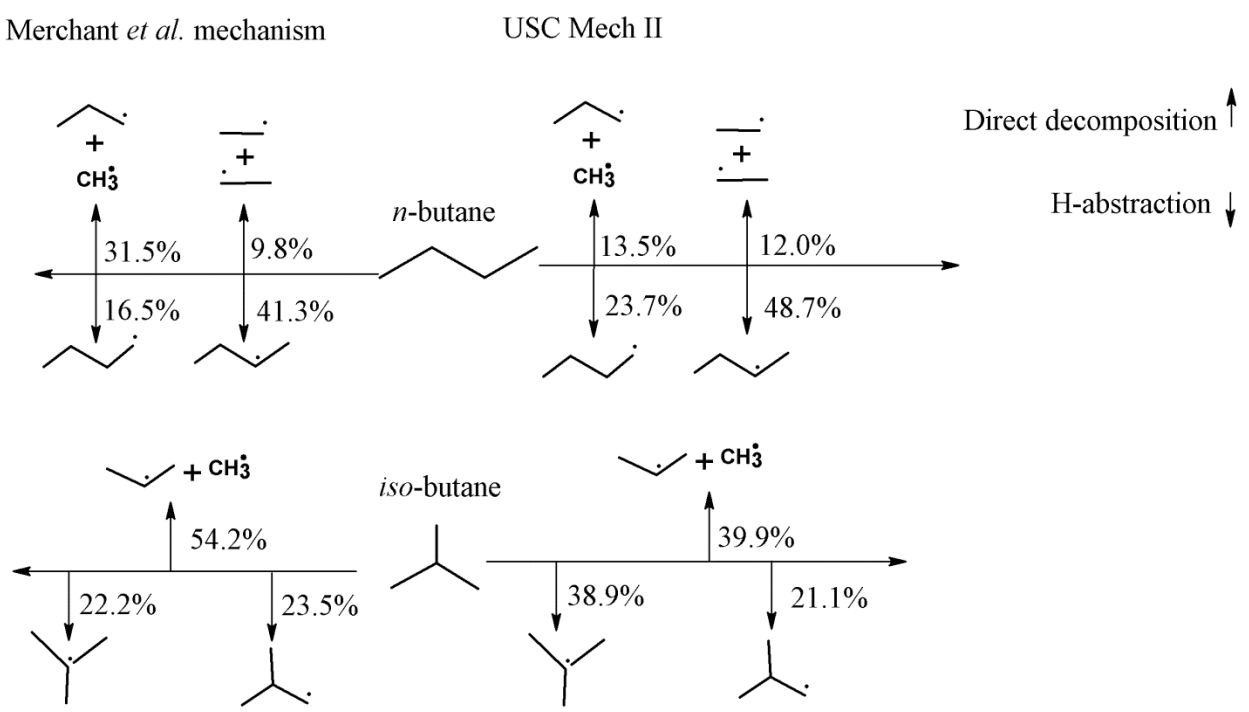

Figure 3.11: Comparison of initial fuel breaking pathways for *n*-butane and *iso*-butane isomers using the chemical kinetic models of (a) Merchant *et al.* [3] and (b) USC Mech II [1]. Conditions: $X_F = 0.29$, $X_{O2} = 0.90$, and $K = 57\ s^{-1}$.

The chemical kinetic models used for flame simulations of butanol isomers under conditions of X_F=0.29, X_{O_2}=0.90, and K=57 s^{-1} (V_0=V_L=14.9 cm/s) were taken from Merchant *et al.* [3] and Sarathy *et al*. [2]. The spatially-resolved profiles of acetylene predicted by the Merchant and Sarathy models for butanol isomers are shown in Fig. 3.12. The peak mole fractions of acetylene precursors predicted using the Merchant (Sarathy) model are 0.04 (0.039), 0.037 (0.041), 0.04 (0.042), and 0.025 (0.039) for *n*-butanol, *iso*-butanol, *sec*-butanol, and *tert*-butanol, respectively. A comparison of propargyl precursors predicted by these two models is shown in Fig. 3.13. The peak mole fractions of propargyl predicted by the Merchant (Sarathy) model are 0.00073 (0.0013), 0.00082 (0.0017), 0.0011 (0.0013), and 0.0022 (0.0027) for *n*-butanol, *iso*-butanol, *sec*-butanol, and *tert*-butanol, respectively. Again, both of the models are found to predict dissimilar amounts of precursors formed by butanol isomers and the rankings in terms of peak mole fraction values also differ. A closer look at the fuel breaking steps also illustrates that the two models differ in the major contributions of specific pathways as shown in Fig. 3.14. The initial breaking step of *n*-butanol shows that the direct decomposition has 40% and 24.8% contribution in the Merchant and Sarathy models, respectively. For *iso*-butanol the direct fuel decomposition has 74% and 43% contributions in the Merchant and Sarathy models, respectively. Through the direct decomposition, *sec*-butanol shows contributions of 70% and 34% in the Merchant and Sarathy models, respectively. Lastly, in *tert*-butanol breaking the direct decomposition has 98% and 82% contributions in the Merchant and Sarathy models, respectively. The remaining fuel breaking for all the butanol isomers described by both of the models is through H-abstraction reactions.

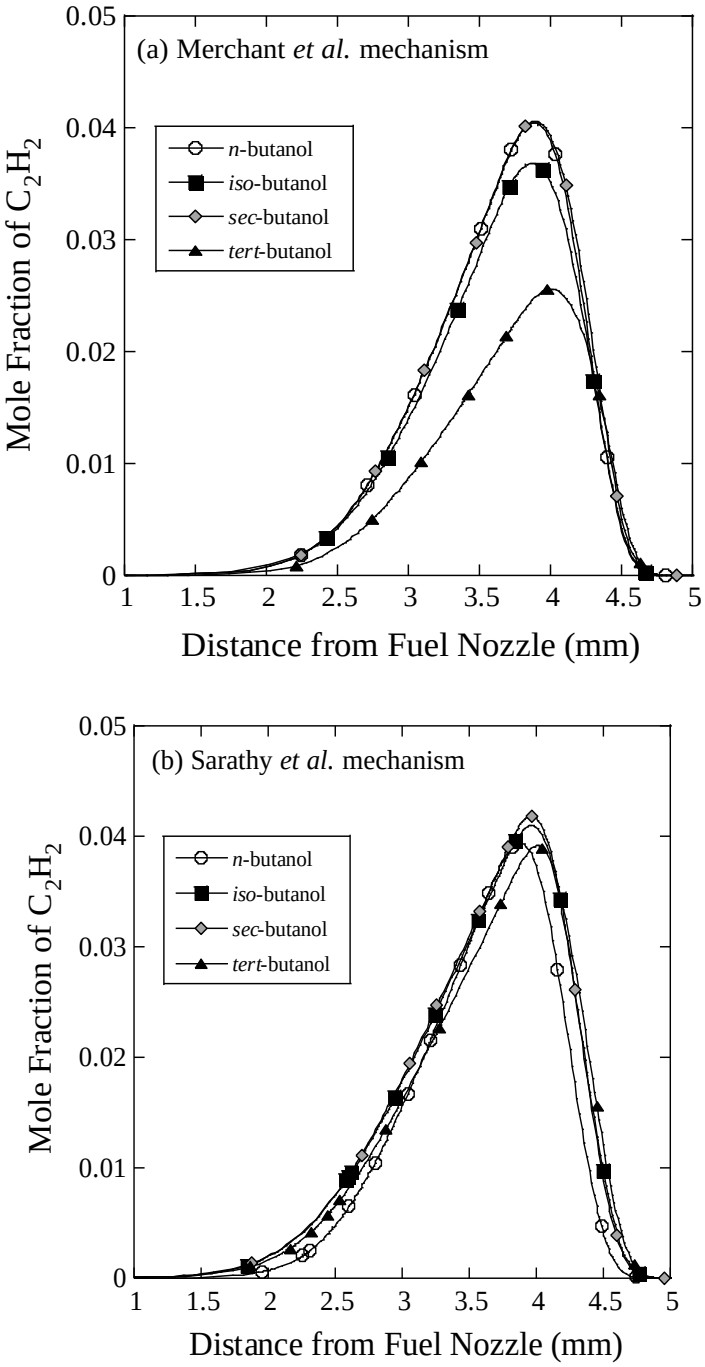

Figure 3.12: Comparison of computed mole fraction profiles of acetylene for butanol isomers using the chemical kinetic models of (a) Merchant *et al.* [3] and (b) Sarathy *et al.* [2]. Conditions: $X_F = 0.29$, $X_{O2} = 0.90$, and $K = 57\ s^{-1}$.

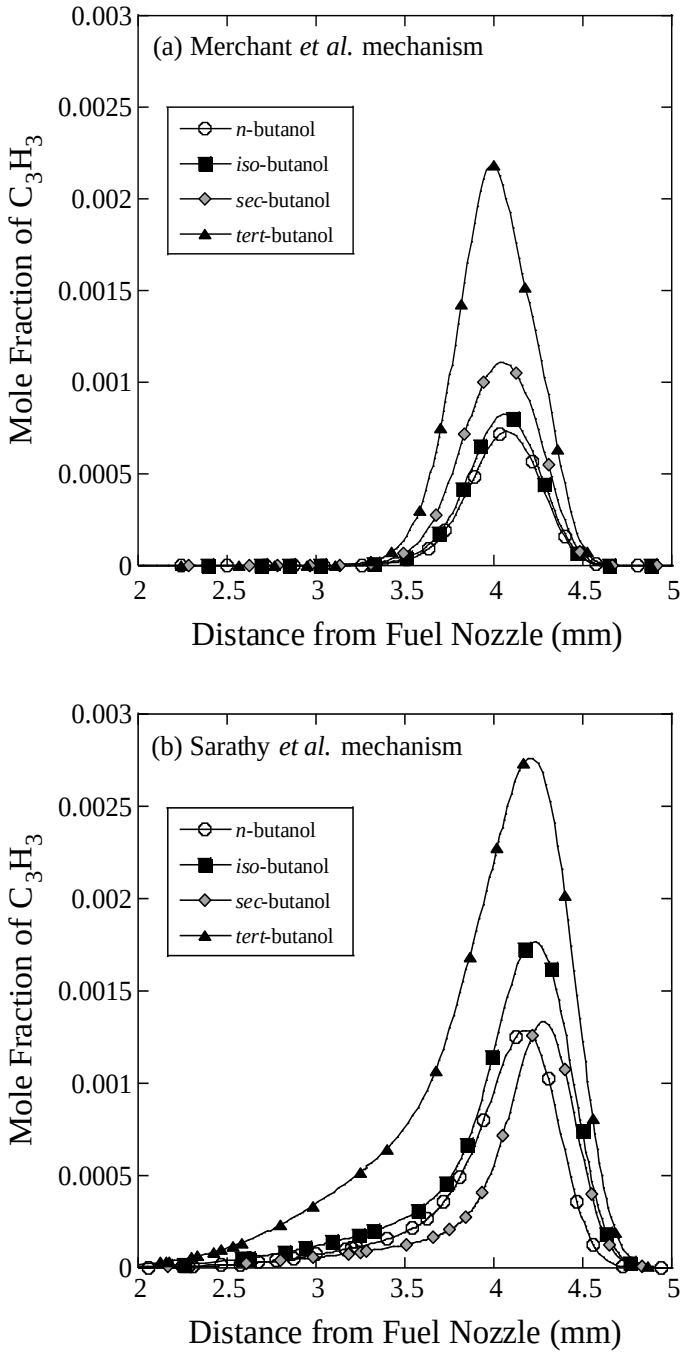

Figure 3.13: Comparison of computed mole fraction profiles of propargyl for butanol isomers using the chemical kinetic models of (a) Merchant *et al.* [3] and (b) Sarathy *et al.* [2]. Conditions: $X_F = 0.29$, $X_{O2} = 0.90$, and $K = 57\ s^{-1}$.

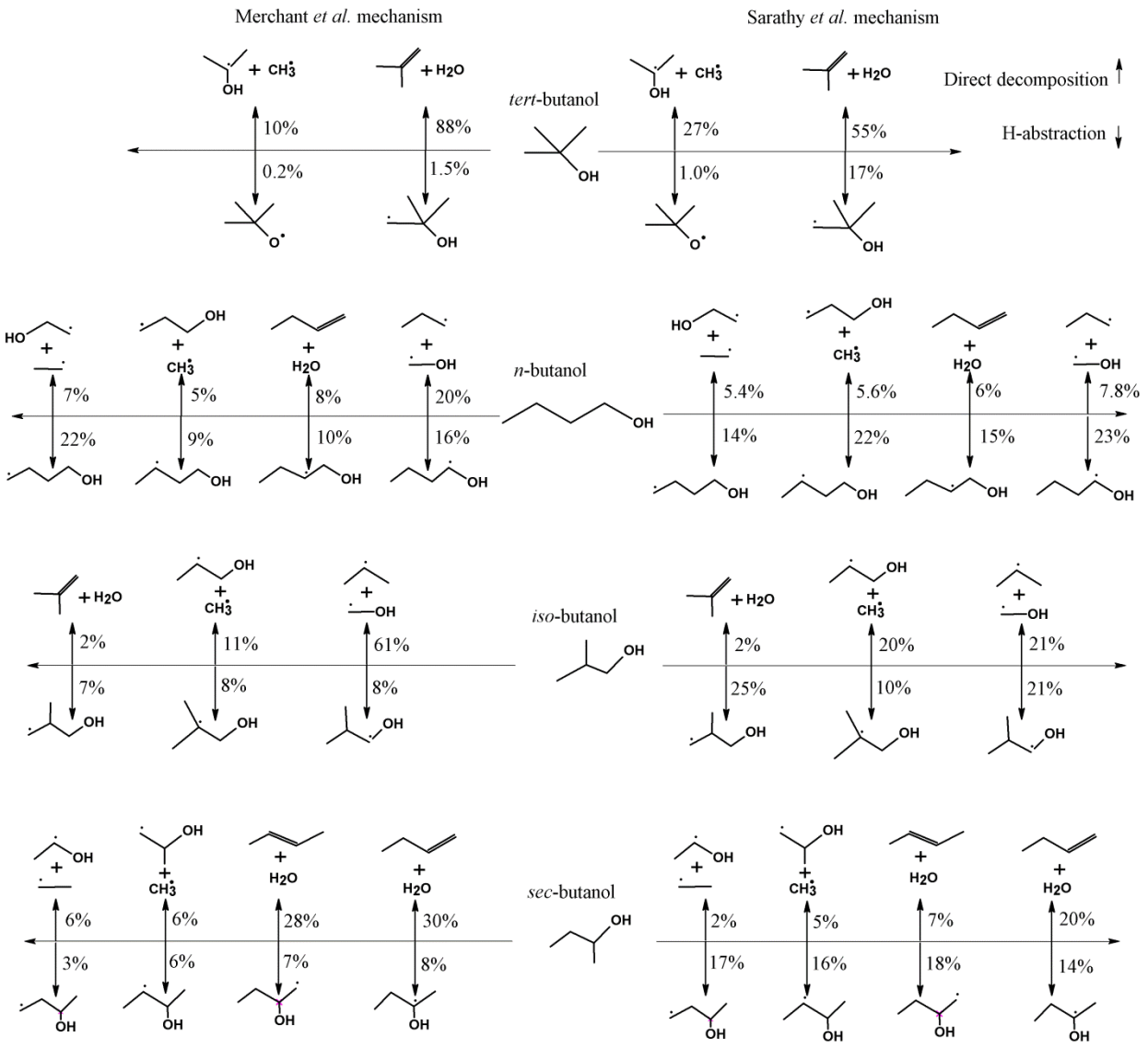

Figure 3.14: Comparison of initial fuel breaking pathways for butanol isomers using the chemical kinetic models of (a) Merchant *et al.* [3] and (b) Sarathy *et al.* [2]. Conditions: X_F = 0.29, X_{O2} = 0.90, and K = 57 s^{-1}.

It can be observed that these models differ in predicting soot precursors and the rankings of butanol isomers in terms of soot precursor formation also differ. From this, it can be inferred that these models would need some improvements/refinements in order to predict the soot precursors so that this information can be used in the subsequent soot modeling. As pointed out by Camacho *et al.* [71], while the sooting premixed flame behavior at the nucleation stage can be predicted by the soot precursors, the sooting behavior at mass growth stage cannot be directly explained by the species profiles of soot precursors. This could be another reason why no direct correlation between the computed mole fractions of soot precursors and the measured amount of soot formed in the present experimental conditions was observed.

Furthermore, the chemical kinetic models employed here do not include PAH chemistry, and hence the concentrations of other important soot precursors such as benzene, napthalene, phenanthrene, pyrene, and larger ring PAH molecules cannot be simulated to compare with the experimental results on sooting propensity rankings for butane and butanol flames. Recognizing the important role of PAHs in soot formation process [201], PAH measurements in moderately sooting flames of butane and butanol isomers have been discussed in Chapter 4, in order to better interpret isomeric structure effects on soot formation.

Chapter 4: PAH formation in butane and butanol isomer flames

4.1 Introduction

By measuring the spatial locations of the PAH fluorescence signals and the evolution of PAHs [202-209] and through sampling investigations [210-214], the evidences, linking the PAH fluorescence to the PAH molecules, have been shown in these literature studies. Through the present PAH-PLIF experiments, we aim to study the effects of molecular structure and hydroxyl functional group on the PAH formation and growth processes. By detecting the PAH-PLIF signals at varying wavelengths, PAHs of different aromatic ring sizes have been tracked. Due to the limitations of quantitative PAH-PLIF measurements, qualitative PAH-PLIF results for the butane isomers and the butanol isomers have been compared. Because of the fuel structural effects, competitive PAH growth pathways are expected to exist [91]. Hence, fuels in the same isomeric class tend to generate different amounts of PAHs. The competitive roles of the HACA and the C_3H_3 pathways in the PAH formation have also been investigated experimentally and computationally in this chapter, by blending a branched-chain isomer with the corresponding straight-chain isomer at varying blending percentages. When keeping the total fuel loading constant, the concentrations of the propargyl and the acetylene are expected to change as a result of the fuel blending, thereby inducing the competition between the HACA and the C_3H_3 pathways for the PAH formation.

Numerous studies on the PAH formation in flames have been conducted by a number of groups e.g.,[215-219]. The PAH concentration measurements have been performed by direct sampling and gas chromatograph/mass spectrometer (GC/MS) analysis of fuel-rich, laminar premixed flames [215]. In addition, two-photon ionization time-of-flight mass spectroscopy has

been used to analyze the PAHs from laminar non-premixed flames [216]. Shock tube data at elevated pressures have been evaluated to predict the reaction pathways for the PAHs [217]. Using an online GC/MS technique, the PAH formation has been investigated in a fuel-rich, premixed, sooting burner stabilized flame for *n*-butane [218]. Molecular-beam-mass-spectrometry (MBMS) coupled with resonance-enhanced-multi-photon-ionization (REMPI) techniques have been employed to measure the concentrations of the small PAHs up to 3 aromatic rings in fuel-rich, premixed flames of propene and cyclopentene [219]. In general, the motive behind the above-mentioned studies was to provide the experimental database to build the reaction pathways for the PAH and soot formation processes.

4.2 LII and PAH-PLIF images

Figure 4.1 shows a false color representation, not drawn to the scale, of the LII and PAH-PLIF images detected for an *n*-butanol sooting flame. The fuel stream was *n*-butanol/N_2 mixture with the fuel mole fraction of $X_F = 0.29$, while the O_2/N_2 oxidizer stream was maintained at the oxygen mole fraction of $X_{O_2} = 0.90$. The PAH-PLIF images shown in Fig. 4.1 are for 334, 400, 450, and 492 nm detection wavelengths, representing the sequence of the PAH formation with different ring sizes. It is noted that the PAH-PLIF signals for the detection wavelengths actually overlap, which can be seen in the spatially-resolved profiles to be shown later in Section 4.5. Such overlap of PAH-PLIF signals is not shown in Fig. 4.1 for clarity, hence this is a representative figure. Shown in the representative Fig. 4.1, the PAH-PLIF images are closer to the fuel nozzle than the LII image. In addition, as the detection wavelength of the PAH-PLIF measurement becomes longer, corresponding to the larger ring size aromatics, the PAH-PLIF images shift closer to the LII image.

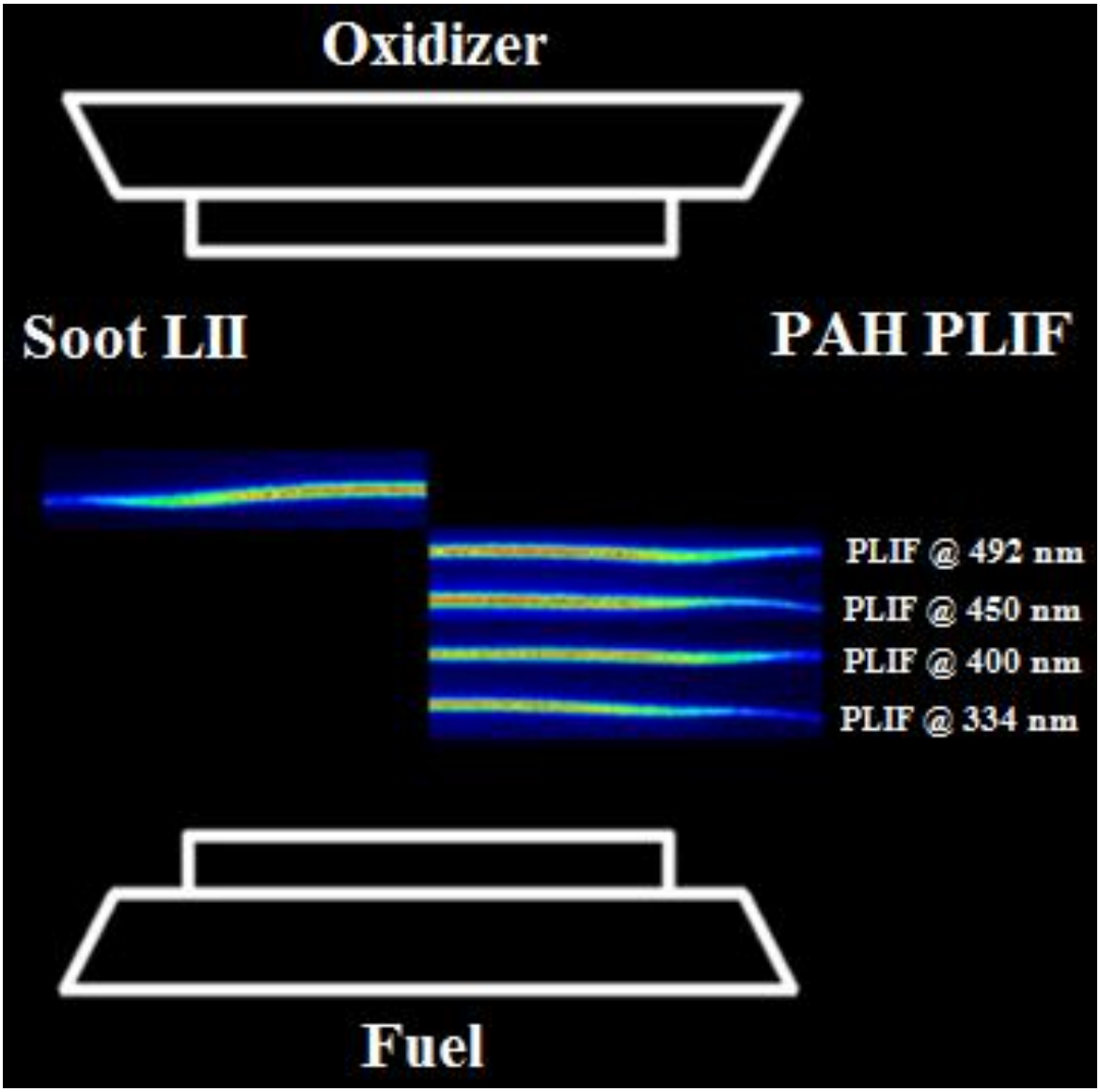

Figure 4.1: Images of LII and PAH-PLIF detected in a counterflow non-premixed flame for *n*-butanol (representative figure illustrating the relative spatial locations of the images, not shown to the scale). Conditions: $X_F = 0.29$, $X_{O2} = 0.90$, and $K = 57\ s^{-1}$.

4.3 Calibration for the n-butanol and iso-butane flames

In Figs. 4.2(a) and 4.2 (b), the spatial distribution profiles of soot volume fraction measured using the LII and LE techniques, as described in [131], are shown for the *n*-butanol sooting flame of Fig. 4.1 at seven axial locations (z) from the bottom fuel nozzle. With increasing z, Figs. 4.2 (a) and 4.2 (b) show the results in the soot growth and soot decomposition regimes, respectively. At the 'Calibration Point' for z=4.84 mm indicated in Fig. 4.2 (a), the LII signal was compared with the quantitative measurement of soot volume fraction determined by the LE measurements using abel's inversion. The refractive index used in this study is $m = 1.57 - 0.56i$, which is a widely used value and has been validated against a wide range of fuels and flame environments, as discussed in [131]. A calibration factor of 3.11×10^{8} was then calculated with this comparison, which was found to be very similar to the calibration factor of 3.05×10^{8} determined with a sooting ethylene flame in our previous study [131]. Figures 4.2 (c) and 4.2 (d) further show the similar results of the *iso*-butane sooting flame with $X_F = 0.29$ and $X_{O_2} = 0.90$. The calibration factor was determined to be 3.08×10^{8}, which, again, is very close to those of ethylene and *n*-butanol. This finding, therefore, suggests that for the conditions investigated herein, the variation in the soot optical properties is insignificant for the oxygenated fuels like *n*-butanol and the non-oxygenates like ethylene and *iso*-butane.

Using these calibration factors determined at the corresponding 'Calibration Point', the quantitative values for the LII signals at different radial-axial locations (r, z) were then

calculated. As shown in Fig. 4.2, the radial soot volume fraction distributions determined from both the LII and LE techniques compare very well for the other axial locations. Moreover, the LE- and LII-measured soot volume fraction profiles are shown to be radially symmetrical, which further demonstrates the stability of the sooting flames for liquid butanols established in the current counterflow burner facility.

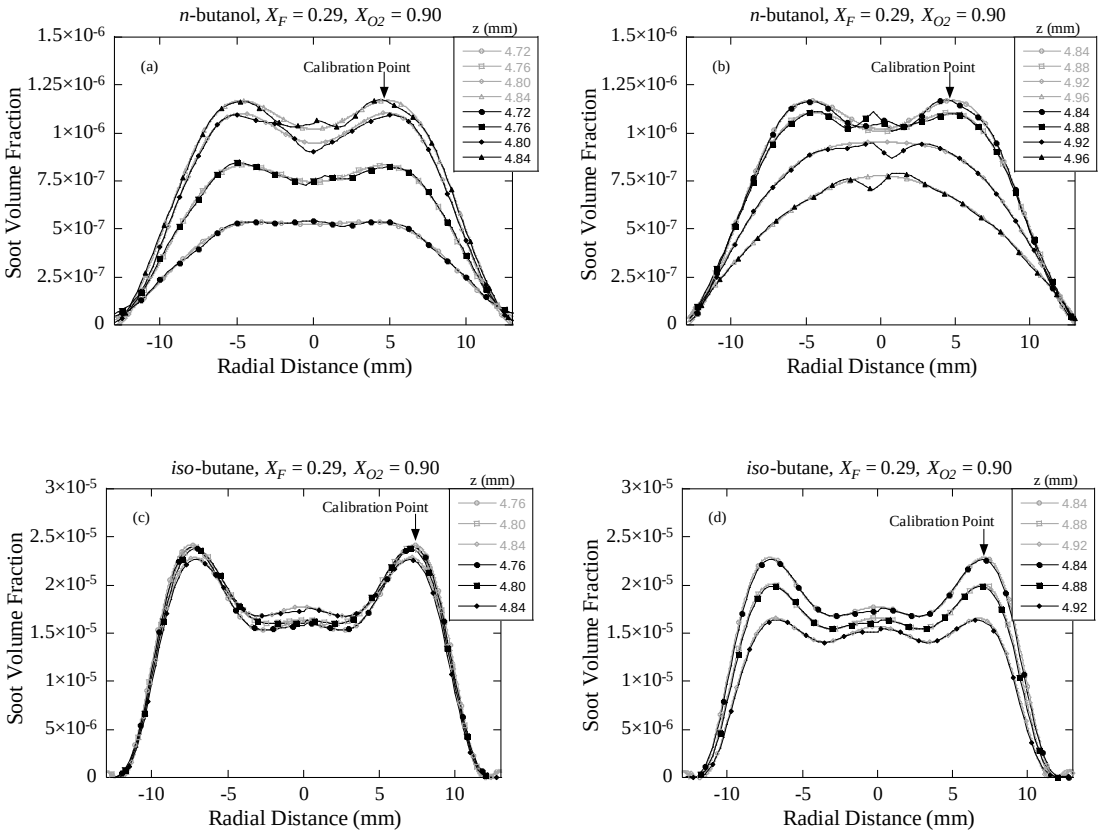

Figure 4.2: Comparison of soot volume fraction distributions in counterflow non-remixed flames measured using LE and LII: (a) soot formation zone for *n*-butanol, (b) soot decomposition and oxidation zone for *n*-butanol, (c) soot formation zone for *iso*-butane, and (d) soot decomposition and oxidation zone for *iso*-butane, where *z* represents the distance from the fuel nozzle. Conditions: X_F = 0.29, X_{O2} = 0.90, and K = 57 s^{-1}. Solid symbols/black lines are for LE measurements using abel's inversion and hollow symbols/gray lines are for LII measurements.

4.4 Test matrix

Table 3 lists the calculated adiabatic flame temperatures (T_{ad}) for all the fuels investigated using the thermodynamic database of the POLIMI mechanism [4-7]. In addition, the maximum flame temperatures (T_{max}) obtained from the counterflow flame simulations are listed in Table 3. While the reaction kinetics of the fuel pyrolysis and oxidation, the aromatic formation, the PAH mass growth and oxidation, and the soot chemistry are temperature sensitive, for a given set of X_F and X_{O_2}, the slight differences in T_{ad} and T_{max}, within the isomers and between butanes and butanols, are not expected to have a major impact on the PAH and soot formation processes in different fuels. Furthermore, the locations of T_{max} for these fuels under the same flow conditions are approximately the same, as can be seen from the spatially-resolved temperature profiles shown in the next section.

Table 3: Calculated adiabatic flame temperatures (T_{ad}), maximum flame temperatures (T_{max}) in the given counterflow conditions, and stoichiometric mixture fractions (Z_{st}) for butane and butanol isomers.

Fuel	**Fuel Stream**		**Oxidizer Stream**		**Adiabatic Flame Temperature T_{ad} (K)**	**Maximum Flame Temperature T_{max} (K)**	**Stoichiometric Mixture Fraction Z_{st}**
	X_F	X_{N_2}	X_{O_2}	X_{N_2}			
n-Butane	0.29	0.71	0.90	0.10	2991	2872	0.357
iso-Butane	0.29	0.71	0.90	0.10	2988	2868	0.357
n-Butanol	0.29	0.71	0.90	0.10	2946	2829	0.404
iso-Butanol	0.29	0.71	0.90	0.10	2943	2825	0.404
sec-Butanol	0.29	0.71	0.90	0.10	2940	2821	0.404
tert-Butanol	0.29	0.71	0.90	0.10	2934	2813	0.404

For all the mixture compositions investigated herein, Z_{st}<0.5, as shown in Table 3, and hence the "flame sheets" are all situated on the oxidizer side of the stagnation plane. Although Z_{st} has been shown to have a significant effect on soot formation, for a given set of X_F and X_{O_2} the differences in Z_{st} due to the small differences in molecular weights and stoichiometric

coefficients for butanes and butanols are deemed insignificant. Therefore, the effect of Z_{st} in comparing the sooting propensity among different fuels is not considered in the present study.

4.5 LII and PAH-PLIF results

The fuel molecular structure plays an important role in the PAH formation and growth processes as it can lead to different concentrations of precursors which can activate PAH-related reactions. Regarding the role of acetylene (C_2H_2), as it maintains relatively high concentration in the high-temperature region, PAHs can be produced through the sequential pathways of H-abstraction-acetylene-addition (HACA) reactions. Since the soot models based on the HACA mechanism underestimate the PAH and soot formations [8, 76-80], additional reactions, including the reasonantly stable aromatic radicals formed through the odd-carbon-atom pathways have been suggested to enhance the PAH formation reactions. Hence, the propargyl (C_3H_3) recombination reaction is currently considered as one of the important reactions in the incipient ring formation process. Moreover, these odd-carbon-atom pathways are also considered important in PAH growth mechanisms [91-97]. In the PAH formation process, a competition between these reaction pathways is present, based on the amounts of the precursors (e.g., C_2H_2 and C_3H_3) available locally and the flame conditions favoring these reactions [91].

Figure 4.3 shows the axial profiles of relative LII and PAH-PLIF signals along the centerline of the counterflow flames of butane and butanol isomers. Again, the experimental conditions for these flames were X_F=0.29, X_{O_2}=0.90, and K=57 s^{-1}. The PAH-PLIF signal profiles for the detection wavelengths of 334 nm, 400 nm, 450 nm, and 492 nm shown were scaled by the maximum PAH-PLIF signal for the *n*-butane flame at 492 nm detection wavelength, which is the largest PAH signal across all the flames studied in Fig. 4.3. Since the

LIF signals collected at different wavelengths have different collection efficiencies, camera sensitivities, and fluorescence lifetimes, they cannot be relatively compared with each other. Hence, wherever a qualitative comparison has been made in this study, it has been made for only a fixed detection wavelength. As it was shown earlier the LIF and LII images were shown just for the representation in Fig. 4.1 so these images did not overlap. Wherein, in the Fig. 4.3, which is drawn with the actual scale, the overlap of LIF and LII profiles can be observed. Furthermore, it is noted that considering the temperature sensitivity and concentration dependence of the PAH-PLIF signals from the aromatics of different ring sizes formed at different axial locations, the direct comparison of PAH-PLIF signals between two different detection wavelengths should be taken with caution. On the other hand, the LII profile for each flame was normalized with the maximum LII signal for *n*-butane in order to demonstrate the relative spatial locations of the PAH-PLIF profiles for different detection wavelengths (hence different aromatic ring sizes). As demonstrated in Fig. 4.3, with the same values of X_F, X_{O_2}, and K for all counterflow non-premixed flames, the spatial locations of the PAH-PLIF profiles across the C_4 fuels are almost the same for a given detection wavelength. Using the POLIMI mechanism, the computed spatially-resolved profiles, including temperature and the mole fractions of acetylene, propargyl, and benzene, have also been shown in Fig. 4.3 for the comparison. As mentioned earlier, the locations of T_{max} are almost the same, situated at 5.25 mm distance from the fuel nozzle. In this study, the detection wavelength of 334 nm represents the PAH-PLIF measurements at the inception stage, as it characterizes the PAHs with 2 and 3 aromatic rings. It is of interest to note that the computed mole fraction profiles of benzene for all flames investigated peak before (i.e. closer to the fuel nozzle) the corresponding maximum signal for the 334 nm detection.

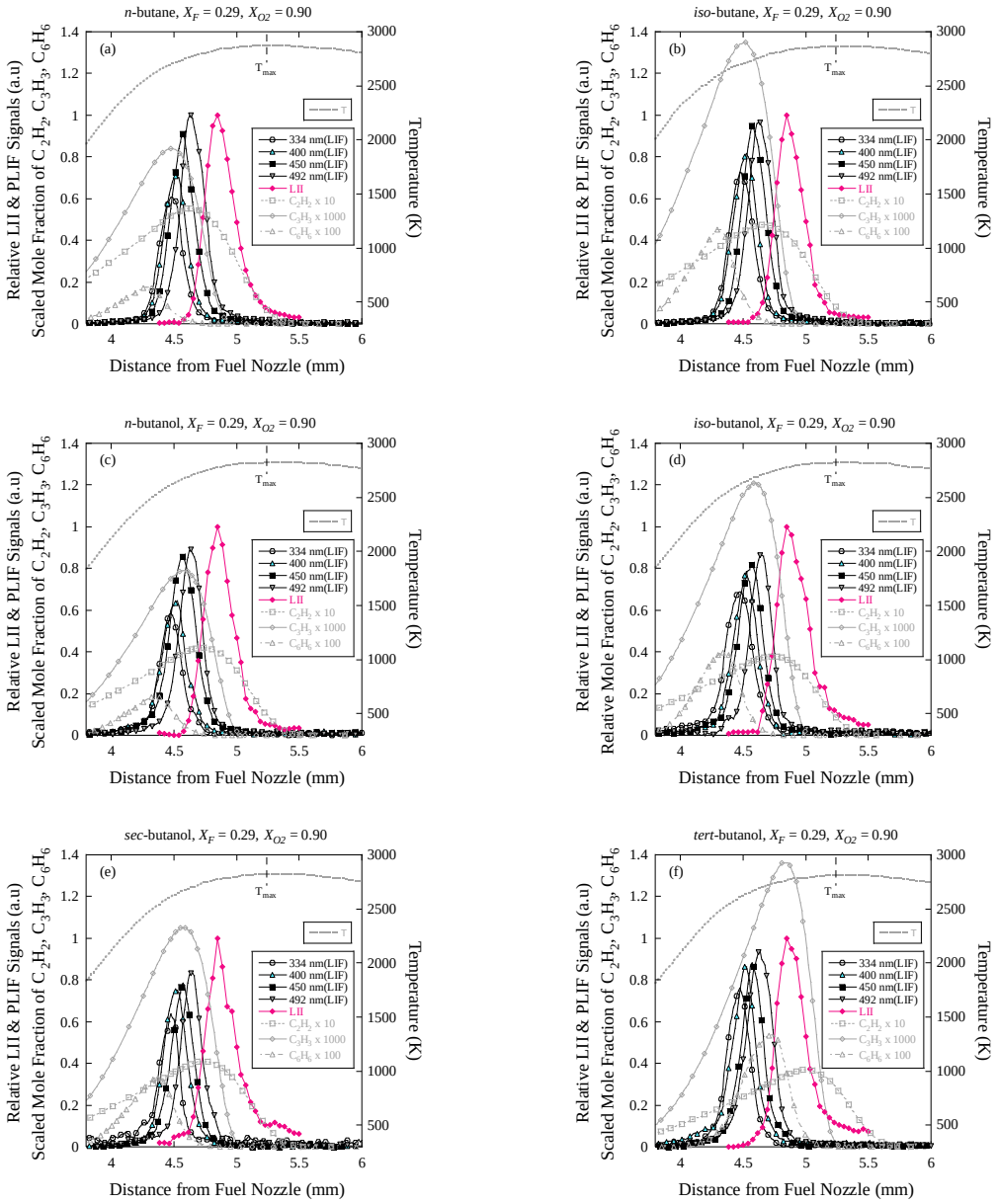

Figure 4.3: Spatial profiles of relative LII and PAH-PLIF (detection wavelengths of 334 nm, 400 nm, 450 nm, and 492 nm) signals along the centerline, as well as the computed profiles of temperature and mole fractions of acetylene, propargyl, and benzene, for: (a) *n*-butane, (b) *iso*-butane, (c) *n*-butanol, (d) *iso*-butanol, (e) *sec*-butanol, and (f) *tert*-butanol flames. Conditions: X_F = 0.29, X_{O2} = 0.90, and K = 57 s^{-1}.

It can also be observed from Fig. 4.3 that for all the butane and butanol isomers the PAH profiles are closer to the fuel side than the LII profile, indicating that PAHs grow from the fuel side. The results for all the flames also show that with the increase in detection wavelength the PAH-PLIF profiles move closer to the LII profile. This shift in PAH-PLIF profiles with increasing detection wavelength in turn indicates that the longer (shorter) detection wavelength corresponds to the larger (smaller) aromatic ring size of PAH's. A comparison of the PAH-PLIF profiles in Fig. 4.3 across the flames for any of the detection wavelengths shows that while their profile shapes appear similar, the maximum relative signal values vary. Such behavior can be associated with the fuel structural differences. This is further analyzed in detail in the following.

In general, the hydrocarbons are known to decompose by either the unimolecular dissociation or bimolecular H-abstraction. The dissociation process is also known to occur by the complex fission or simple fission. It is theorized that the butanol isomers are able to produce H_2O through the process of complex fission [35, 58, 220-223]. Since the dominant pathways of initial fuel breaking depend on the structure of the fuel, understanding the initial fuel breaking pathways is important to understand the formation of the first aromatic rings [22]. In order to aid the interpretation of the present experimental results, the fuel decomposition pathways for the butanol isomers are described hereafter. The complex fission process takes place by bonding between the hydrogen (H) and hydroxyl (OH) to form H_2O, and the α and β carbon atoms form a double bond between them to form butene [58]. In the simple fission process, first a methyl radical is abstracted from the α carbon atom, and then hydrogen radical is abstracted from the oxygen atom to form a double bond between the α carbon atom and oxygen atom to form acetone [221, 222]. In the process of H-atom abstraction, first a hydrogen atom is abstracted from the β carbon atom, then a hydroxyl radical is abstracted from the α carbon atom, thereby

facilitating the formation of a double bond between the α and β carbon atoms to form butene [58, 220, 221]. The step of the complex fission process depends on the structure of the fuel and this determines the amount of butene produced by each of the butanol isomers. Structurally, in the *tert*-butanol isomer, the hydroxyl group has a maximum number (9) of neighboring hydrogen atoms available to form the complex bonds, and hence this helps in unimolecular elimination of water. This step has been reported as the dominant pathway in butene formation [19, 41, 59, 179]. Similar complex fission reaction pathways are possible for the *n*-butanol, *iso*-butanol, and *sec*-butanol isomers, as for these fuels, the hydroxyl group has 2, 1, and 5 neighboring hydrogen atoms to form the complex bond to eliminate water [41]. For these three isomers, other competing fuel destruction pathways of H-abstraction, followed by the β-scission of the C-O bond have also been known [19, 179]. The measurements of the butene for these butanol isomers, using the Electron Ionization-Molecular Beam Mass Spectrometry (EI-MBMS) technique, by Oßwald *et al.* [28] in a flat stabilized flames on McKenna burner, showed that the *tert*-butanol isomer produces the maximum amount of the butene, followed by *iso*-butanol, *sec*-butanol, and *n*-butanol in the decreasing order. The importance of the butene formation is related to the propargyl and first aromatic benzene ring formation [28, 179]. In addition, Oßwald *et al.* [28] have experimentally shown that the propargyl radical formation follows the order of butene formation. The reactions of allene and allyl production from butene have been envisaged as the responsible reactions, linking the butene and the propargyl [224, 225]. Further, the experimental measurements, by Oßwald *et al.* [28] using the Particle-Ionization-Molecular-Beam-Mass-Spectrometry (PI-MBMS), and by McEnelly and Pfefferle [179] using the mass spectroscopy technique, have shown that the first benzene ring formation follows the order of propargyl formation, and at the initial aromatic ring formation stage the propargyl recombination reaction

is the most important. Similar observations linking the propargyl with benzene formation have been made by Hansen *et al.* [226] and Miller *et al.* [227]. From these theoretical and experimental backgrounds, it is established that the initial aromatic ring formation for butanols is governed by the propargyl radical.

The soot formation process can be divided into the inception and growth stages. Camacho *et al.* [71] and McEnally and Pfefferle [179] have noted that a direct link between the fuel structure and the PAHs at the inception stage can be established. Firstly, the PAH-PLIF profiles measured at 334 nm detection wavelength for different flames shown in Fig. 4.3 are analyzed and compared. As stated earlier, this detection wavelength corresponds to PAHs with 2 and 3 aromatic rings, and hence this detection wavelength represents the PAHs at the inception stage. Figure 4.4(a) shows and compares the maximum relative PAH-PLIF signals at 334 nm detection wavelength for butane and butanol isomers. It is seen that in terms of the amounts of 2- and 3-ring aromatics produced by these fuels, they are ordered as *tert*-butanol > *iso*-butane > *iso*-butanol > *sec*-butanol > *n*-butane > *n*-butanol. Similar rankings have been observed by McEnally and Pfefferle [179] in their benzene measurements. It is also noted from Fig. 4.4(a) that the PAH-PLIF signal at 334 nm for *iso*-butane is larger than that for *n*-butane. Similar PAH inception ranking for the butane isomers was also observed by Camacho *et al.* [71], and McEnally and Pfefferle [179], as they noted that the branched chain isomers produce more propargyl than the straight chain isomers. Additionally, the straight chain isomer was found to produce more acetylene than the branched chain isomer [179]. These literature results indicate that at the inception stage the odd-carbon-atom pathway of propargyl recombination dominates. By similar analogy, the results which have been shown in Fig. 4.4(a) for the butanol isomers can be explained and inferred, as the most branched isomer, *tert*-butanol, has the maximum PAH-

PLIF signal, followed by *iso*-, *sec*-, and *n*-butanol, in the order of the degree of branching of these isomers as defined in [179].

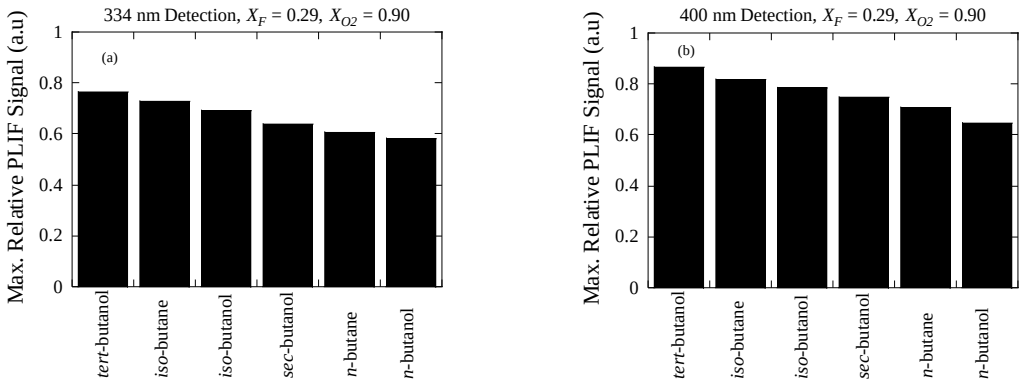

Figure 4.4: Comparison of maximum relative PAH-PLIF signals measured for butane and butanol isomers: (a) detection wavelength of 334 nm corresponding to 2- and 3-ring aromatics and (b) detection wavelength of 400 nm corresponding to 4-ring aromatics. Conditions: X_F = 0.29, X_{O2} = 0.90, and K = 57 s^{-1}.

Based on the results in Fig. 4.3, Fig. 4.4(b) compares the maximum relative PAH-PLIF signals at the detection wavelength of 400 nm for different flames. As discussed earlier, this detection wavelength corresponds to 4 ring aromatic species such as pyrene [164]. For this detection wavelength, the isomers studied are ranked as *tert*-butanol > *iso*-butane > *iso*-butanol > *sec*-butanol > *n*-butane > *n*-butanol. This ranking follows that observed for the 2- and 3-ring aromatics produced. As the present ranking is consistent with the literature results discussed earlier, it can be inferred that even up to the 4-ring aromatics formation, the odd-carbon-atom pathways of PAH formation dominate. The dominance of the odd-carbon-atom pathways via propargyl is further demonstrated in Sec. 4.6 and explained through the path analyses discussed in Sec. 4.7.

From our previous study of the soot formation process of the counterflow non-premixed flames [131], the sooting tendencies for these fuels were ranked as *n*-butane > *iso*-butane > *tert*-butanol > *n*-butanol > *iso*-butanol > *sec*-butanol. Shown in Fig. 4.5 are these rankings for the flames of Fig. 4.3 by plotting their maximum soot volume fractions. In Fig. 4.5(a) the maximum soot volume fraction values with y-axis scale of $10^{-5} - 10^{-4}$, while in Fig. 4.5(b) these are shown using a y-axis scale of $10^{-6} - 10^{-5}$ so that the rankings for the butanol isomers can be prominently seen. In our previous study [131], it was also observed that the sooting propensity rankings in terms of soot volume fraction remained the same as shown in Fig. 4.5 for varying fuel mole fractions, oxidizer mole fractions, and strain rates. Comparing these with the current PAH-PLIF measurements at the inception stage shown in Fig. 4.4, it can be concluded that the PAH formation at the inception stage does not correlate with the amount of soot formed. As discussed earlier, the PAH growth and the soot formation processes involve various complex

parallel pathways, and hence a direct correlation between the soot volume fraction and the PAH formation at the inception stage may not exist.

For further analysis, the maximum relative PAH-PLIF signals for all the detected wavelengths are compared in Fig. 4.6 for the straight- and branched-chain isomers. The error bars in Fig. 4.6 are based on twice the standard deviation of the repeated measurements. The comparisons of relative PAH-PLIF signals have been made and discussed in the following discussions, only for each individual detected wavelength, as mentioned earlier it cannot be made across the two different detection wavelengths. A comparison of *n*-butane and *iso*-butane is shown in Fig. 4.6 (a), and it is seen that *iso*-butane has a larger signal than *n*-butane for the 334 nm detection wavelength, which could be due to the dominance of the odd-carbon-atom pathways discussed in [179]. The same trend continues for the detection wavelengths of 400 and 450 nm, as shown in Fig. 4.6 (a), consistent with the findings of [179] for *iso*-butane that the odd-carbon-atom pathways remain dominant at this stage. However, a comparison of PAH-PLIF signals at the detection wavelength of 492 nm shows that *n*-butane turns out to have larger signal than *iso*-butane. Since the location of the peak PAH-PLIF signal at 492 nm detection wavelength is closer to the sooting flame, the larger signal for the *n*-butane could be because the temperature-sensitive HACA reactions for *n*-butane enhance the PAH formation at this growth stage as discussed in [179].

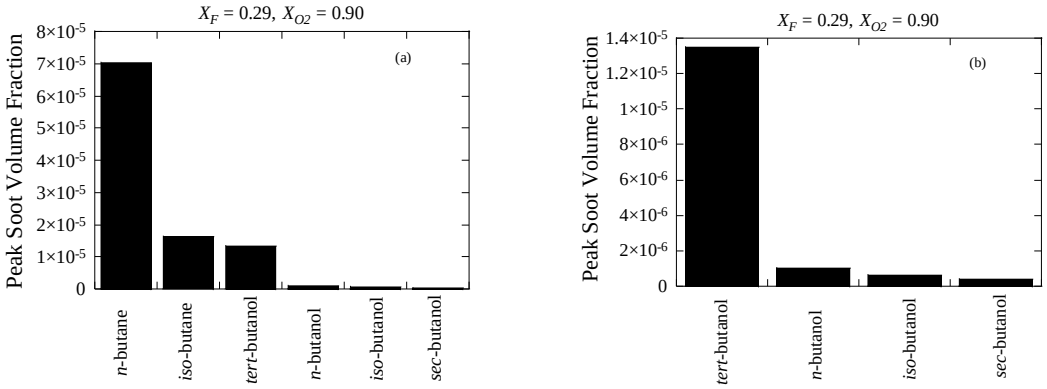

Figure 4.5: Comparison of peak soot volume fractions: (a) all the butane and butanol isomers and (b) butanol isomers. Conditions: X_F = 0.29, X_{O2} = 0.90, and K = 57 s^{-1}.

In Fig. 4.6(b), a comparison for *n*-butanol and *iso*-butanol has been presented. While *iso*-butanol shows larger PAH-PLIF signal than *n*-butanol for the detection wavelengths of 334 and 400 nm, *n*-butanol exhibits larger PAH-PLIF signal for the detection wavelengths of 450 and 492 nm. Since the results are consistent with those of [179], it is inferred that the consequence of the branched chain isomer producing more propargyl and its effect at the PAH inception stage [179] result in larger PAH-PLIF signal for *iso*-butanol up to the detection wavelength of 400 nm. However, from 450 nm onwards the PAH-PLIF signal for *n*-butanol being larger suggests that the HACA mechanism for *n*-butanol propels the growth of PAHs (larger aromatic ring size) in comparison to *iso*-butanol [179]. Similar findings were observed when comparing *sec*-butanol and *n*-butanol, as shown in Fig. 4.6(c).

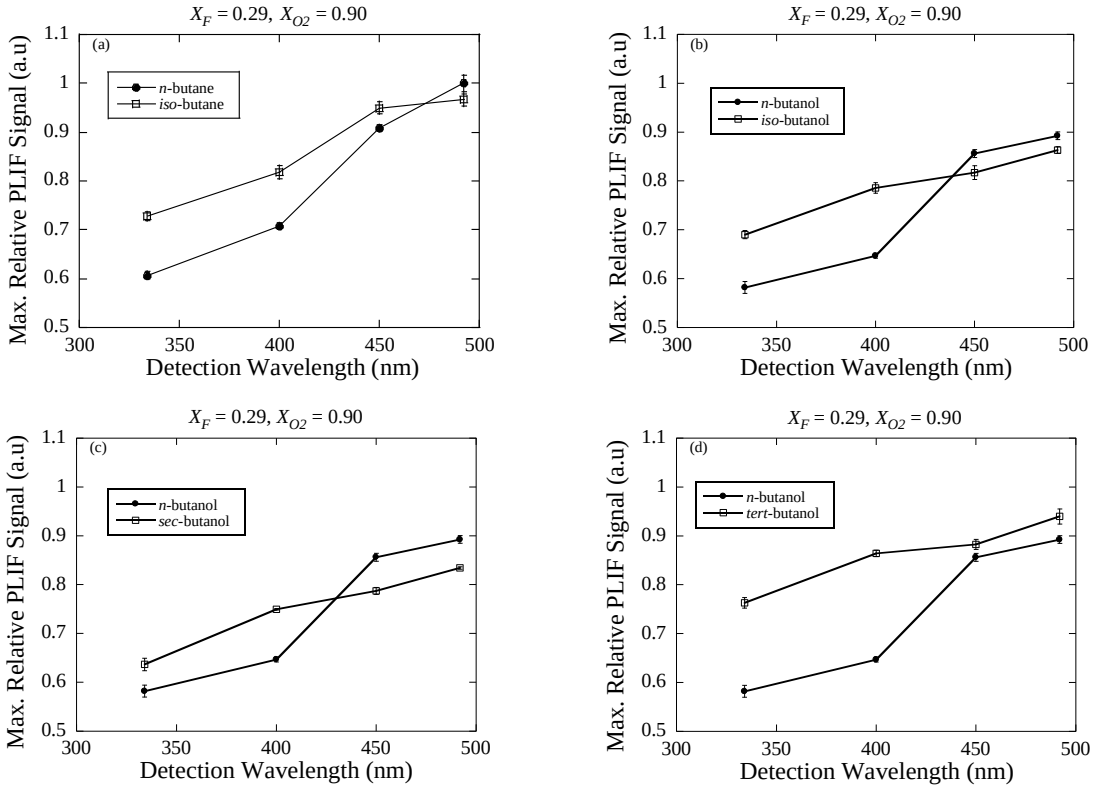

Figure 4.6: Comparison of maximum relative PAH-PLIF signals for 334 nm, 400 nm, 450 nm, and 492nm detection wavelengths: (a) *n*-butane and *iso*-butane, (b) *n*-butanol and *iso*-butanol, (c) *n*-butanol and *sec*-butanol, and (d) *n*-butanol and *tert*-butanol. Conditions: $X_F = 0.29$, $X_{O2} = 0.90$, and $K = 57\ s^{-1}$. Lines are connected to guide the discernment only.

Further, in Fig. 4.6(d), a comparison of *n*-butanol and *tert*-butanol is shown. Consistent with the demonstration in [179] that the odd-carbon-atom pathways for the branched chain isomer dominate, *tert*-butanol is seen to have larger PAH-PLIF signal than *n*-butanol at 334 nm detection wavelength. This behavior continues for the other detection wavelengths of 400, 450, and 492 nm. Following the literature results, this suggests that for *tert*-butanol, the odd-carbon-atom pathways produce an abundance of incipient aromatics, such that the odd-carbon-atom pathways of the PAH growth remain a dominant pathway. Other than *tert*-butanol, when *n*-butanol was compared with the other two isomers, the HACA mechanism for *n*-butanol is expected to account for the formation of larger PAHs.

Figures 4.7(a) and 4.7(b) compare the maximum relative PAH-PLIF signals for all C_4 flames measured at the detection wavelengths of 450 nm and 492 nm, respectively. Since these two detection wavelengths characterize PAHs larger than 4 aromatic rings, as discussed earlier, Fig. 4.7 demonstrates the rankings for the PAH growth stage. The ranking for 450 nm detection shows *iso*-butane > *n*-butane > *tert*-butanol > *n*-butanol > *iso*-butanol > *sec*-butanol. At the detection wavelength of 492 nm, signifying much larger PAHs, the ranking becomes *n*-butane > *iso*-butane > *tert*-butanol > *n*-butanol > *iso*-butanol > *sec*-butanol. The rankings, as shown in Fig. 4.7 for the PAH growth stage, are seen to be different from those shown in Fig. 4.4 for the PAH inception stage. As the 492 nm detection wavelength represents large PAHs formed prior to the formation of soot particles, the PAH formation ranking in Fig. 4.7(b) is seen to be consistent with the sooting tendency ranking displayed in Fig. 4.5 and that reported in [131].

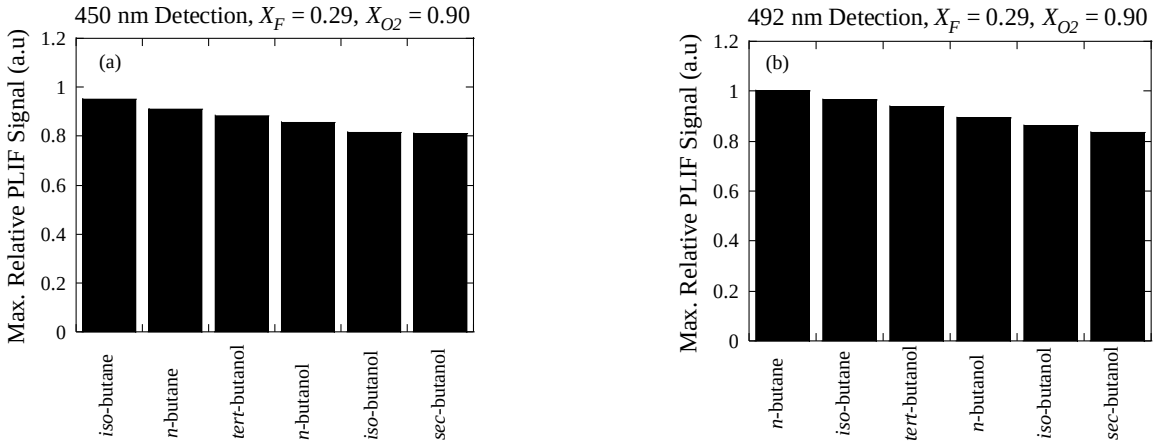

Figure 4.7: Comparison of maximum relative PAH-PLIF signals measured for butane and butanol isomers: (a) large aromatics measured with detection wavelength of 450 nm and (b) large aromatics measured with detection wavelength of 492 nm. Conditions: X_F = 0.29, X_{O2} = 0.90, and K = 57 s^{-1}.

4.6 Non-premixed counterflow flame simulations

From the experimental results at the inception stage and based on their consistency with the literature studies, it is inferred that the amount of the PAH formed by these isomers is expected to show a correlation with the ability of each fuel to produce the propargyl. To correlate the incipient PAH formation and the precursors such as the acetylene and the propargyl, the experimental conditions were simulated using the POLIMI mechanism [4-7]. Since the present experimental results only provide qualitative measurements, a quantitative comparison with the simulated results is not made. Hence, these experimental and simulated results are compared in terms of predictability of the rankings. The calculated peak mole fractions of the acetylene and the propargyl formed in the flames by these isomers are shown in Figs. 4.8(a) and 4.8(b), respectively. In terms of the peak acetylene formation, the isomers are ranked as *n*-butane > *iso*-butane > *n*-butanol > *sec*-butanol > *iso*-butanol > *tert*-butanol. As discussed in McEnally and Pfefferle [179], the straight chain isomers produce more acetylene than the branched chain isomers. The comparison of these isomers in terms of the peak propargyl formation shows that the ranking is *tert*-butanol > *iso*-butane > *iso*-butanol > *sec*-butanol > *n*-butane > *n*-butanol. This propargyl ranking is consistent with the experimental ranking for the incipient PAHs shown in Fig. 4.4. Further, the A_1-ring (benzene, C_6H_6) in Fig. 4.8(c), the A_2–A_3-ring PAHs (naphthalene, $C_{10}H_8$; anthracene, $C_{14}H_{10}$) in Fig. 4.8(d), and the A_4-ring PAH (pyrene, $C_{16}H_{10}$) in Fig. 4.8(e) show the same ranking as the propargyl in Fig. 4.8(b). From the past studies [85, 90, 179], it has been shown that in the formation of benzene ring the propargyl radical plays an important role. Therefore, the ranking of A_1-ring formation (benzene, C_6H_6) in Fig. 4.8(c) follows the trend for propargyl radical formation in Fig. 4.8(b).

From the experimental results shown in Fig. 4.4, the A_2–A_3 and the A_4 rankings show the same trend as the simulated results shown in Figs. 4.8(d) and 4.8(e). It will be demonstrated in due course that the simulated results exhibit the importance of the odd-carbon-atom pathways through the propargyl recombination at the incipient stage. Since the POLIMI mechanism [4-7] does not consider the PAHs larger than A_4, the experimental results based on the 450 nm and 492 nm detection wavelengths shown in Fig. 4.7 cannot be simulated and compared.

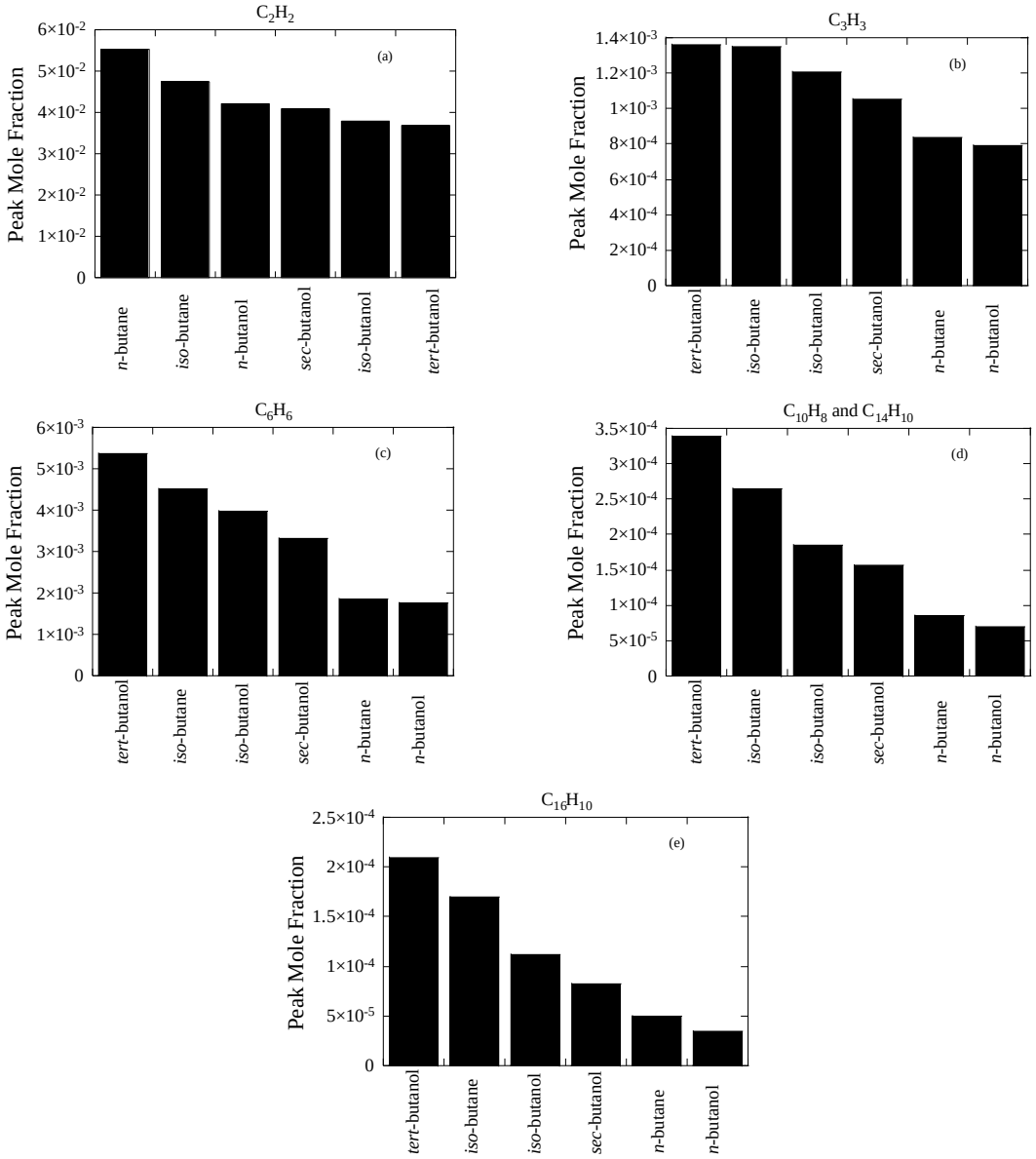

Figure 4.8: Comparison of calculated peak mole fractions using the POLIMI mechanism [4-7] for butane and butanol isomer: (a) acetylene (C_2H_2), (b) propargyl (C_3H_3), (c) A_1 aromatics (C_6H_6), (d) A_2 and A_3 aromatics ($C_{10}H_8$ and $C_{14}H_{10}$), and (e) A_4 aromatics ($C_{16}H_{10}$). Conditions: $X_F = 0.29$, $X_{O2} = 0.90$, and $K = 57\ s^{-1}$.

4.7 Effects of fuel blending

With the discussion and comparison with the literature studies so far, it can be inferred that the PAH formation at the inception stage is mostly governed by the ability of the isomers to produce the propargyl and hence by the odd-carbon-atom pathway of the initial aromatic ring formation. At the PAH growth stage, however, the HACA mechanism is also expected to play a role, as seen in the sooting tendency for some of the fuels. To further investigate the role of the HACA mechanism, the two straight chain fuels, *n*-butane and *n*-butanol, were blended with their respective branched chain isomers. The total fuel mole fraction was still kept constant at X_F=0.29, while the blending percentage (β) is defined as:

$$\beta = \frac{X_{F,branched}}{X_F} \times 100, \quad (3)$$

where $X_{F,branched}$ is the mole fraction of the branched chain isomer in the fuel stream. As the fuels from the same isomeric class with the same molecular weight were blended, for the same oxidizer stream, the Z_{st} values for binary blend/N_2 mixtures remain the same as those of the respective neat components listed in Table 3, when the total fuel mole fraction is fixed at X_F=0.29. In addition, because of the small difference in T_{ad} or T_{max} for the isomers of the same class, as shown in Table 3, the variation of T_{ad} or T_{max} with β is considered insignificant. Hence, any change in PAH-PLIF signals with varying fuel blending ratios observed in the current experiments can be attributed to the fuel structure effects.

With X_F=0.29, X_{O_2}=0.90, and K=57 s^{-1}, the relative intensities of the PAH-PLIF signals for the binary blends of *n*-butane/*iso*-butane and *n*-butanol with other butanol isomers varying from β=0% to 100% were measured. Figure 4.9 shows such experimental results in order to identify the synergistic effects. Again, the PAH-PLIF signals were scaled by the maximum value for the

detection wavelength of 492 nm for the *n*-butane flame. Two different fuel blending effects were generally observed in Fig. 4.9. First, an increase in the PAH-PLIF signal followed by a decrease, with the increase in β, was seen. For brevity, this behavior in the PAH-PLIF signal is named as 'positive synergy' in the current study. The second type of the blending effect was opposite to the first one, which exhibits a decrease in the PAH-PLIF signal followed by an increase, with the increase in β. This behavior in the PAH-PLIF signal is named as 'negative synergy' herein.

These behaviors, as shown in Fig. 4.9, can be examined by comparing them with the simulated results of the acetylene and the propargyl. In Figs. 4.8 and 4.10-4.13, the simulated results of the peak mole fractions of the acetylene and the propargyl using the POLIMI mechanism for the individual fuels and the binary blends are shown, along with those of the A_1–A_4 aromatics. The detailed discussions on Figs. 4.10-4.13 will be provided later. As observed from the Fig. 4.8, the straight chain isomers produce more acetylene than the branched chain isomers, while the branched chain isomers produce more propargyl than the straight chain isomers. From Figs. 4.10-4.13, a uniform observation of an increase in the propargyl concentration and a decrease in the acetylene concentration with increasing β can be made. Considering these, 'positive synergy' is explained in the following.

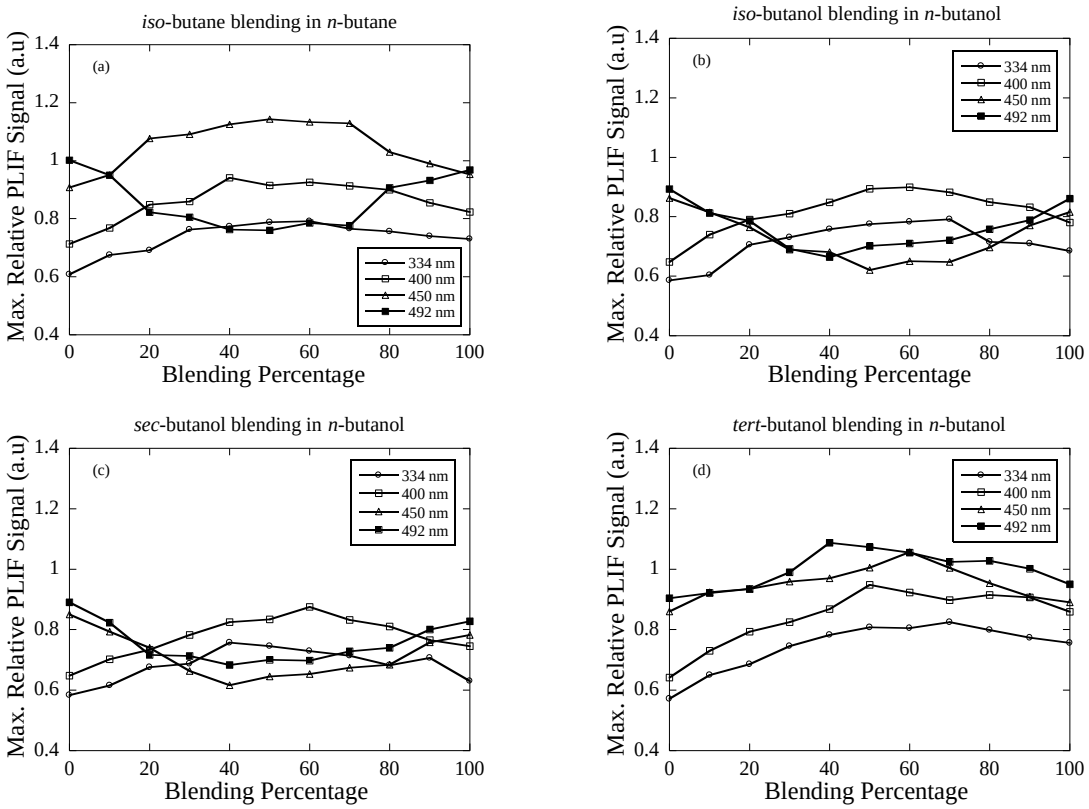

Figure 4.9: Variations of maximum relative PAH-PLIF signals for 334 nm, 400 nm, 450 nm, and 492nm detection wavelengths with blending percentage: (a) blending *iso*-butane in *n*-butane, (b) blending *iso*-butanol in *n*-butanol, (c) blending *sec*-butanol in *n*-butanol, and (d) blending *tert*-butanol in *n*-butanol. Conditions: X_F = 0.29, X_{O2} = 0.90, and K = 57 s^{-1}. Lines are connected to guide the discernment.

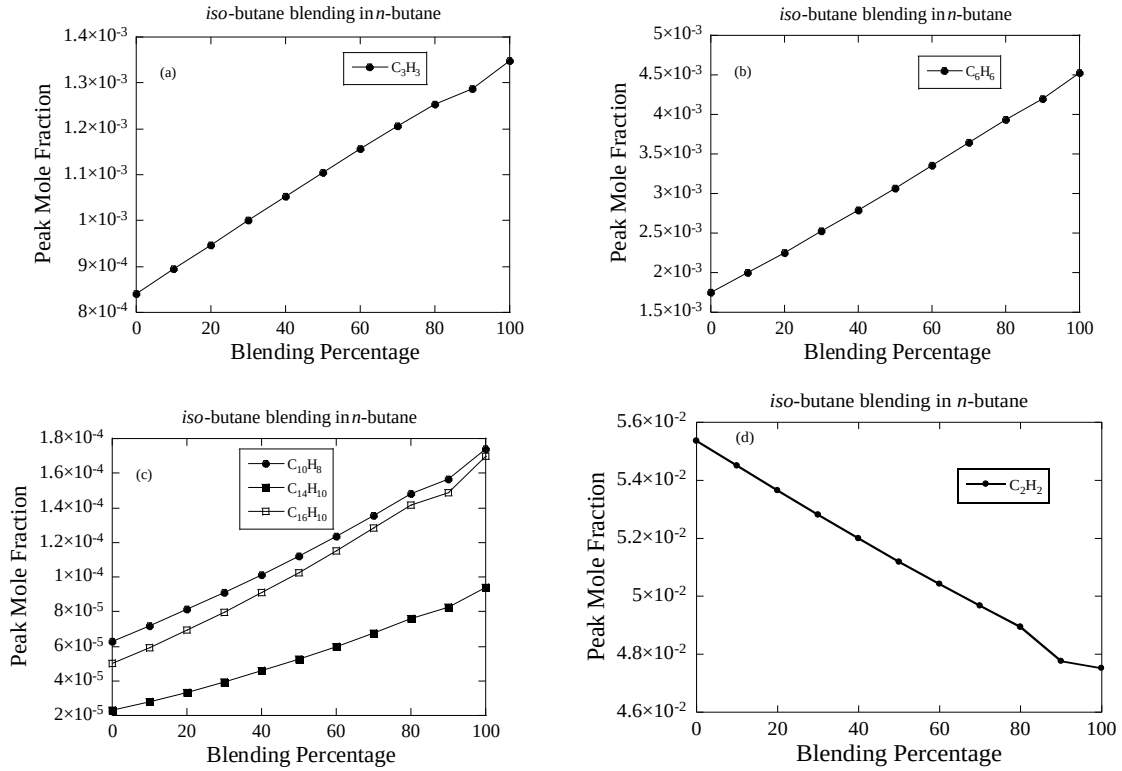

Figure 4.10: Variations of calculated peak mole fractions using the POLIMI mechanism [4-7] with blending percentage for blending *iso*-butane in *n*-butane: (a) propargyl (C_3H_3), (b) A_1 aromatics (C_6H_6), (c) A_2, A_3, and A_4 aromatics ($C_{10}H_8$, $C_{14}H_{10}$, and $C_{16}H_{10}$, respectively), and (d) acetylene (C_2H_2). Conditions: $X_F = 0.29$, $X_{O2} = 0.90$, and $K = 57\ s^{-1}$.

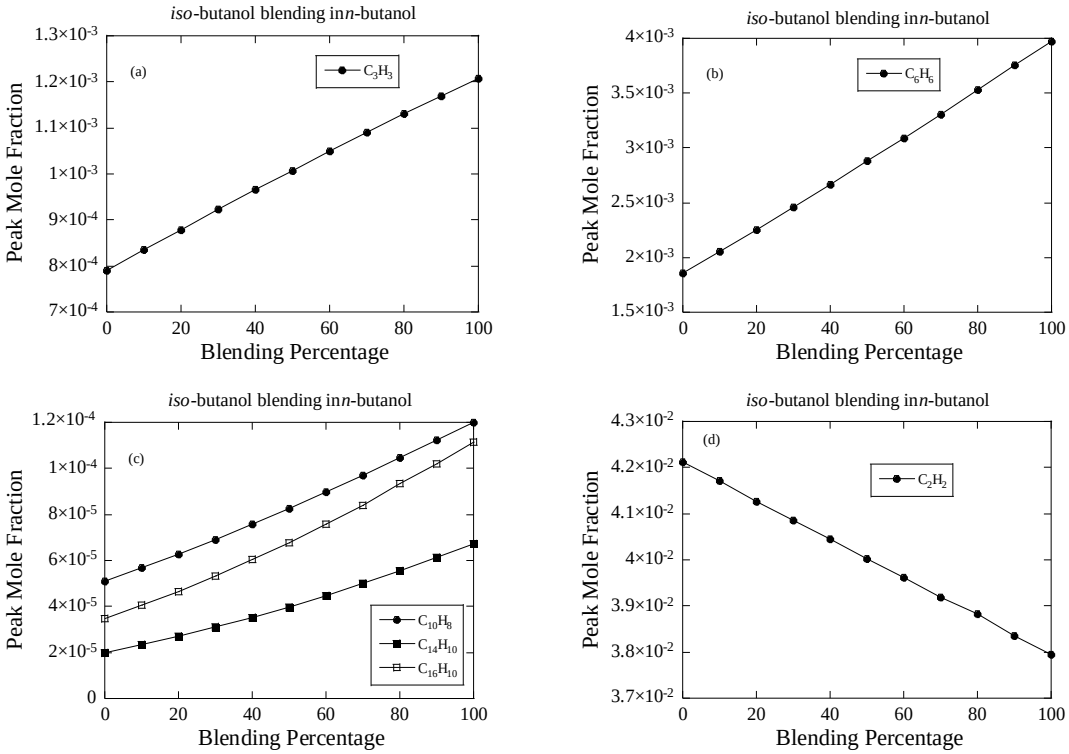

Figure 4.11: Variations of calculated peak mole fractions using the POLIMI mechanism [4-7] with blending percentage for blending *iso*-butanol in *n*-butanol: (a) propargyl (C_3H_3), (b) A_1 aromatics (C_6H_6), (c) A_2, A_3, and A_4 aromatics ($C_{10}H_8$, $C_{14}H_{10}$, and $C_{16}H_{10}$, respectively), and (d) acetylene (C_2H_2). Conditions: $X_F = 0.29$, $X_{O2} = 0.90$, and $K = 57\ s^{-1}$.

For the detection wavelength of 334 nm, as shown in Fig. 4.6(a), the PAH-PLIF signal for *iso*-butane is larger than that for *n*-butane. As previously discussed, this can be inferred to be the dominant role of the odd-carbon-atom pathways involving the propargyl in the PAH inception stage for *iso*-butane. It is seen from Fig. 4.9(a) that the relative PAH-PLIF signal for the detection wavelength of 334 nm increases from β=0% (pure *n*-butane) to β=70%, followed by a decrease when further increasing *iso*-butane blending to β=100% (pure *iso*-butane). In view of the consistent increase in the propargyl concentration in Fig. 4.10(a) with increasing β, this non-monotonic behavior in the PAH-PLIF signal for the 334 nm detection wavelength can be argued to be related to the other parallel reactions competing with the odd-carbon-atom pathways, such as the HACA mechanism. An initial increase in *iso*-butane blending provides more aromatic rings, and hence in conjunction with the HACA mechanism, this results in the 'positive synergy', as the increase in the PAH-PLIF signals for these binary blends surpass those of pure *n*-butane and pure *iso*-butane. However, the decrease in acetylene concentration with increasing *iso*-butane blending, as shown in Fig. 4.10(d), could lead to a decrease in the PAH-PLIF signal with the detection wavelength of 334 nm for β=80–100%.

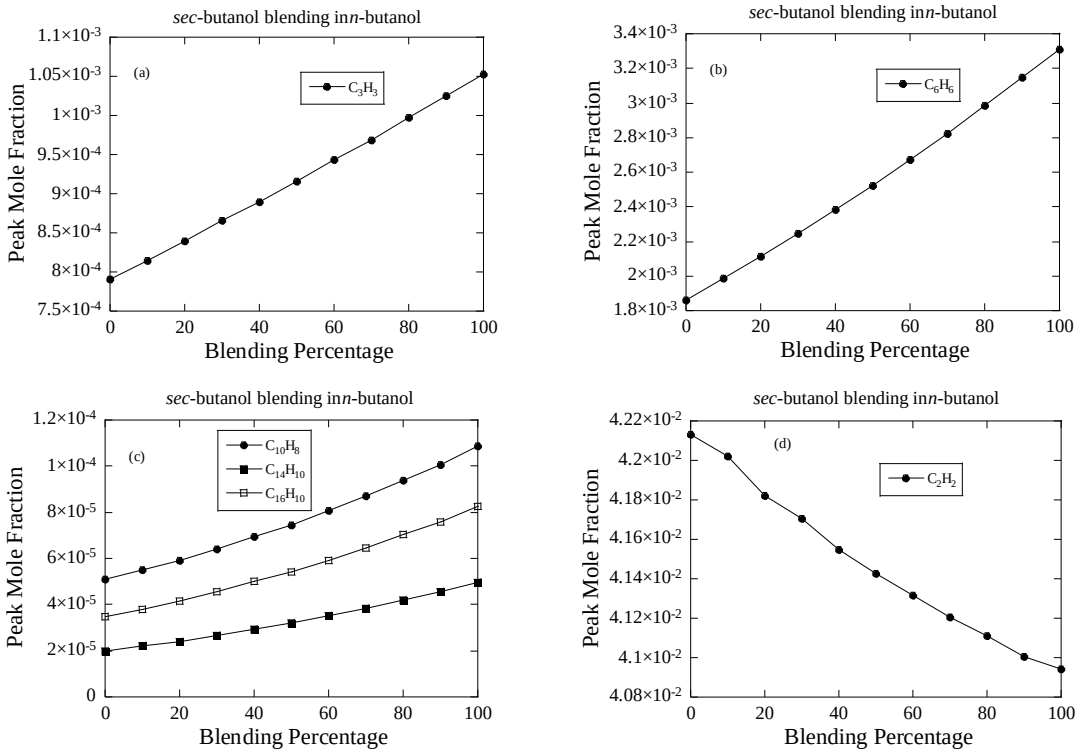

Figure 4.12: Variations of calculated peak mole fractions using the POLIMI mechanism [4-7] with blending percentage for blending *sec*-butanol in *n*-butanol: (a) propargyl (C_3H_3), (b) A_1 aromatics (C_6H_6), (c) A_2, A_3, and A_4 aromatics ($C_{10}H_8$, $C_{14}H_{10}$, and $C_{16}H_{10}$, respectively), and (d) acetylene (C_2H_2). Conditions: $X_F = 0.29$, $X_{O2} = 0.90$, and $K = 57\ s^{-1}$.

On the other hand, the 'negative synergy' exhibits opposite effects with increasing β. As seen from Fig. 4.6(a), *n*-butane has a larger PAH-PLIF signal for the 492 nm detection wavelength than *iso*-butane. Based on this experimental finding and the simulated results, the importance of the acetylene in the large PAH formation through the HACA mechanism is suggested. In addition, it is observed from Fig. 4.9(a) for the detection wavelength of 492 nm that the relative PAH-PLIF signal decreases from β=0% (pure *n*-butane) to β=50%, and then increases with increasing *iso*-butane blending towards β=100% (pure *iso*-butane). Again, a monotonic decrease in acetylene concentration with increasing β can be seen from Fig. 4.10(d). This decrease in acetylene concentration in turns impedes the PAH formation mostly dominant through the HACA pathways along with the odd-carbon-atom pathways. Since the propargyl concentration increases with increasing β, as shown in Fig. 4.10(a), a further increase in *iso*-butane blending for β=50–100% adds the aromatic rings through the odd-carbon-atom pathways, thereby providing more sites for PAH growth and leading to an increase in the PAH-PLIF signal for the 492 nm detection wavelength. These synergistic results further indicate that both the propargyl and the acetylene are involved in the PAH formation, and the concentrations of these precursors, as well as the local flame environment/condition, determine the dominant role played by either of these in the PAH formation.

Based on the above discussions, the experimental results of Fig. 4.9 can then be better understood and explained. In Fig. 4.9(a), the changes in the relative PAH-PLIF signal intensities as a result of blending *iso*-butane in *n*-butane have been shown. For the detection wavelengths of 334, 400, and 450 nm, the PAH-PLIF signals exhibit 'positive synergy', which can be inferred by the dominance of the odd-carbon-atom pathways at this inception stage for *iso*-butane. At the

detection wavelength of 492 nm, the ‘negative synergy’ was observed, which emphasizes the importance of the HACA mechanism for *n*-butane at this growth stage.

Figure 4.9(b) shows the experimental results of blending *iso*-butanol in *n*-butanol. Similar to the binary blends of *iso*-butane and *n*-butane, synergistic effects have been observed. For the detection wavelengths of 334 and 400 nm, the ‘positive synergy’ can be observed, suggesting that for these wavelengths of detection the odd-carbon-atom pathways for *iso*-butanol produce relatively more PAHs than *n*-butanol. For the detection wavelengths of 450 and 492 nm, the ‘negative synergy’ can be observed, thereby implying the importance of the HACA mechanism enhancing the PAH growth for the *n*-butanol at this stage. The same observations have been made for the blending effects of *sec*-butanol and *n*-butanol as shown in Fig. 4.9(c). In Fig. 4.9(d), when blending *tert*-butanol in *n*-butanol, all the detection wavelengths show the ‘positive synergistic’ effect. This further emphasizes the importance of the odd-carbon-atom pathways in the PAH formation for *tert*-butanol.

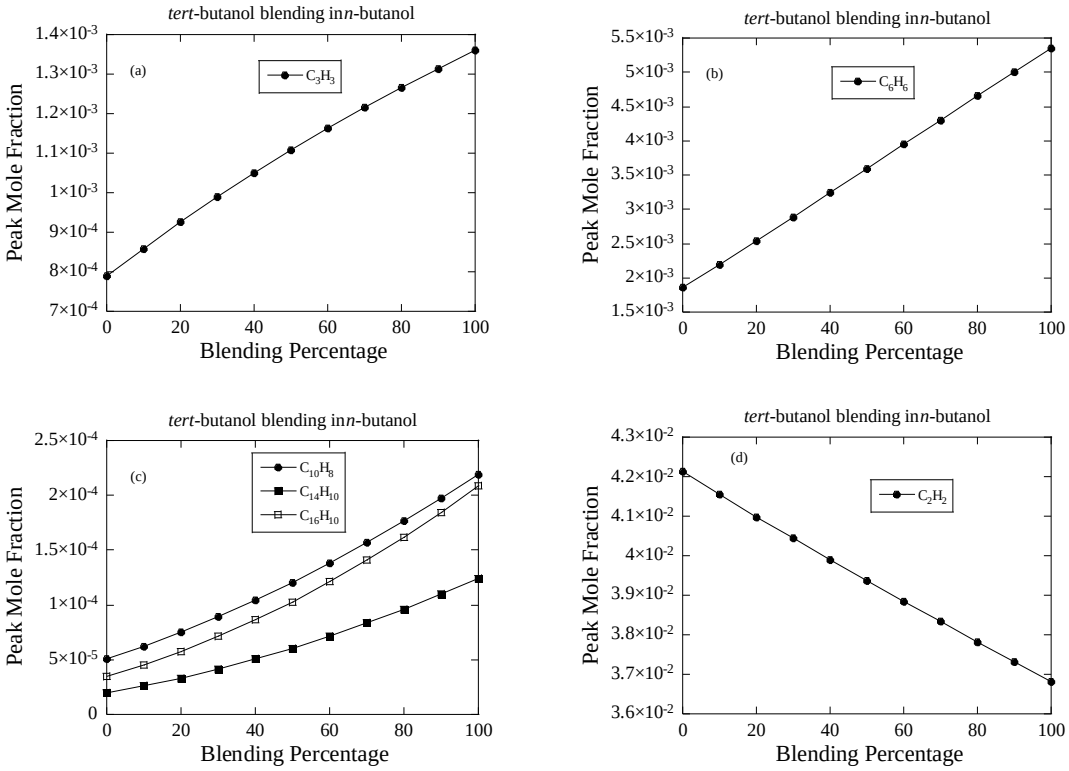

Figure 4.13: Variations of calculated peak mole fractions using the POLIMI mechanism [4-7] with blending percentage for blending *tert*-butanol in *n*-butanol: (a) propargyl (C_3H_3), (b) A_1 aromatics (C_6H_6), (c) A_2, A_3, and A_4 aromatics ($C_{10}H_8$, $C_{14}H_{10}$, and $C_{16}H_{10}$, respectively), and (d) acetylene (C_2H_2). Conditions: $X_F = 0.29$, $X_{O2} = 0.90$, and $K = 57\ s^{-1}$.

The binary fuel blend experiments of Fig. 4.9 are also simulated using the POLIMI mechanism [4-7]. For the binary blends of *n*-butane and *iso*-butane, Fig. 4.10 demonstrates that the peak mole fractions of the propargyl and the A_1–A_4 ring PAHs increase with increasing β, while the peak mole fraction of the acetylene decreases. Although a non-monotonic response ('positive or negative synergy') was observed in the PAH-PLIF experiments shown in Fig. 4.9(a), such a behavior is not observed in the simulations. Similar observations are made for blending the branched chain butanols in *n*-butanol, as shown in the simulated results of Figs. 4.11–4.13, namely a monotonic increase in the amounts of the propargyl and the A_1–A_4 ring PAHs formed, and a monotonic decrease in the amount of the acetylene formed. This discrepancy in the experimental and simulated results is further investigated by conducting path analyses of PAH formation in the POLIMI mechanism [4-7], as well as by examining the role of the acetylene in PAH formation along with the dominance of the propargyl at the inception stage.

4.8 PAH formation pathways

In the present path analyses, the *n*-butane flame with X_F=0.29, X_{O_2}=0.90, and K=57 s^{-1} was used as a representative condition for the demonstration. For each of the aromatic species of interest, the spatially-integrated rates of the production for the contributing reaction pathways were taken from the simulation. The percentage contribution from each reaction pathway was calculated relative to the sum of all the related, spatially-integrated rates of production. Figures 4.14(a) and 15(b) demonstrate the major kinetic pathways leading to the formation of the benzene (C_6H_6) and the phenyl (C_6H_5), respectively. It can be seen from Fig. 4.14(a) that 56.5% of the benzene formation is due to the conversion of the phenyl by reacting with the hydrogen radical. Such conversion of phenyl, reacting with PC_3H_4, C_3H_6, C_2H_4, and CH_3, totals to 9.20%, while the similar conversion by reacting with C_2H_2 accounts for 1.5% of the benzene formation. Moreover,

the propargyl recombination reaction, $C_3H_3+C_3H_3(+M)\rightarrow C_6H_6$, and the acetylene pathway, $C_2H_2+C_4H_4\rightarrow C_6H_6$, contribute 24.42% and 0.26%, respectively. The reaction pathway from methylcyclopentadiene also shows a 2.9% contribution. It has to be pointed out that the fulvene chemistry is not considered in the POLIMI mechanism, and hence is not shown here.

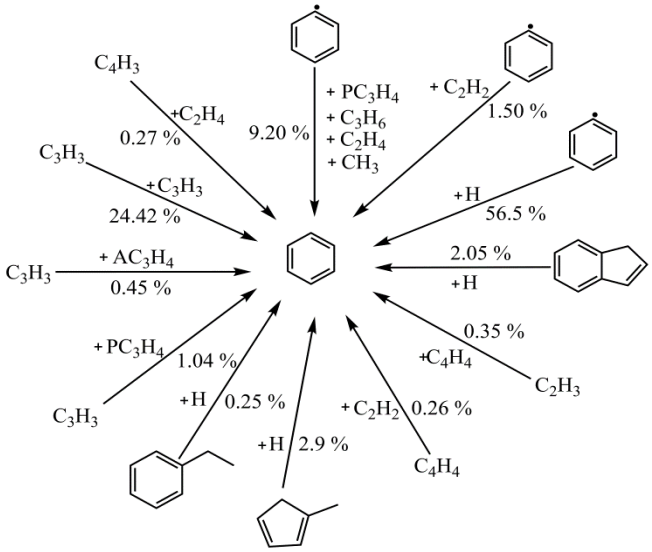

(a)

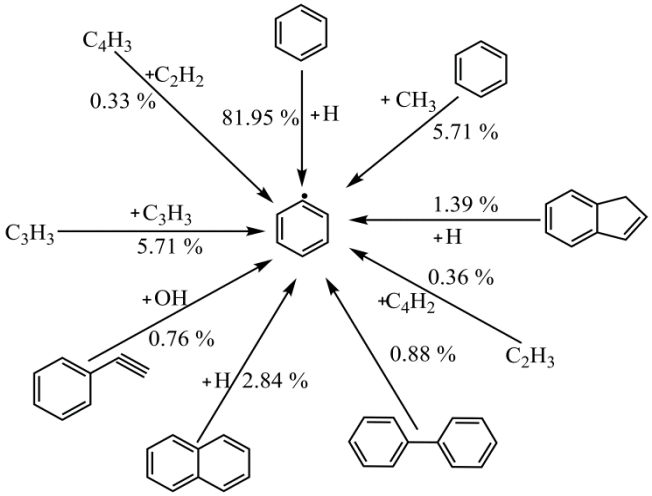

(b)

Figure 4.14: Kinetic pathways of formation of (a) A_1 aromatics (benzene, C_6H_6) and (b) A_1 aromatic radicals (phenyl, C_6H_5), showing percentage contributions through various reactions based on the POLIMI mechanism [4-7]. Conditions: *n*-butane, $X_F = 0.29$, $X_{O2} = 0.90$, and $K = 57$ s^{-1}.

At first glance Fig. 4.14(a) seems to suggest that the main formation of the benzene is from the phenyl at 56.5%. However, it can be seen from Fig. 4.14(b) that there are reaction channels, converting the phenyl back to the benzene, in a significant portion. In particular, in the phenyl formation pathways shown in Fig. 4.14(b), the conversion from benzene by reacting with H and CH_3 contribute 81.95% and 5.71%, respectively. As the precursor species, including propargyl, acetylene, etc., are the fundamental building blocks in the aromatic formation process [89], they are expected to make major contributions. Therefore, apart from the inter-conversion reactions, the most important pathway of benzene formation is from propargyl. Similarly, in the phenyl formation, Fig. 4.14(b) shows that $C_3H_3+C_3H_3 \rightarrow C_6H_5+H$ and $C_4H_3+C_2H_2 \rightarrow C_6H_5$ contribute 5.71% and 0.33%, respectively, with the propargyl pathway being more significant. These results indicate that for the first aromatic ring formation process in the POLIMI mechanism, the propargyl pathways are dominant as compared to the acetylene pathways.

The simulated results shown in Figs. 4.15–4.17 further illustrate that the major pathways in the POLIMI mechanism for the PAH growth to the 2-, 3-, and 4-ring aromatics, are through the odd-carbon-atom pathways, as indicated by the solid arrows for the first level pathways and the dashed arrows for the second level pathways. It is noted that the species in the second level originate mostly from the odd-carbon-atom pathways, which are described in details in the following discussion.

It is seen from Fig. 4.15(a) that for the A_2 ring, naphthalene ($C_{10}H_8$), the major formation pathways, apart from the stabilizing inter-conversion reactions, are through the methylnaphthalene pathway, $C_{10}H_7CH_3+H \rightarrow C_{10}H_8+CH_3$, and the methylnaphthalene radical pathway, $C_{10}H_7CH_2+CH_3 \rightarrow C_{10}H_8+C_2H_4$, contributing 14.66% and 4.2%, respectively. In addition, the pathway analysis to the second level shows that methylnaphthalene ($C_{10}H_7CH_3$) and

methylnaphthalene radical ($C_{10}H_7CH_2$) are formed from the odd-carbon-atom pathways. For example, in the methylnaphthalene formation, phenyl plays an important role and mostly forms from propargyl, as discussed in Fig. 4.14. Another example as seen in the methylnaphthalene radical formation is that a major pathway is through the reaction of phenylacetylene radical ($C_6H_4C_2H$) with propargyl. Figure 4.15(a) also shows the other two important pathways contributing to the A_2 ring naphthalene formation that involves propargyl radical, namely its reaction with the phenylacetylene radical (1.54%) and its reaction with the benzyl radical (1.31%). On the other hand, the acetylene pathway, $C_2H_2+C_6H_5C_2H \rightarrow C_{10}H_8$, contributes only 0.61% to the A_2 ring naphthalene formation. Hence, in comparative terms the propargyl is a dominant precursor as compared to the acetylene.

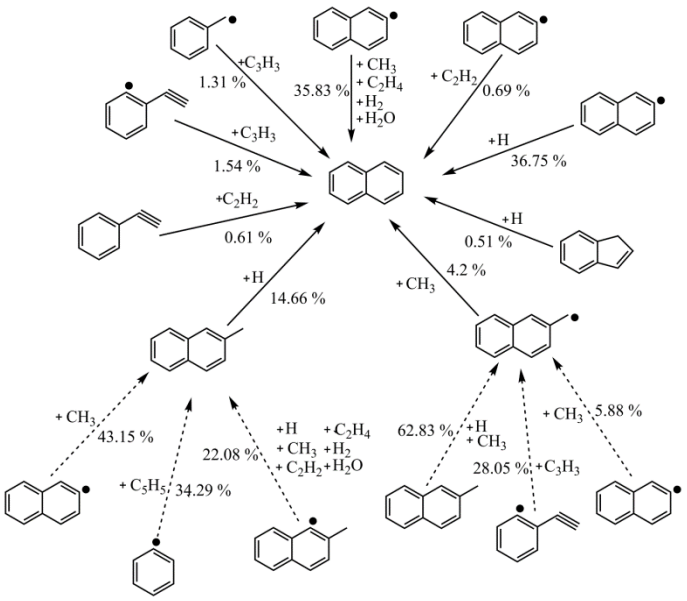

(a)

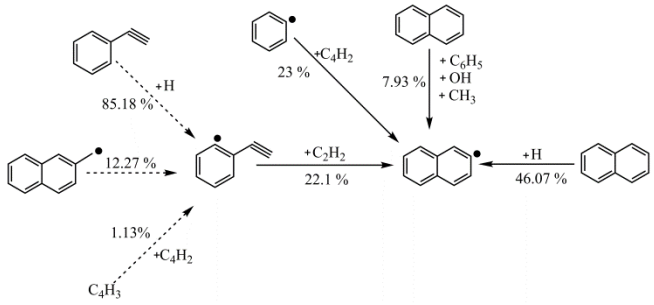

(b)

Figure 4.15: Kinetic pathways of formation of (a) A_2 aromatics (naphthalene, $C_{10}H_8$) and (b) A_2 aromatic radicals (naphthyl, $C_{10}H_7$), showing percentage contributions through various reactions based on the POLIMI mechanism [4-7]. Conditions: *n*-butane, $X_F = 0.29$, $X_{O2} = 0.90$, and $K = 57$ s^{-1}. Solid arrows show the first level of path analysis and dashed arrows show the second level of path analysis.

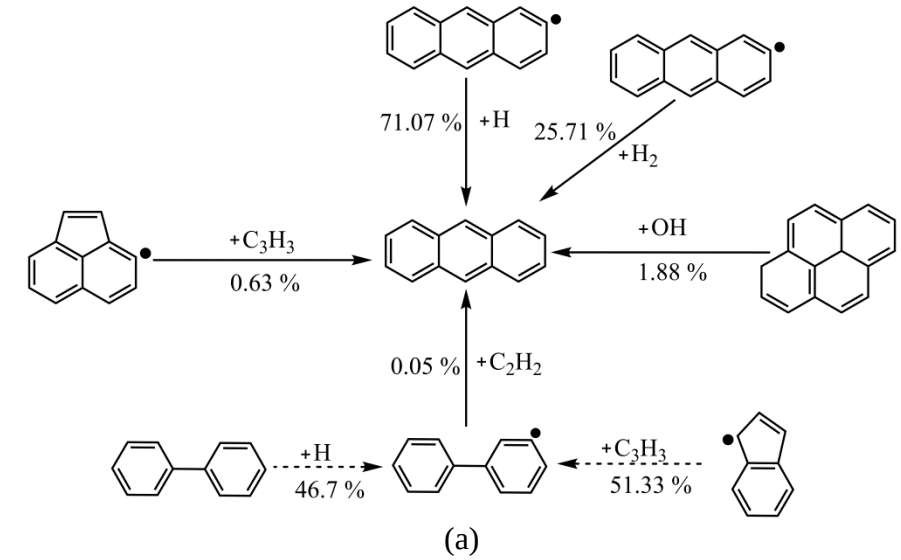

(a)

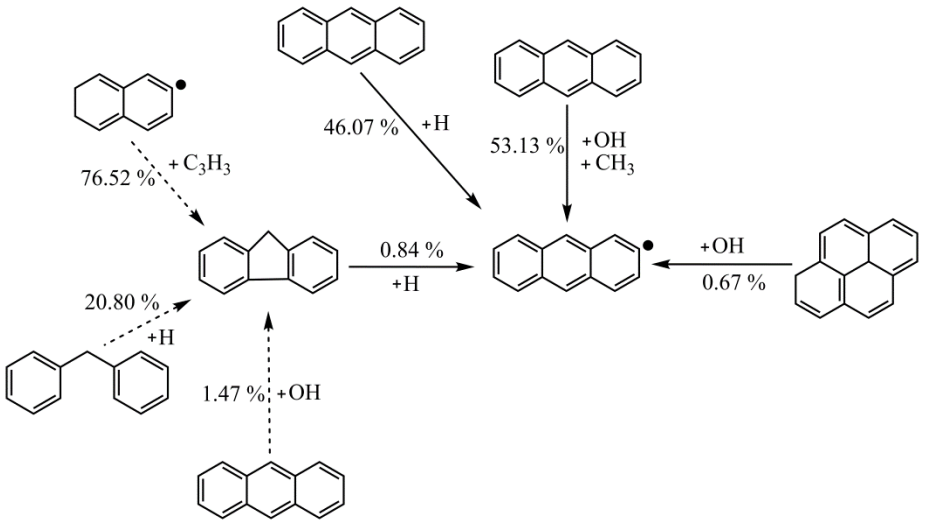

(b)

Figure 4.16: Kinetic pathways of formation of (a) A_3 aromatics (anthracene, $C_{14}H_{10}$) and (b) A_3 aromatic radicals (anthracenyl, $C_{14}H_9$), showing percentage contributions through various reactions based on the POLIMI mechanism [4-7]. Conditions: *n*-butane, X_F = 0.29, X_{O2} = 0.90, and K = 57 s^{-1}. Solid arrows show the first level of path analysis and dashed arrows show the second level of path analysis.

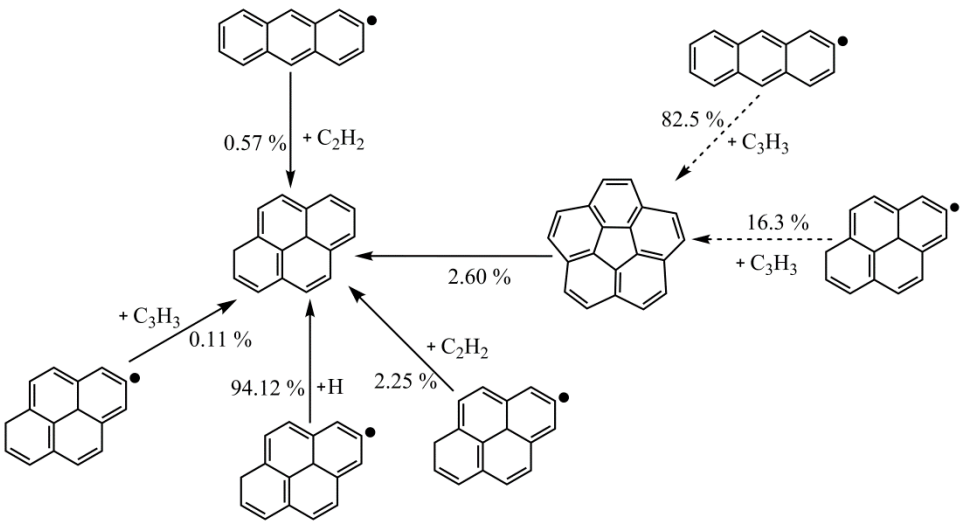

(a)

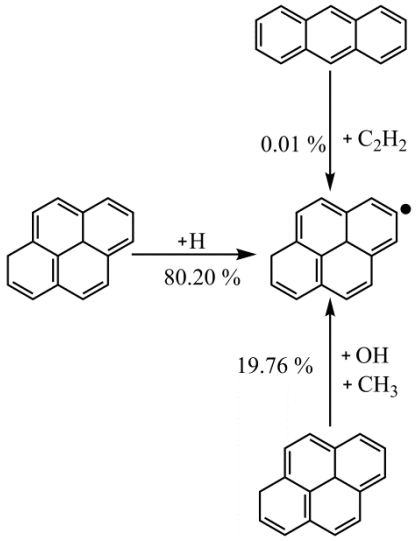

(b)

Figure 4.17: Kinetic pathways of formation of (a) A_4 aromatics (pyrene, $C_{16}H_{10}$) and (b) A_4 aromatic radicals (pyrenyl, $C_{16}H_9$), showing percentage contributions through various reactions based on the POLIMI mechanism [4-7]. Conditions: *n*-butane, $X_F = 0.29$, $X_{O2} = 0.90$, and $K = 57$ s^{-1}. Solid arrows show the first level of path analysis and dashed arrows show the second level of path analysis.

For the naphthyl radical ($C_{10}H_7$) formation shown in Fig. 4.15(b), apart from the stabilizing inter-conversion reactions, the pathway originating from the phenyl contributes to 23%. Again, the phenyl mostly forms from the propargyl. The other important step of acetylene addition has 22.1% contribution through the reaction of $C_6H_4C_2H+C_2H_2 \rightarrow C_{10}H_7$. The phenylacetylene radical involved in this reaction is formed through the decomposition of methylnaphthalene radical, which is formed via a major propargyl pathway discussed earlier.

Figure 4.16(a) shows the results for the A_3 ring anthracene formation. It is seen that a minute 0.05% contribution is from the acetylene addition reaction of $C_{12}H_9+C_2H_2 \rightarrow C_{14}H_{10}+H$. Further analysis to the second level shows that in this reaction, the biphenyl radical ($C_{12}H_9$) is formed through the reaction where the propargyl is added to the indenyl. The other pathway in the A_3 formation is from the A_4 aromatic pyrene ($C_{16}H_{10}$), which is shown in Fig. 4.17(a) to originate from the reactions involving propargyl. In addition, the pathway of acenaphthylene radical ($C_{12}H_7$) reacting with the propargyl, $C_3H_3+C_{12}H_7 \rightarrow 0.5C_{14}H_{10}+0.5C_{16}H_{10}$, contributes to 0.63%. Hence, the dominance of the propargyl can be seen in the A_3 formation as well. Similarly, the anthracenyl ($C_{14}H_9$) formation, as shown in Fig. 4.16(b), involves the propargyl pathways. From Fig. 4.17(a), it can be observed that, apart from the stabilizing inter-conversion reactions, the A_4 ring pyrene formation is mainly through the reaction pathways that include propargyl, while the acetylene has 0.57% contribution from the acetylene addition reaction of $C_{14}H_9+C_2H_2 \rightarrow C_{16}H_{10}+H$. It is also noted in the POLIMI mechanism that the pyrenyl ($C_{16}H_9$) formation is mostly governed by the inter-conversion stabilization pathways, as shown in Fig. 4.17(b).

For the binary fuel blends studied here, the above-mentioned important reactions are expected to show more contributions in the PAH formation, as the experimental results

demonstrated the synergistic effects. Although at the inception stage the role of propargyl should be the dominant determinant of the PAH formation [71, 179], other pathways from the acetylene cannot be entirely ruled out [8, 76-80]. As previously shown in Figs. 4.10-4.13, the calculated peak mole fractions of the propargyl, benzene, naphthalene, anthracene, and pyrene increase with increasing β, but that of the acetylene decreases as the amount of straight chain isomer decreases. From the path analyses, it is clear that the major PAH pathways in the POLIMI mechanism [4-7] basically involve the odd-carbon-atom pathways. However, the experimental results from Fig. 4.9 show the synergistic effects, which are not predicted by the simulations. This discrepancy could be explained by the possibility that the acetylene addition reactions, as well as those beyond the HACA mechanism, also have significant contributions in the PAH formation. Based on the current experimental findings, it is suggested that the increased contributions of the acetylene addition reactions in the PAH formation can improve the comprehensiveness of the underlying reaction mechanism. To further develop these PAH-related chemistries to predict the larger aromatic ring PAHs, beyond the current A_4-ring in the POLIMI mechanism [68-71], the inclusion of the acetylene addition reactions (and possibly other new pathways) for the larger PAHs should be considered important, at least for the straight chain fuels.

Chapter 5: Soot and PAH formation in ethylene flames at elevated pressures

5.1 Introduction

There have been various soot models developed to study soot formation at elevated pressures. These models are either semi-empirical or employ simplified acetylene based reaction mechanisms [228]. As the fundamental understanding of soot formation processes, even at atmospheric pressure, is still lacking, these models are not versatile in applications. More information on physically relevant conditions, such as at higher pressures, is required to improve these soot models. In the past, studies of soot formation at elevated pressures have been conducted in laminar premixed [112, 134, 229-231] and non-premixed [102, 232-237] flames. These studies are aimed to obtain a relationship between the soot volume fraction (f_v) and pressure (P), which is given by, $f_v \propto P^n$, where n is pressure scaling factor. Pressure scaling factor, n is define by the power law dependence of soot volume fraction on pressure [238]. Lee and Na [235], using the two-color pyrometry, measured soot concentrations, at a pressure range of 1–4 atm, in co-flow non-premixed flames of air as oxidizer and pure ethylene. They reported a quadratic dependence on the pressure of the maximum local soot volume fraction at a height of 20 mm and above the burner nozzle exit [235]. Flower and Bowman [232, 233] used a co-flow laminar non-premixed ethylene flame at pressure range of 1–10 atm to measure the soot volume fraction using the line-of-sight light extinction (LE) diagnostic method, and reported a pressure scaling factor of n=1.2 ± 0.1. Radially-resolved soot concentration and soot temperature measurements have been reported by Thomson *et al.* [239] in laminar non-premixed co-flow methane flames up to the pressure of 40 atm, using the soot emission spectroscopy and line-of-

sight attenuation techniques, and the authors obtained a quadratic pressure scaling. McCrain and Roberts [102] investigated the formation of soot at elevated pressures up to 25 atm in methane–air coflow non-premixed flames and up to 16 atm in ethylene–air coflow non-premixed flames. They employed the laser induced incandescence (LII) technique to measure the soot volume fraction. It was noted that the flame gets narrower with increasing pressure, and the local peak soot volume fraction has been found to scale with pressure for the flames. McCrain and Roberts [102] noticed that the integrated soot volume fraction, at an axial location, scaled with pressure with n=1.0 and n=1.2 for methane–air and ethylene–air flames, respectively. In addition, the region of local peak soot volume fraction was found to shift from the wings of the flame to the tip with increasing pressure for both methane–air and ethylene–air flames [102]. It was found that the local peak soot volume fraction scaled with pressure for the methane–air flames with n=1.2 and for the ethylene–air flames with n=1.7 [102]. Hence, the pressure dependence of soot volume fraction based on the local maximum is considerably different than that determined from the integrated value in the ethylene–air flames [102]. Zhou *et al.* [238] conducted the LII soot volume fraction measurements in laminar non-premixed co-flow *n*-heptane flames over a pressure range spanning from 1.0 to 3.0 bar. While the oscillations of the height of the flame tip was less than 1 mm in this setup, they observed that the oscillations of the flame tip increased with increasing pressure. On the other hand, the flame tip height based on soot structure decreased slightly with increasing pressure, and, somewhat unexpected, the natural luminosity showed a slightly higher flame than that determined by the LII signals. While the pressure plays an important role in enhancing the combustion intensity, it has been reported that the pressure scale factor of soot formation is in the range of 0.6–2.4 [112, 234, 240, 241].

Most of these literature studies at elevated pressures have been conducted in co-flow non-premixed flame conditions. However, these flame configurations are two-dimensional and require significant computational resources to accurately model them. In contrast, a counterflow flame configuration is quasi-one-dimensional in nature, facilitating simulations with detailed chemistry and soot modeling [240, 242-245]. To our knowledge only few studies have been conducted to measure PAHs at elevated pressure conditions [171]. Most of the literature studies to measure PAH profiles were conducted at atmospheric conditions, including those in premixed flames [96, 246-248], co-flow non-premixed flames [95, 249-252], and counterflow non-premixed flames [240, 242, 253-256]. Hence, in this chapter, combining soot and PAH measurements at elevated pressure conditions, for ethylene flames, is of fundamental interest.

5.2 Test matrix

Table 4 lists experimental conditions investigated in this study. The bulk velocities of $V_0 = V_L =$ 82.5, 41.25, 27.5, 20.625, 16.5, and 13.75 cm/s were used to maintain K'=300 s^{-1} for P=1, 2, 3, 4, 5, and 6 atm, respectively. The fuel stream was composed of ethylene and nitrogen, with the mole fractions of ethylene, X_F, varied from 0.20 to 0.40. The mole fractions of oxygen and nitrogen in the oxidizer stream were kept constant at X_{O_2}=0.21 and X_{N_2}=0.79, respectively. The exit temperatures of the fuel and oxidizer nozzles were maintained at 300 K. For K'=300 s^{-1} and a given set of X_F and X_{O_2}, the maximum flame temperatures, T_{max}, within the investigated pressure range, simulated using the WF-PAH mechanism [8], are also shown in Table 4. It is seen that T_{max} increases with increasing pressure. Figure 5.1 shows the comparison of the flame structure variations at P=1, 4, and 6 atm by plotting the profiles of temperature, mole fractions of

ethylene and oxygen, and mass flux, for the case of X_F=0.20 and K'=300 s^{-1}. By keeping pressure-weighted strain rate constant, it is seen from Fig. 5.1 that the overall flame thickness in terms of temperaturte profile is unchanged and the profiles of mass flux, ethylene mole fraction, and oxygen mole fraction entering the flame are almost identical. These comparisons justify this method of pressure-weighted strain rate to control the overall flame structure/thickness, which will be further demonstrated later by comparing the current experimental results.

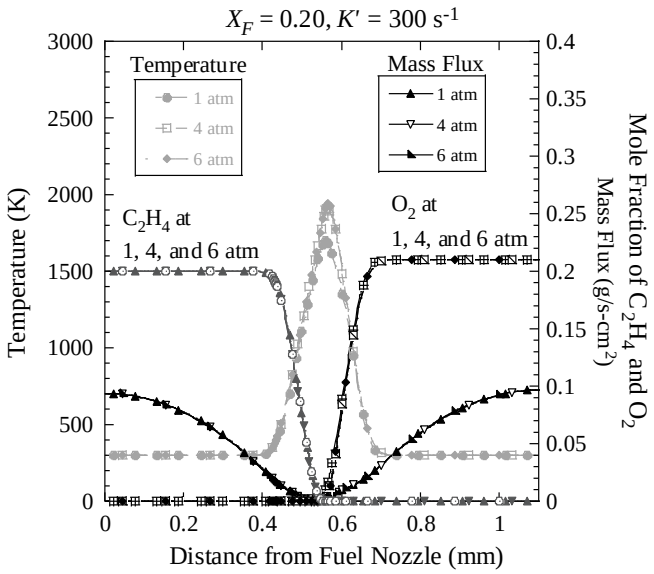

Figure 5.1: Simulated temperature and velocity profiles, using USC-PAH mechanism [8], for ethylene flames at P = 1, 4 and 6 atm, demonstrating the same flame width with variation in pressure.

Table 4: Experimental conditions, simulated maximum flame temperatures (T_{max}) in the given counterflow conditions, and calculated stoichiometric mixture fractions (Z_{st}) for ethylene flames.

Fuel Stream		**Oxidizer Stream**		**Pressure Range (atm)**	**Maximum Flame Temperature Range T_{max} (K)**	**Stoichiometric Mixture Fraction Z_{st}**	**Pressure-weighted Strain Rate K' (s^{-1})**
X_F	X_{N_2}	X_{O_2}	X_{N_2}				
0.20	0.80	0.21	0.79	1–6	1699–1944	0.268	300
0.30	0.70	0.21	0.79	1–6	1822–2072	0.197	300
0.40	0.60	0.21	0.79	1–6	1889–2144	0.156	300

5.3 Calibration of LII measurements

It is important to determine the calibration factor for LII at elevated pressures. In Fig. 5.2(a) and Fig. 5.2(b), the spatial distribution profiles of soot volume fraction measured using the LII and LE technique using abel's inversion, as described in [131], have been shown for the sooting ethylene flame under the conditions of X_F=0.20, P=2 atm, and K'=300 s^{-1} at five axial locations (z) from the bottom fuel nozzle. The calibration of ethylene flames at atmospheric pressure has been demonstrated in our earlier study [131].

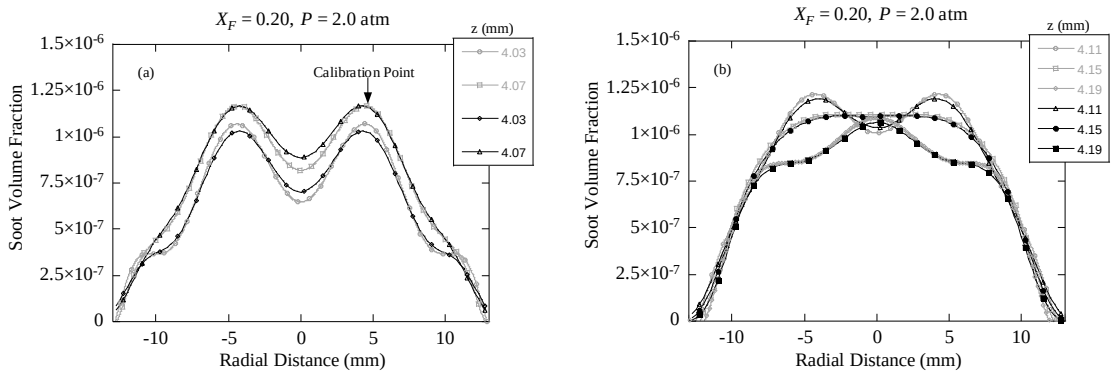

Figure 5.2: Comparison of soot volume fraction distributions in counterflow nonpremixed ethylene flame measured using LE and LII. (a) soot formation zone (b) soot decomposition and oxidation zone, where z represents the distance from the fuel nozzle. Conditions: X_F = 0.20, P = 2 atm, and $K^{'}$=300 s^{-1}. Solid symbols/black lines are for LE measurements using abel's inversion and hollow symbols/gray lines are for LII measurements.

With increasing z, Fig. 5.2(a) and Fig. 5.2(b) show the results in the soot growth and soot decomposition regimes, respectively. At the 'Calibration Point' for z=4.07 mm indicated in Fig. 5.2(a), the LII signal was compared with the quantitative measurement of soot volume fraction using the LE technique. The refractive index used for the current measurements is $m = 1.57 - 0.56i$, which is widely used in the literature [130, 131, 141]. The choice of refractive index was based on generally accepted value by the research community and was chosen so that comparisons could be drawn [142-146, 148]. In our previous study [131], the choice of this refractive index $m = 1.57 - 0.56i$ has been discussed in detail and compared with other refractive indices of $m = 1.90 - 0.55i$ [150] and $m = 1.75 - 1.03i$ [151]. A calibration factor of 3.01×10^8 for LII was then calculated based on the LE results, which was found to be very similar to the calibration factor of 3.05×10^8 determined with a sooting ethylene flame at atmospheric pressure. The similar calibration factor was attained by increasing the camera gain as specified earlier in Section 3.2. These calibration factors are system dependent and also depend on the variou parameters such as gate width, gate delay, gain etc. chosen for the experiments. The agreement of the LE and LII profiles demonstrate that there is no influence of pressure on the calibration process, which is consistent with the previous literature studies [106, 134], due to an insignificant change in the soot morphology, particle diameter, and soot composition at elevated pressures as explained by [106]. Using the calibration factor, the quantitative values for the LII signals at other radial-axial locations were then determined. It is seen from Fig. 5.2 that the radial distributions of soot volume fractions obtained from both the LII and LE techniques compare well for all the axial locations. Furthermore, the LII profiles shown in Fig. 5.2 are as symmetrical as the LE profiles. This symmetry of the LII profiles

demonstrates that the laser fluence employed herin is sufficient and adequate at elevated pressures.

5.4 LII and PAH-PLIF results

Combination of PAH-PLIF signals and LII signals can provide the information about the structural locations of the PAH formation and soot layer in the flame. In order to assess the pressure effects on soot formation of ethylene flames, soot volume fraction and PAH profiles for these flames were measured and compared at constant pressure-weighted strain rate. The exit temperatures of the fuel and oxidizer nozzles were maintained at 300 K. Moderately sooting flame conditions were chosen in this study, as the LII and PAH-PLIF measurement techniques are not suitable for heavily sooting flames. This is because that under heavily sooting conditions the laser fluence may not be sufficeint for the entire measurement domain due to the absorption of the laser power by the soot particles. For LII in particular, this leads to the difficulty in maintaining the required laser fluence threshold for the whole region of interrogation. It is also noted that for lightly sooting flames, the sparse density of soot particles results in weaker LII signal strength, which would not be sensitive enough for the LII measurements. For X_F=0.20, Fig. 5.3(a) and Fig. 5.3(b) show the experimental results at P=1 and 6 atm, respectively. Similarly, the experimental results shown in Fig. 5.3(c) and Fig. 5.3(d) are for X_F=0.30 at P=1 and 6 atm, respectively. And lastly, Fig. 5.3(e) and Fig. 5.3(f) present the experimental results for X_F=0.40 at P=1 and 6 atm, respectively. The PAH-PLIF signal profiles in Fig. 5.3 and the maximum PAH-PLIF measurements in the rest of the discussion, for the detection wavelengths of 334 nm, 400 nm, 450 nm, and 492 nm, were scaled by the maximum PAH-PLIF signal for X_F=0.20 and P=1 atm at 334 nm detection wavelength. This normalization basis was used in order to demonstrate the relative spatial locations of the PAH-PLIF profiles for different detection wavelengths (hence different aromatic ring sizes). On the other hand, the LII profile for

each flame shown in Fig. 5.3 was scaled with the maximum LII signal at X_F=0.20 at P=1, which therefore demonstrates the relative increase in the LII signal for other fuel loading and the pressure conditions.

As discussed earlier, the overall flame thickness has been maintained the same by keeping the pressure-weighted strain rate constant at K'=300 s^{-1} such that the effect of pressure on soot/PAH formation can be clearly elucidated. This is verified, as demonstrated in Fig. 5.3, that between the minimum (1 atm) and the maximum (6 atm) pressure ranges investigated in this study, the width of the PAH formation zone and sooting zone is similar for all the fuel mole fractions investigated. It has to be pointed out that considering the temperature sensitivity and concentration dependence of the PAH-PLIF signals from the aromatics of different ring sizes formed at different axial locations, the direct comparison of PAH-PLIF signals between two different detection wavelengths should be taken with caution. In addition, since the PAH-PLIF measurements have not been corrected for the quenching effect of pressure broadening, these results provide broad qualitative information. Considering these, for all the profiles in Fig. 5.3, it can be observed that with the increase in detection wavelength for PAH-PLIF these profiles shift away from the fuel nozzle and move closer to the LII profile. It can also be observed from Fig. 5.3 that for all the fuel mole fractions and pressure conditions, the PAH profiles are closer to the fuel side than the LII profile, indicating that PAHs grow from the fuel side. The results for all the flames also show that with the increase in detection wavelength the PAH-PLIF profiles move closer to the LII profile. This shift in PAH-PLIF profiles with increasing detection wavelength indicates that the longer (shorter) detection wavelength corresponds to the larger (smaller) aromatic ring size of PAH's, as previously observed by Lee *et al.* [158]. In Fig. 5.3, a comparison of the PAH-PLIF profiles across the flames for any of the detection wavelengths

shows that while their profile shapes appear similar, the maximum relative signal values vary. Such behavior can be associated with the effects of fuel mole fraction and pressure on the PAH and soot formation processes. The maximum relative signals of PAH-PLIF signals increase for each detection wavelength, with increase in pressure, indicating that the pressure inhances PAH formation. The comparison of the maximum relative signals of PAH-PLIF signals for all the detection wavelengths will be shown and discussed later. In general, the soot volume fraction profile can be divided into three zones, namely inception, growth, and oxidation for soot. The soot inception zone exists towards the fuel side, where the higher concentrations of soot precursors are present and initial aromatic ring formation of benzene, naphthalene, anthracene, etc, takes place. Further growth in soot is due to various parallel pathways of soot formation and growth, such as aromatic condensation, hydrogen-abstraction/carbon-addition (HACA), etc. Finally, the soot profiles decay after attaining a peak, which is due to the oxidation processes, decomposition of soot due to high temperature. Using the WF-PAH mechanism [8], the computed spatially-resolved temperature profiles have also been shown in Fig. 3 for the comparison. It can be noticed that the decay of soot volume fraction profiles occurs closer to the T_{max} location and towards the oxidizer side.

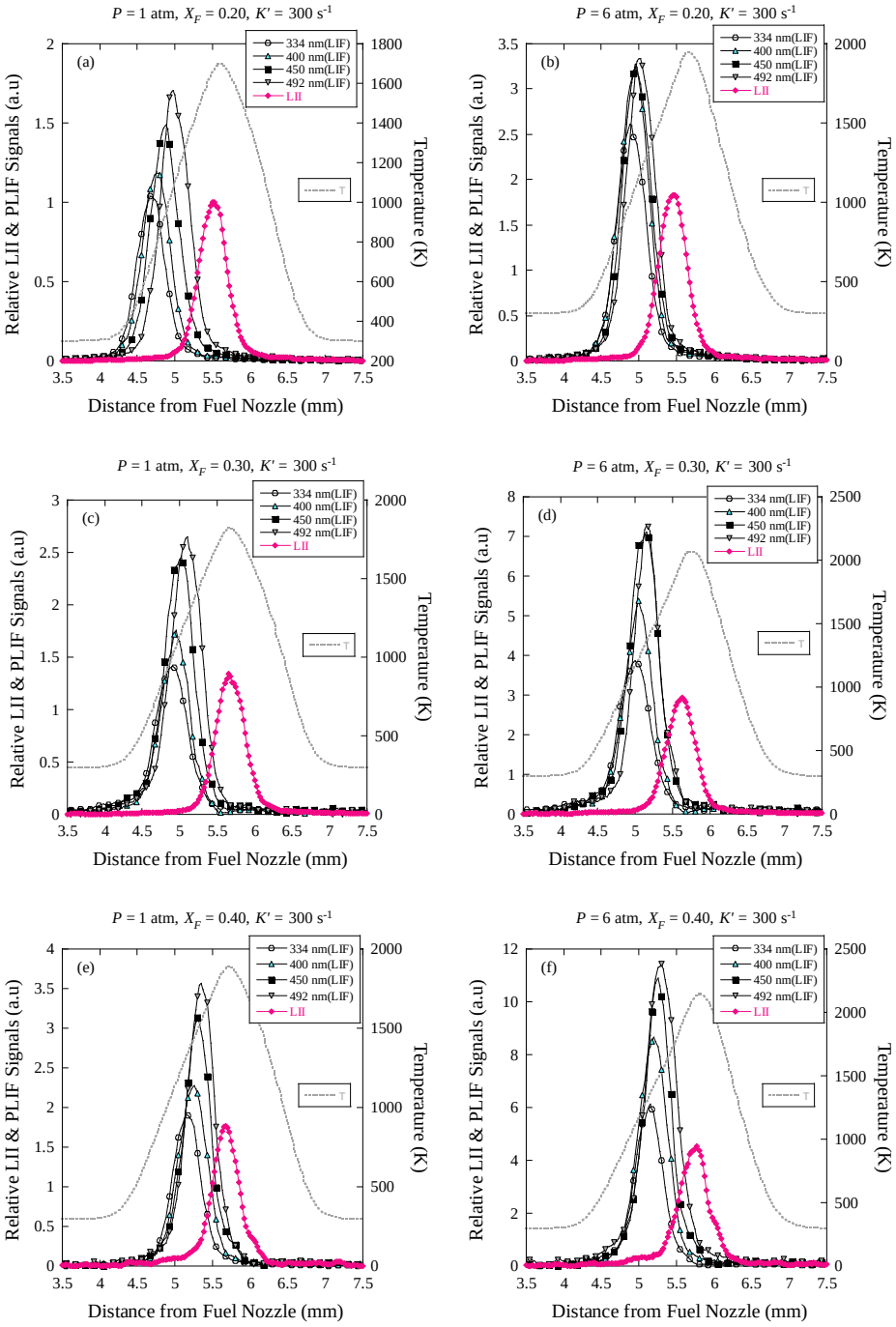

Figure 5.3: Spatial profiles of relative LII and PAH-PLIF (detection wavelengths of 334 nm, 400 nm, 450 nm, and 492 nm) signals, as well as the computed temperature profiles using the WF-PAH mechanism [8], along the centerline in the ethylene flames. Conditions: (a) X_F =0.20, P =1 atm, and $K^{'}$ =300 s^{-1} (b) X_F =0.20, P =6 atm, and $K^{'}$ =300 s^{-1} (c) X_F =0.30, P =1 atm, and $K^{'}$ =300 s^{-1} (d) X_F =0.30, P =6 atm, and $K^{'}$ =300 s^{-1} (e) X_F =0.40, P =1 atm, and $K^{'}$ =300 s^{-1} (f) X_F =0.40, P =6 atm, and $K^{'}$ =300 s^{-1} .

In order to understand the effect of pressure on the soot formation process, Fig. 5.4 shows and compares the soot volume fraction profiles along the centerline for all the sooting ethylene flames investigated, in the pressure range of P=1–6 atm and X_F=0.20–0.40. In Fig. 5.4, it can be noticed that the the width of the sooting zone with increase in pressure remains similar, which again justifies the formulation of keeping pressure-weighted strain rate constant to isolate the pressure effect on the soot formation process. With increase in the pressure, it can be observed that the maximum soot volume fraction value increases. Furthermore, the experimental results shown in Fig. 5.4 provide benchmark datasets for the development and validation of comprehensive soot models.

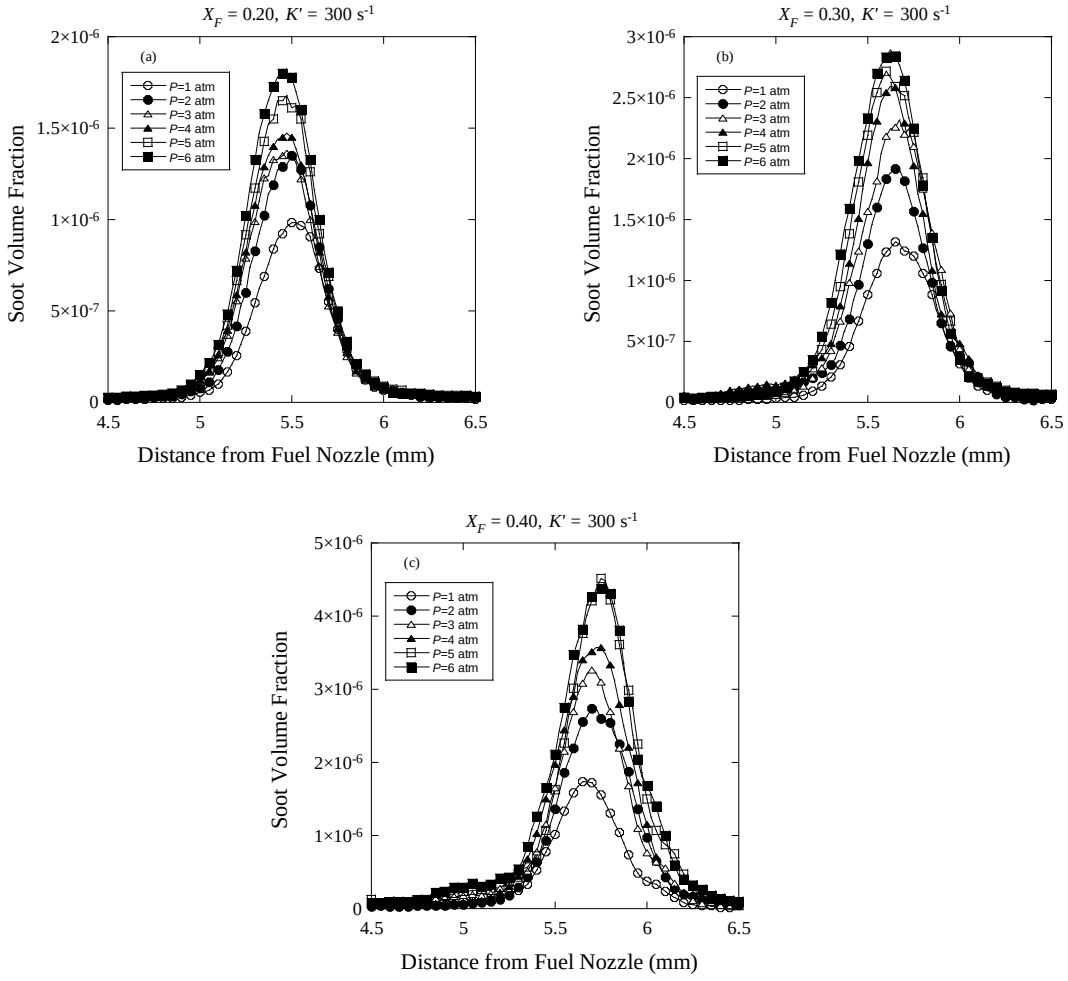

Figure 5.4: Spatial profiles of quantitative soot volume fraction, along the centerline in ethylene flames. Conditions: (a) X_F =0.20, P =1-6 atm, and $K^{'}$ =300 s^{-1} (b) X_F =0.30, P =1-6 atm, and $K^{'}$ =300 s^{-1} (c) X_F =0.40, P =1-6 atm, and $K^{'}$ =300 s^{-1}.

The effect of pressure on the maximum soot volume fraction along the centerline is shown in Fig. 5.5 for ethylene flames under the conditions of X_F=0.20–0.40, P=1–6 atm, and K'=300 s^{-1}. The pressure dependences of the maximum soot volume fraction, $f_{v,max}$, and the spatially-integrated soot volume fraction, $f_{v,int} = \int_0^L f_v dz$, are demonstrated in Figs. 5.5(a) and 5.5(b), respectively. From Fig. 5.5, it can be noticed that for a fixed pressure, the maximum and integrated soot volume fraction values increase by an increase in the fuel mole fraction, due to the increase in the amount of soot precursor pool [238]. For a given X_F, it is seen that the amount of soot formation increases with increasing pressure. Similar behavior of increase in soot volume fraction with pressure has been observed by Flower and Bowman [232, 233], Lee and Na [235], and McCrain and Roberts [102] in co-flow non-premixed ethylene flames.

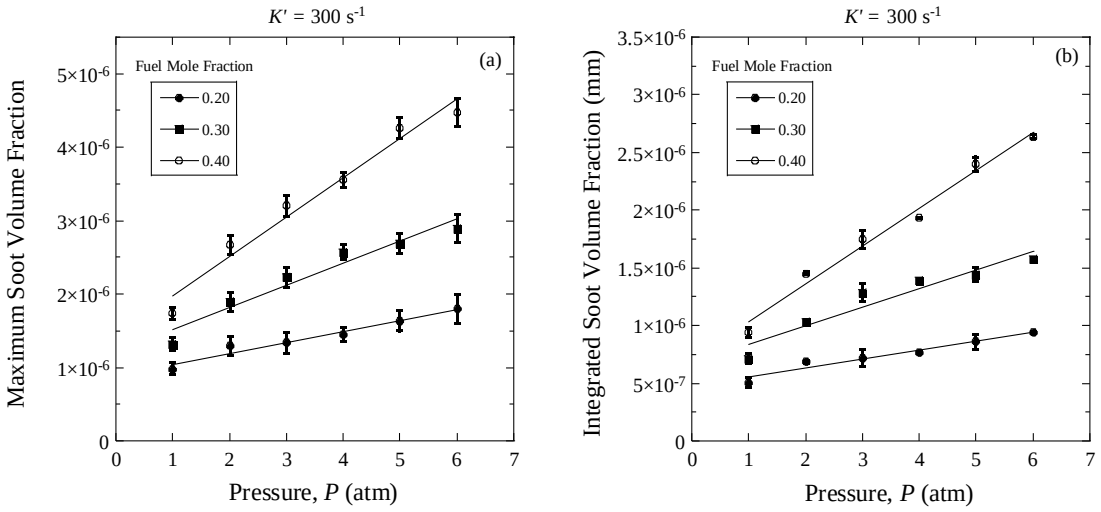

Figure 5.5: Maximum soot volume fractions along the centerline measured in ethylene flames for varying fuel mole fractions and pressures at $K^{'}$ =300 s^{-1}. Best fit straight lines are drawn to guide the discernment.

Figure 5.6 shows the qualitative comparison of the effect of pressure on 334 nm detection linked to A_2–A_3 formation, 400 nm detection linked to A_4 formation, and 450 and 492 nm detections linked to the larger aromatic ring PAH formation. The experimental results of maximum PLIF signals along the centerline shown in Fig. 5.6 are for the fuel mole fraction range of X_F=0.20–0.40, P=1–6 atm, and K'=300 s^{-1}. A consideration that should be taken is that the gate widths in these measurements have been kept the same across all the pressures, the pressure effect on the collection efficiency in reality differs. The effect of pressure in the fluorescence process is of decrease in the fluorescence signal due to the increase in quenching rates [257]. On the other hands, the increase in pressure is known to enhance the PAH formation process [98]. For each of the detection wavelengths, an increase in PAH-PLIF signal has been observed with the increase in the fuel mole fraction or pressure for each detection wavelength. This observation indicates that the pressure effect on the PAH formation process is stronger than the rate of quenching, hence these results qualitatively represent the pressure effect on the PAH process and hence the soot formation process. Due to this, these qualitative results should be interpreted with caution considering the errors in the measurements due to the aforementioned limitations of the LIF measurements.

To further investigate how the soot and PAH formation processes scale with the pressure, logarithmic calculations for both the LII and PAH-PLIF measurements have been conducted. The pressure scaling for soot volume fraction was determined by the following:

$$f_{v,max}/f_{vo,max} = \left(P/P_o\right)^n \quad \text{or} \quad f_{v,int}/f_{vo,int} = \left(P/P_o\right)^n, \tag{10}$$

where $f_{vo,max}$ ($f_{vo,int}$) is the maximum (spatially-integrated) soot volume fraction along the centerline at a reference pressure P_o and n is the pressure scaling factor. Here, P_o is set to 1 atm.

Logarithmic plots based on Eq. (10) and the results of Fig. 5.5 are shown in Fig. 5.7. These logarithmic plots are also used to draw a best fit straight line to determine the pressure scaling factors. A similar method of pressure scaling has been adopted by McCrain and Roberts [102].

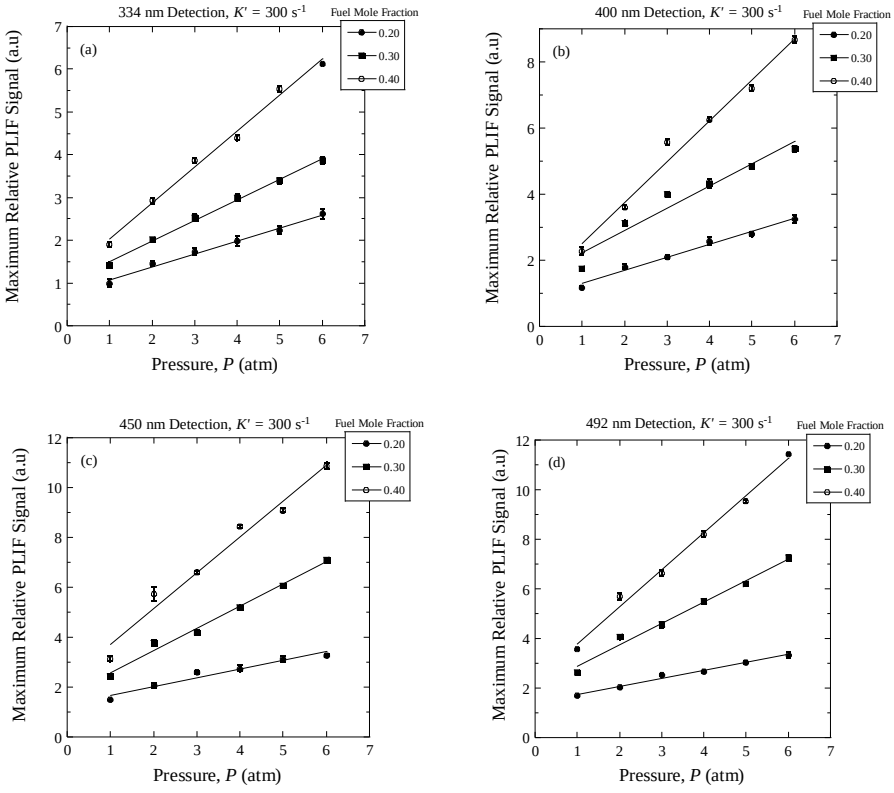

Figure 5.6: Maximum relative PAH-PLIF signals along the centerline in ethylene flames for varying fuel mole fractions and pressures at $K^{'}$ =300 s^{-1}: (a) 334 nm wavelength (A_2–A_3) detection, (b) 400 nm wavelength (A_4) detection, (c) 450 nm wavelength detection, (d) 492 nm wavelength detection. Best fit straight lines are drawn to guide the discernment.

Similarly, for the PAH-PLIF measurements the pressure scaling was determined by the following:

$$LIF_{max}/_{LIF_{o,max}} = \left(P/_{P_o}\right)^{n'}, \tag{11}$$

where LIF_{max} is the maximum relative PAH-PLIF signal along the centerline, $LIF_{o,max}$ is that at P_o=1 atm, and n' is the pressure scaling factor for PAH. Using Eq. (11) and the results of Fig. 5.6, the logarithmic plots for PAH-PLIF measurements at the detection wavelengths of 334 nm, 400 nm, 450 nm, and 492 nm are shown in Fig. 5.8. By drawing a best fit straight line, the corresponding pressure scaling factor n' for each measurement can be calculated.

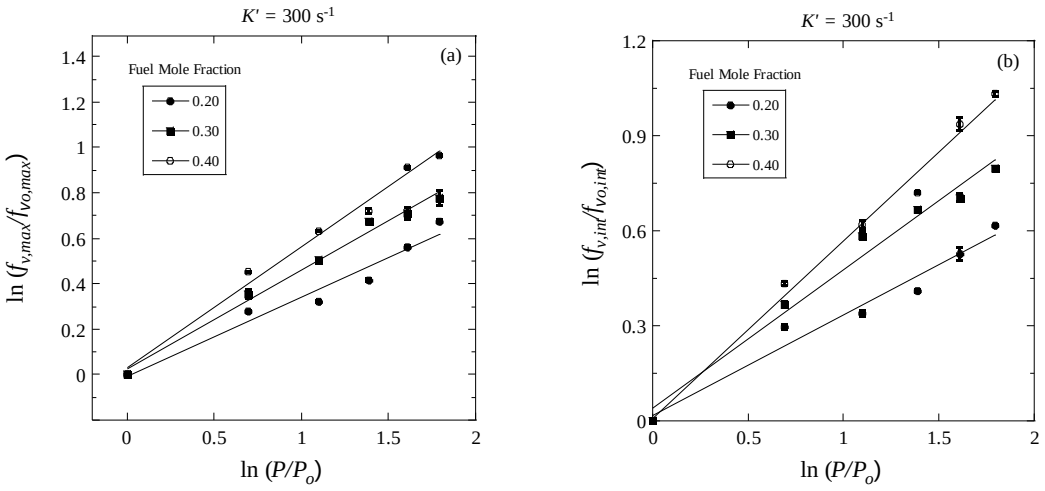

Figure 5.7: Logarithmic plot of relative (a) maximum and (b) spatially-integrated soot volume fraction variation with relative logarithmic pressure for different fuel mole fractions at $K^{'}$ =300 s^{-1}. Best fit straight lines are drawn to guide the discernment.

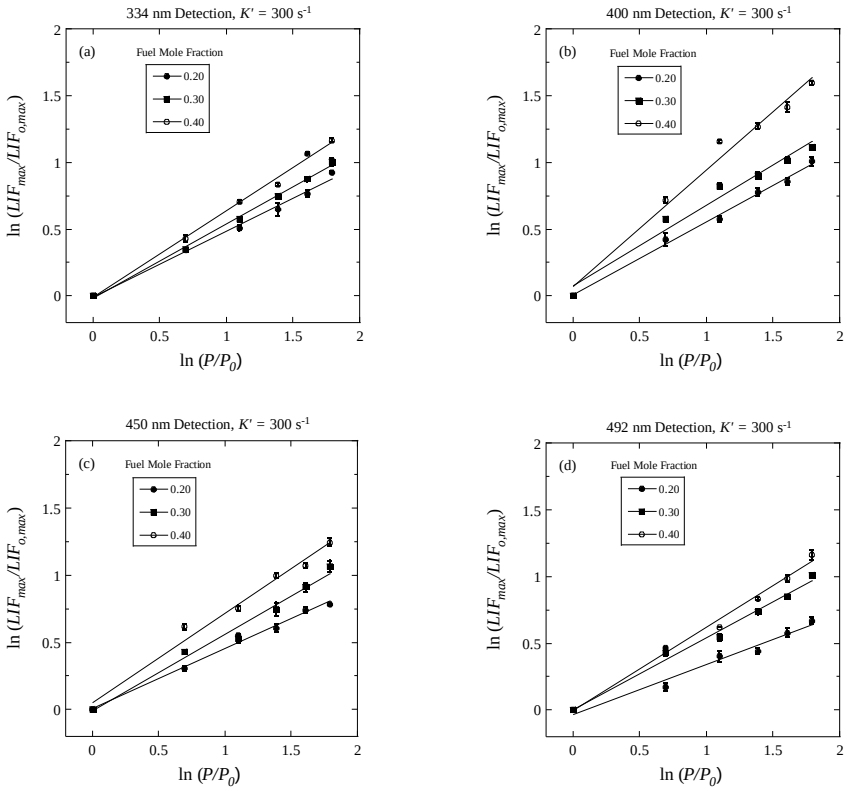

Figure 5.8: Logarithmic plots of relative maximum PAH-PLIF signal variation with relative logarithmic pressure for different fuel mole fractions at $K^{'}$ =300 s^{-1}: (a) 334 nm wavelength (A_2–A_3) detection, (b) 400 nm wavelength (A_4) detection, (c) 450 nm wavelength detection (d) 492 nm wavelength detection. Best fit straight lines are drawn to guide the discernment.

From Fig. 5.7 and Fig. 5.8, the deduced pressure scaling factors are summarized in Table 5, for soot volume fraction results and PAH-PLIF measurements at different detection wavelengths. It can be noticed that the PAH-LIF measurements show an increase in pressure scaling factor up to 400 nm detection wavelength followed by a decrease. For example, for X_F=0.20, the pressure scaling factor is 0.49 at 334 nm detection, increases to 0.55 at 400 nm detection, then it decreases to 0.44 at 450 nm detection, followed by a further decrease to 0.37 at 492 nm detection, finally for the soot volume fraction it decreases to 0.35. Similar trends have been observed for the other two fuel mole fraction measurements at X_F=0.30 and 0.40. In a study of co-flow non-premixed ethylene flames, McCrain and Roberts [102] reported the pressure scaling factors for their local maximum and path-integrated soot volume fractions are 1.7 and 1.2, respectively. However, the pressure scaling factors in the current study for soot volume fraction is <0.6. This discrepancy could be due to that the sooting behavior depends on the flame configuration in addition to the fuel type and structure [10]. It is also of interest to note that McCrain and Roberts [102] observed the trend of increasing soot yield and decreasing pressure scaling factor with increasing fuel flow rate. Since the current counteflow flames experienced higher strain rates than those in the typical co-flow flames, this could be a reason leading to lower pressure scaling factors in this study. The lower strain rates could not be tested in our experiments as that would limit the flame stability due to the wider flames resulting in the heat loss to the nozzles, as well as limitations of LII measurements due to higher soot loading.

Table 5: Experimentally-fitted pressure scaling factors for ethylene flames.

X_F	Pressure Scaling Factor					
	334 nm PAH-PLIF	**400 nm PAH-PLIF**	**450 nm PAH-PLIF**	**492 nm PAH-PLIF**	**Maximum Soot Volume Fraction LII**	**Integrated Soot Volume Fraction LII**
0.20	0.49	0.55	0.44	0.37	0.35	0.32
0.30	0.56	0.60	0.57	0.54	0.43	0.44
0.40	0.65	0.87	0.66	0.62	0.53	0.56

5.5 Simulated PAH results

From the experimental results, it has been observed that with an increase in pressure the PAH formation process is enhanced. Depending on the aromatic ring size of the measured PAHs, the pressure scaling factor varies. Using the WF-PAH mechanism [8], the species profiles of benzene, C_6H_6 (A_1-ring), naphthalene, $C_{10}H_8$ (A_2-ring), anthracene, $C_{14}H_{10}$ (A_3-ring), and pyrene, $C_{16}H_{10}$ (A_4-ring) were simulated. The investigated conditions in simulations are the same as that for the ethylene–air nonpremixed counterflow flame experiments, namely X_F=0.20–0.40, P=1–6 atm, and K'=300 s^{-1}. Since the experimental PAH-PLIF results are qualitative in nature and also measure all the PAHs in A_2–A_3 aromatic class with 334 nm detection wavelength and A_4 aromatic class with 400 nm detection wavelength [158, 256], a direct comparison with the simulated results cannot be made. The simulated results have been used to see the trends of pressure effect on aromatics formation process. Figure 5.9 shows these computed peak mole fractions of PAHs versus pressure. It is seen from Fig. 5.9 that all the calculated peak values of PAHs increase with increasing pressure. Figure 5.9(a) is plotted for the first aromatic ring A_1 (C_6H_6, benzene) formation. Although benzene profiles were not measured in the cuurent experiemnts, the computational results show an increase in the benzene formation with an increase in pressure. Figures 5.9(b) and 5.9(c) are plotted for the A_2 aromatics ($C_{10}H_8$, napththalene) and A_3 aromatics ($C_{14}H_{10}$, anthracene), respectively, which in the experimental

results are related to the 334 nm wavelength detection PAH-PLIF signals shown in Fig. 5.6(a). By comparison, both of these plots show a monotonic increase with pressure. Similarly, a qualitative comparison between the calculated A_4-ring PAH ($C_{16}H_{10}$, pyrene) in Fig. 5.9(d) and the experimental results in Fig. 5.6(b). As the increase in fuel mole fraction provides more precursor pools of PAH formation, it can be observed in all the cases, for a fixed pressure an increase in fuel mole fraction results in the increase of the amount of PAH formed.

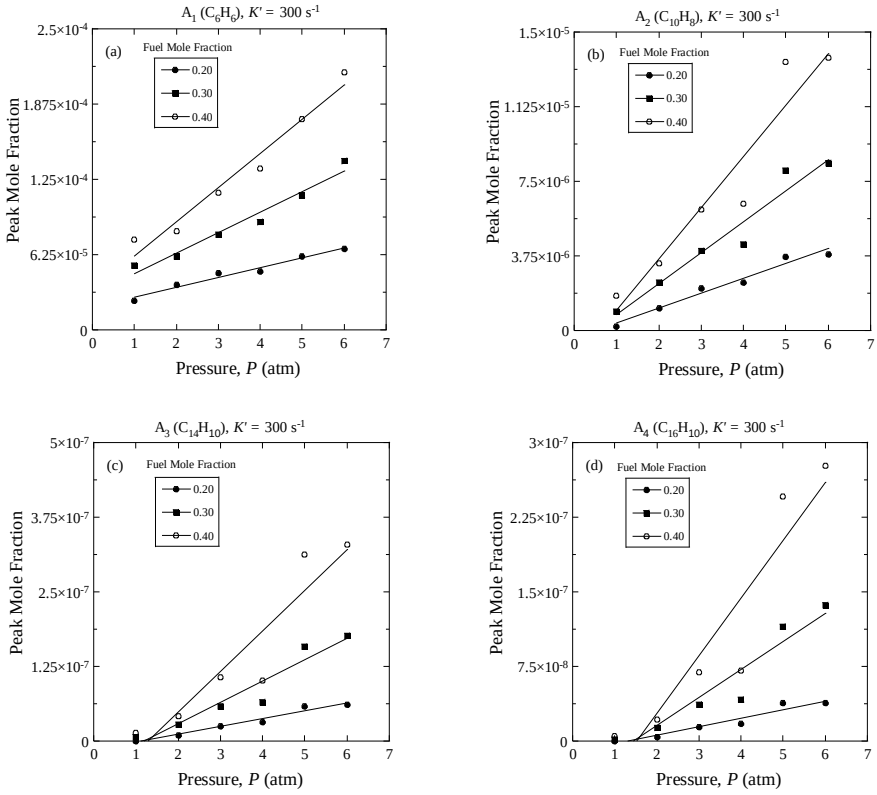

Figure 5.9: Variations of calculated peak mole fractions using the WF-PAH [8] mechanism in ethylene flames for varying fuel mole fractions and pressures at $K^{'}$ =300 s^{-1}: (a) A_1 aromatics (C_6H_6), (b) A_2 aromatics ($C_{10}H_8$), (c) A_3 ($C_{14}H_{10}$) aromatics, and (d) A_4 aromatics ($C_{16}H_{10}$). Best fit straight lines are drawn to guide the discernment.

To further investigate how the simulated peak mole fractions of aromatic species scale with the pressure, logarithmic correlations for these computed results have been conducted. The method of plotting them is similar to the one adopted for correlating the experimental results, using Eq. (11), where LIF_{max} has been replaced by the respective peak mole fraction M of the aromatic species and $LIF_{o,max}$ is replaced by M_o, i.e., the corresponding peak mole fraction at 1 atm pressure. The logarithmic plots have been shown in Fig. 5.10. Similarly, using these plots, the pressure scaling factors have been calculated and summarized in Table 6. While the pressure scaling factor values shown in Table 5 and Table 6 are different, similar increasing trend of pressure scaling factor from A_2 to A_4 is observed.

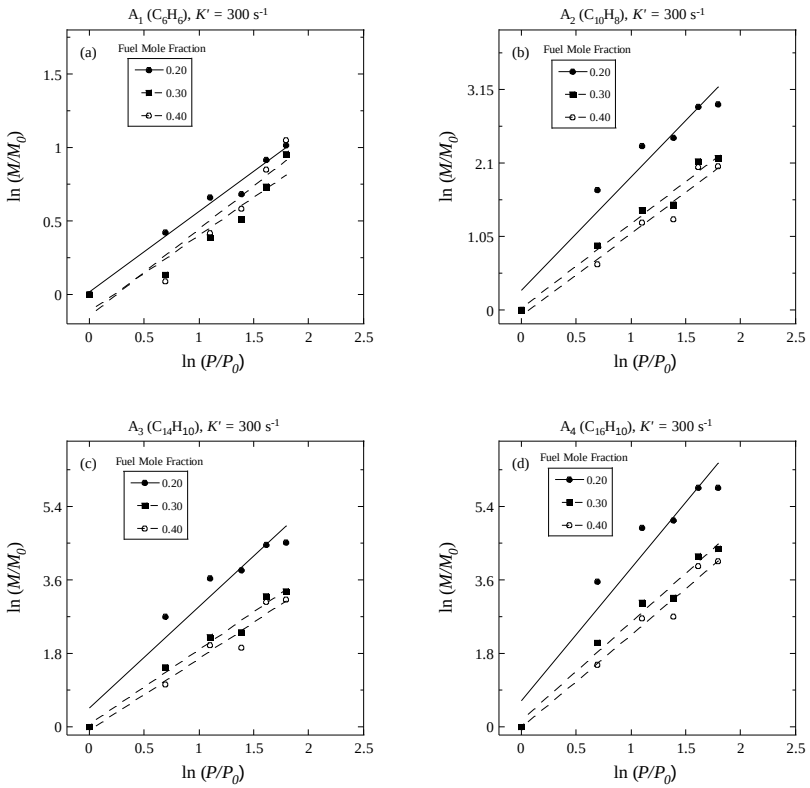

Figure 5.10: Variations of calculated relative logarithmic peak mole fractions using the WF-PAH [8] mechanism with relative logarithmic pressure for varying fuel mole fractions at $K^{'}$ =300 s^{-1}: (a) A_1 aromatics (C_6H_6), (b) A_2 aromatics ($C_{10}H_8$), (c) A_3 ($C_{14}H_{10}$) aromatics, and (d) A_4 ($C_{16}H_{10}$) aromatics. Best fit straight lines are drawn to guide the discernment.

Table 6: Simulation-fitted pressure scaling factors for peak aromatic species mole fractions in ethylene flames using the WF-PAH mechanism [8].

X_F	**Scaling factor, n**			
	A_1-ring (benzene, C_6H_6)	**A_2-ring PAH (naphthalene, $C_{10}H_8$)**	**A_3-ring PAH (anthracene, $C_{14}H_{10}$)**	**A_4-ring PAH (pyrene, $C_{16}H_{10}$)**
0.20	0.55	1.62	2.49	3.24
0.30	0.52	1.21	1.83	2.40
0.40	0.59	1.18	1.77	2.28

In Table 6, it can be seen that with the increase in the aromatic ring size the pressure scaling factor *n* increases which is consistent with our experiments. The simulated aromatics predict up to 4 aromatic rings, and in the experiments concluded in the Table 5, this is corresponds to the detection wavelength of 400 nm for which pressure scaling factor *n* increases. These factors are not similar, as in our experimental results, a class of aromatic ring sizes have been detected.

Chapter 6: Conclusions and future work

6.1 Accomplishments

In this dissertation, the work on optical diagnostics measurements of soot and PAH formation in butane and butanol isomers at atmospheric pressure and ethylene at elevated pressures, has been presented. Considering the importance of *in-situ* and *non-intrusive* optical diagnostic techniques the following are the key accomplishments:

1. The implementation of the optical diagnostic technique, laser induced incandescence (LII), capable of providing the quantitative measurements of soot volume fractions.

2. The implementation of the calibration technique, light extinction (LE), for the LII. The successful implementation of this technique has been demonstrated for liquid fuels (*n*-butanol), straight and structural fuels (ethylene and *iso*-butane) and at elevated pressure conditions (ethylene at 2 atm pressure).

3. The mapping of PAH formation using the planar laser induced fluorescence (PLIF) was successfully demonstrated by detecting PAHs at various detection wavelengths.

4. Under the counterflow non-premixed conditions, alternative fuels of butanol isomers were tested and were compared with butane isomers, by measuring soot volume fractions and PAHs.

5. The LII and LIF techniques were implemented at elevated pressures, which are relevant to the real engine operating conditions. Ethylene flames were tested for soot volume fractions and PAHs at elevated pressures.

6. Various chemical kinetic mechanisms were used to develop the understanding of the chemical kinetic pathways of fuel oxidation and PAH formation, by comparing the computational results with experimental measurements.

6.2 Conclusions

In the soot formation study presented in Chapter 3, atmospheric-pressure, non-premixed, sooting flames of butane and butanol isomers in a counterflow configuration were investigated. Laser diagnostics techniques were implemented to carry out quantitative measurements of soot volume fraction profiles. Due to the molecular structure effects, the sooting behaviors of fuels within the same isomeric class were found to differ. These differences were linked to different initial fuel breaking pathways pertaining to different C-C, C-H bond strengths within isomers. The presence of hydroxyl (-OH) group in butanol isomers was noted to affect the sooting behavior, as the butane isomers were found to produce more soot than butanol isomers for the conditions investigated. The effects of fuel mole fraction, oxygen mole fraction, and strain rate on soot formation were also investigated for these fuels. For the conditions studied, the sooting tendency ranking generally follows *n*-butane > *iso*-butane > *tert*-butanol > *n*-butanol > *iso*-butanol > *sec*-butanol. The counterflow non-premixed flames were also simulated using the gas-phase chemical kinetic models available in the literature to compute the spatially-resolved profiles of soot precursors, including acetylene and propargyl. However, the experimentally-observed sooting propensity ranking does not correlate well with the rankings for the computed peak mole fractions of soot precursors. These rankings may not correlate with each other as the soot formation and growth is a non-linear process. In addition, qualitative and quantitative dissimilarities in the computed mole fractions of soot precursors, as well as the differences in the

initial fuel breaking steps, predicted by the literature kinetic models are noted. Further chemical kinetic studies are needed to reconcile such discrepancies.

In the PAH formation study presented in Chapter 4, atmospheric pressure, non-premixed, sooting flames of the butanes and the butanols in the counterflow configuration were investigated to study the PAH formation, by using an optical diagnostic technique of planar laser-induced fluorescence for qualitative measurements of the PAHs with different aromatic ring sizes. The fuel structure effects on the PAH formation were observed, as within the same isomeric class the PAH formation tendencies differ. At the inception stage, the dominance of the propargyl pathways in the PAH formation was discussed based on the present experimental data and the simulated results using the POLIMI mechanism [4-7]. At the growth stage, the PAH formation ranking for the large PAHs formed just before the formation of soot particles was found to be consistent with the sooting tendency determined based on the peak soot volume fraction measured by the laser-induced incandescence (LII) technique. Additional experiments were conducted for the binary fuel blends by blending the branched chain isomer with the baseline straight chain isomer. Such experimental results revealed some synergistic effects and suggested the importance of the acetylene addition pathways to account for the synergy, which, however, were not shown in the simulations. It was further found through the path analyses that the contribution of the HACA mechanism in the PAH formation described in the POLIMI mechanism [4-7] plays a minimal role. Hence, in addition to the odd-carbon-atom pathways of PAH formation, the importance of the HACA routes, as well as other pathways beyond the HACA mechanism, for the large PAH formation should be considered in the chemical kinetic models, especially for the straight chain fuels.

The study of counterflow non-premixed sooting ethylene–air flames with fuel mole fractions of 0.20–0.40 in the pressure range of 1–6 atm were investigated experimentally with the laser diagnostic techniques of laser induced incandescence, planar laser induce fluorescence, and light extinction. A better understating of the quantitative soot formation process has been developed for ethylene counterflow flames under elevated pressure conditions. The effect of pressure on the formation of PAHs with different aromatic ring sizes has also been measured qualitatively. The pressure-weighted strain rate method which has been proposed in the literature was adopted to investigate the pressure effect solely. These flames have been shown, using the WF-PAH mechanism [8], to maintain similar overall flame width, thus isolating the pressure effect on the soot formation. Further experimental evidences, by comparing measured soot and PAH profiles, demonstrate similar structural width. With increase in pressure, the increase in soot volume fraction and PAH-LIF signals were observed. The pressure scaling factors for soot formation and PAH formation were deduced. A comparison of the pressure scaling factor for soot volume fraction with the literature study showed that in the counterflow non-premixed flames it was lower than the co-flow non-premized flames. This discrepancy could be due to the differences in flame configuration and the strain rate/flame curvature experienced by the flame. Since the PAH experimental measurements are qualitative in nature, measuring the A_2−A_3 and A_4 classes of the aromatics, a direct comparison of pressure scaling factors with the computed peak mole fractions of aromatic species, which include A_1 to A_4 aromatics, has not been made. However, both the experiments and computations demonstrate similar trends of increase in PAH formation with increasing pressure.

6.3 Future work

The work presented in the current dissertation is an initial demonstration of successful implementation of LII, LE and PLIF techniques in non-premixed counterflow configuration at atmospheric and elevated pressure conditions. This opens up numerous possibilities for the future:

1. The soot formation process is a complex phenomenon of various gas and solid phase chemistries involved in this process. The progress that has been made to understand the process of soot formation is that it is agreed that the soot formation process depends on the chemistry of the fuel pyrolysis and fuel structure [72]. Early understanding of soot formation was mostly believed by the H-abstraction-C_2H_2-addition (HACA) mechanism of the PAH formation and initial development of chemical kinetic mechanisms has been based on HACA [8, 76-80]. With further experimental investigations, the pathways involving propargyl, allyl, cyclopentadienyl, and indenyl have also been shown to contribute to the PAH formation processes [81-89]. In addition, the odd-carbon-atom pathways have been introduced as possible reaction routes of the incipient PAH formation, as the propargyl has been proposed to produce reasonantly stable benzene rings [91-95]. Having demonstrated the measurement of the PAHs and soot, using the efficient use of optical diagnostic techniques, in the future the research can be directed to provide a detailed mapping of soot and PAH formation pathways.

2. The demonstration of LII technique leads to the possibility of soot particle size measurements. The soot particle sizes can be measured by detecting the LII signals at two detection wavelengths. The LII temporal profiles for the spatial locations can be created which are dependent on the soot particle diameter and the detection wavelength. Having known these two detection wavelengths, the particle size distribution can be mapped in the sooting zone. The

information of soot particle size distribution is important in the development of surface chemistry of solid phase soot formation, such as the moment method of soot formation.

3. This study also leaves a possibility of studying various fuels such as jet fuels, diesel, esters, ethers etc. in the counterflow non-premixed flame configuration to understand fuel specific effects on the soot and PAH formation process. The sooting tendencies can be compared and ranked for butanols and their counterpart alkanes, for example the butane and butanol isomers were compared in this thesis.

References

1. Wang, H.; You, X.; Joshi, A. V.; Davis, S. G.; Laskin, A.; Egolfopoulos, F. N.; Law, C. K. *USC Mech Version II. High-Temperature Combustion Reaction Model of H2/CO/C1-C4 Compounds*. 2007.
2. Sarathy, S. M.; Vranckx, S.; Yasunaga, K.; Mehl, M.; Oßwald, P.; Metcalfe, W. K.; Westbrook, C. K.; Pitz, W. J.; Kohse-Höinghaus, K.; Fernandes, R. X., A comprehensive chemical kinetic combustion model for the four butanol isomers. *Combustion and Flame*, **2012**, 159 (6), 2028-2055.
3. Merchant, S. S.; Zanoelo, E. F.; Speth, R. L.; Harper, M. R.; Van Geem, K. M.; Green, W. H., Combustion and pyrolysis of iso-butanol: Experimental and chemical kinetic modeling study. *Combustion and Flame*, **2013**, 160 (10), 1907-1929.
4. Frassoldati, A.; Cuoci, A.; Faravelli, T.; Niemann, U.; Ranzi, E.; Seiser, R.; Seshadri, K., An experimental and kinetic modeling study of n-propanol and iso-propanol combustion. *Combustion and Flame*, **2010**, 157 (1), 2-16.
5. Frassoldati, A.; Cuoci, A.; Faravelli, T.; Ranzi, E., Kinetic modeling of the oxidation of ethanol and gasoline surrogate mixtures. *Combustion Science and Technology*, **2010**, 182 (4-6), 653-667.
6. Frassoldati, A.; Grana, R.; Faravelli, T.; Ranzi, E.; Oßwald, P.; Kohse-Höinghaus, K., Detailed kinetic modeling of the combustion of the four butanol isomers in premixed low-pressure flames. *Combustion and Flame*, **2012**, 159 (7), 2295-2311.
7. Goldaniga, A.; Faravelli, T.; Ranzi, E.; Dagaut, P.; Cathonnet, M. Oxidation of oxygenated octane improvers: MTBE, ETBE, DIPE, and TAME. in Symposium (International) on Combustion. 1998 27 (1) 353-360.

8. Wang, H.; Frenklach, M., A detailed kinetic modeling study of aromatics formation in laminar premixed acetylene and ethylene flames. *Combustion and flame,* **1997**, 110 (1), 173-221.

9. Jess, A., What might be the energy demand and energy mix to reconcile the world's pursuit of welfare and happiness with the necessity to preserve the integrity of the biosphere? *Energy Policy* **2010**, 38 (8), 4663–4678.

10. Glassman, I.; Yetter, R. A., Combustion 2008: (4th ed.) Academic Press

11. Nigam, P. S.; Singh, A., Production of liquid biofuels from renewable resources. *Progress in energy and combustion science,* **2011**, 37 (1), 52-68.

12. Demain, A. L., Biosolutions to the energy problem. *Journal of industrial microbiology & biotechnology,* **2009**, 36 (3), 319-332.

13. Barron, N.; Brady, D.; Love, G.; Marchant, R.; Nigam, P.; McHale, L.; McHale, A., Alginate-immobilized thermotolerant yeast for conversion of cellulose to ethanol. *Progress in Biotechnology,* **1996**, 11, 379-383.

14. Othmer, K., Encyclopedia of Chemical Technology. Vol. 4 (1). 1991: John Wiley and Sons, New York, .

15. Zhang, Z.; Huang, Z.; Wang, X.; Xiang, J.; Wang, X.; Miao, H., Measurements of laminar burning velocities and Markstein lengths for methanol–air–nitrogen mixtures at elevated pressures and temperatures. *Combustion and Flame,* **2008**, 155 (3), 358-368.

16. Sarathy, S.; Thomson, M.; Togbé, C.; Dagaut, P.; Halter, F.; Mounaim-Rousselle, C., An experimental and kinetic modeling study of n-butanol combustion. *Combustion and Flame,* **2009**, 156 (4), 852-864.

17. Gu, X.; Huang, Z.; Wu, S.; Li, Q., Laminar burning velocities and flame instabilities of butanol isomers–air mixtures. *Combustion and Flame*, **2010**, 157 (12), 2318-2325.

18. Veloo, P. S.; Wang, Y. L.; Egolfopoulos, F. N.; Westbrook, C. K., A comparative experimental and computational study of methanol, ethanol, and n-butanol flames. *Combustion and Flame*, **2010**, 157 (10), 1989-2004.

19. Moss, J. T.; Berkowitz, A. M.; Oehlschlaeger, M. A.; Biet, J.; Warth, V.; Glaude, P.-A.; Battin-Leclerc, F., An experimental and kinetic modeling study of the oxidation of the four isomers of butanol. *The Journal of Physical Chemistry A*, **2008**, 112 (43), 10843-10855.

20. Veloo, P. S.; Egolfopoulos, F. N., Flame propagation of butanol isomers/air mixtures. *Proceedings of the Combustion Institute*, **2011**, 33 (1), 987-993.

21. Jin, H.; Wang, Y.; Zhang, K.; Guo, H.; Qi, F., An experimental study on the formation of polycyclic aromatic hydrocarbons in laminar coflow non-premixed methane/air flames doped with four isomeric butanols. *Proceedings of the Combustion Institute*, **2013**, 34 (1), 779-786.

22. Yang, B.; Oßwald, P.; Li, Y.; Wang, J.; Wei, L.; Tian, Z.; Qi, F.; Kohse-Höinghaus, K., Identification of combustion intermediates in isomeric fuel-rich premixed butanol–oxygen flames at low pressure. *Combustion and Flame*, **2007**, 148 (4), 198-209.

23. Grana, R.; Frassoldati, A.; Faravelli, T.; Niemann, U.; Ranzi, E.; Seiser, R.; Cattolica, R.; Seshadri, K., An experimental and kinetic modeling study of combustion of isomers of butanol. *Combustion and Flame*, **2010**, 157 (11), 2137-2154.

24. Jin, H.; Cuoci, A.; Frassoldati, A.; Faravelli, T.; Wang, Y.; Li, Y.; Qi, F., Experimental and kinetic modeling study of PAH formation in methane coflow diffusion flames doped with n-butanol. *Combustion and Flame*, **2014**, 161 (3), 657-670.

25. Ghiassi, H.; Toth, P.; Lighty, J. S., Sooting behaviors of n-butanol and n-dodecane blends. *Combustion and Flame*, **2014**, 161 (3), 671-679.

26. Wu, F.; Law, C. K., An experimental and mechanistic study on the laminar flame speed, Markstein length and flame chemistry of the butanol isomers. *Combustion and Flame*, **2013**, 160 (12), 2744-2756.

27. Wang, H.; Reitz, R. D.; Yao, M.; Yang, B.; Jiao, Q.; Qiu, L., Development of an n-heptane-n-butanol-PAH mechanism and its application for combustion and soot prediction. *Combustion and Flame*, **2013**, 160 (3), 504-519.

28. Oßwald, P.; Güldenberg, H.; Kohse-Höinghaus, K.; Yang, B.; Yuan, T.; Qi, F., Combustion of butanol isomers–a detailed molecular beam mass spectrometry investigation of their flame chemistry. *Combustion and Flame*, **2011**, 158 (1), 2-15.

29. Hansen, N.; Harper, M.; Green, W., High-temperature oxidation chemistry of n-butanol–experiments in low-pressure premixed flames and detailed kinetic modeling. *Physical Chemistry Chemical Physics*, **2011**, 13 (45), 20262-20274.

30. Hansen, N.; Merchant, S. S.; Harper, M. R.; Green, W. H., The predictive capability of an automatically generated combustion chemistry mechanism: Chemical structures of premixed iso-butanol flames. *Combustion and Flame*, **2013**, 160 (11), 2343-2351.

31. Noorani, K. E.; Akih-Kumgeh, B.; Bergthorson, J. M., Comparative high temperature shock tube ignition of C1-C4 primary alcohols. *Energy & fuels*, **2010**, 24 (NOV-DEC), 5834-5843.

32. Gu, X.; Huang, Z.; Li, Q.; Tang, C., Measurements of laminar burning velocities and Markstein lengths of n-butanol− air premixed mixtures at elevated temperatures and pressures. *Energy & Fuels*, **2009**, 23 (10), 4900-4907.

33. Gu, X.; Li, Q.; Huang, Z.; Zhang, N., Measurement of laminar flame speeds and flame stability analysis of tert-butanol–air mixtures at elevated pressures. *Energy Conversion and Management*, **2011**, 52 (10), 3137-3146.

34. Liu, W.; Kelley, A. P.; Law, C. K., Non-premixed ignition, laminar flame propagation, and mechanism reduction of n-butanol, iso-butanol, and methyl butanoate. *Proceedings of the Combustion Institute*, **2011**, 33 (1), 995-1002.

35. Norton, T. S.; Dryer, F. L. The flow reactor oxidation of C1− C4 alcohols and MTBE. in Symposium (International) on Combustion. 1991 23 (1) 179-185.

36. Lefkowitz, J. K.; Heyne, J. S.; Won, S. H.; Dooley, S.; Kim, H. H.; Haas, F. M.; Jahangirian, S.; Dryer, F. L.; Ju, Y., A chemical kinetic study of tertiary-butanol in a flow reactor and a counterflow diffusion flame. *Combustion and Flame*, **2012**, 159 (3), 968-978.

37. Van Geem, K. M.; Pyl, S. P.; Marin, G. B.; Harper, M. R.; Green, W. H., Accurate high-temperature reaction networks for alternative fuels: butanol isomers. *Industrial & Engineering Chemistry Research*, **2010**, 49 (21), 10399-10420.

38. Cai, J.; Zhang, L.; Yang, J.; Li, Y.; Zhao, L.; Qi, F., Experimental and kinetic modeling study of tert-butanol combustion at low pressure. *Energy*, **2012**, 43 (1), 94-102.

39. Cai, J.; Zhang, L.; Zhang, F.; Wang, Z.; Cheng, Z.; Yuan, W.; Qi, F., Experimental and kinetic modeling study of n-butanol pyrolysis and combustion. *Energy & Fuels*, **2012**, 26 (9), 5550-5568.

40. Stranic, I.; Chase, D. P.; Harmon, J. T.; Yang, S.; Davidson, D. F.; Hanson, R. K., Shock tube measurements of ignition delay times for the butanol isomers. *Combustion and Flame*, **2012**, 159 (2), 516-527.

41. Black, G.; Curran, H.; Pichon, S.; Simmie, J.; Zhukov, V., Bio-butanol: Combustion properties and detailed chemical kinetic model. *Combustion and Flame*, **2010**, 157 (2), 363-373.

42. Yasunaga, K.; Mikajiri, T.; Sarathy, S. M.; Koike, T.; Gillespie, F.; Nagy, T.; Simmie, J. M.; Curran, H. J., A shock tube and chemical kinetic modeling study of the pyrolysis and oxidation of butanols. *Combustion and Flame*, **2012**, 159 (6), 2009-2027.

43. Stranic, I.; Pyun, S. H.; Davidson, D. F.; Hanson, R. K., Multi-species measurements in 1-butanol pyrolysis behind reflected shock waves. *Combustion and Flame*, **2012**, 159 (11), 3242-3250.

44. Rosado-Reyes, C. M.; Tsang, W., Shock tube study on the thermal decomposition of n-butanol. *The Journal of Physical Chemistry A*, **2012**, 116 (40), 9825-9831.

45. Cook, R. D.; Davidson, D. F.; Hanson, R. K., Multispecies laser measurements of n-butanol pyrolysis behind reflected shock waves. *International Journal of Chemical Kinetics*, **2012**, 44 (5), 303-311.

46. Vranckx, S.; Heufer, K.; Lee, C.; Olivier, H.; Schill, L.; Kopp, W.; Leonhard, K.; Taatjes, C.; Fernandes, R., Role of peroxy chemistry in the high-pressure ignition of n-butanol–Experiments and detailed kinetic modelling. *Combustion and Flame*, **2011**, 158 (8), 1444-1455.

47. Heufer, K. A.; Fernandes, R. X.; Olivier, H.; Beeckmann, J.; Röhl, O.; Peters, N., Shock tube investigations of ignition delays of n-butanol at elevated pressures between 770 and 1250K. *Proceedings of the Combustion Institute*, **2011**, 33 (1), 359-366.

48. Zhu, Y.; Davidson, D. F.; Hanson, R. K., 1-Butanol ignition delay times at low temperatures: An application of the constrained-reaction-volume strategy. *Combustion and Flame*, **2014**, 161 (3), 634-643.

49. Zhang, J.; Niu, S.; Zhang, Y.; Tang, C.; Jiang, X.; Hu, E.; Huang, Z., Experimental and modeling study of the auto-ignition of n-heptane/n-butanol mixtures. *Combustion and Flame*, **2013**, 160 (1), 31-39.

50. Weber, B. W.; Kumar, K.; Zhang, Y.; Sung, C.-J., Autoignition of n-butanol at elevated pressure and low-to-intermediate temperature. *Combustion and Flame*, **2011**, 158 (5), 809-819.

51. Weber, B. W.; Sung, C.-J., Comparative autoignition trends in butanol isomers at elevated pressure. *Energy & Fuels*, **2013**, 27 (3), 1688-1698.

52. Yang, Z.; Wang, Y.; Yang, X.; Qian, Y.; Lu, X.; Huang, Z., Autoignition of butanol isomers/n-heptane blend fuels on a rapid compression machine in N2/O2/Ar mixtures. *Science China Technological Sciences*, **2014**, 57 (3), 461-470.

53. Kumar, K.; Zhang, Y.; Sung, C.-J.; Pitz, W. J., Autoignition response of n-butanol and its blends with primary reference fuel constituents of gasoline. *Combustion and Flame*, **2015**, 162 (6), 2466-2479.

54. Barnard, J. A., The pyrolysis of n-butanol. *Transactions of the Faraday Society*, **1957**, 53, 1423-1430.

55. Barnard, J. A., The pyrolysis of tert.-butanol. *Transactions of the Faraday Society*, **1959**, 55, 947-951.

56. Tsang, W., Thermal Decomposition of Some Tert-Butyl Compounds at Elevated Temperatures. *The Journal of Chemical Physics*, **1964**, 40 (6), 1498-1505.

57. Lewis, D.; Keil, M.; Sarr, M., Gas phase thermal decomposition of tert-butyl alcohol. *Journal of the American Chemical Society*, **1974**, 96 (14), 4398-4404.

58. Choudhury, T. K.; Lna, M. C.; Lin, C. Y.; Sanders, W. A., Thermal decomposition of t-butyl alcohol in shock waves. *Combustion Science and Technology*, **1990**, 71 (4-6), 219-232.

59. Dagaut, P.; Sarathy, S. M.; Thomson, M. J., A chemical kinetic study of n-butanol oxidation at elevated pressure in a jet stirred reactor. *Proceedings of the combustion Institute*, **2009**, 32 (1), 229-237.

60. Togbé, C.; Mzé-Ahmed, A.; Dagaut, P., Kinetics of oxidation of 2-butanol and isobutanol in a jet-stirred reactor: experimental study and modeling investigation. *Energy & Fuels*, **2010**, 24 (9), 5244-5256.

61. Saisirirat, P.; Togbé, C.; Chanchaona, S.; Foucher, F.; Mounaim-Rousselle, C.; Dagaut, P., Auto-ignition and combustion characteristics in HCCI and JSR using 1-butanol/n-heptane and ethanol/n-heptane blends. *Proceedings of the Combustion Institute*, **2011**, 33 (2), 3007-3014.

62. Togbe, C.; Dayma, G.; Mze-Ahmed, A.; Dagaut, P., Experimental and modeling study of the kinetics of oxidation of simple biodiesel− biobutanol surrogates: Methyl octanoate− butanol mixtures. *Energy & Fuels*, **2010**, 24 (7), 3906-3916.

63. Dagaut, P.; Togbé, C., Experimental and modeling study of the kinetics of oxidation of butanol− n-heptane mixtures in a jet-stirred reactor. *Energy & Fuels*, **2009**, 23 (7), 3527-3535.

64. Dagaut, P.; Togbé, C., Oxidation kinetics of butanol–gasoline surrogate mixtures in a jet-stirred reactor: experimental and modeling study. *Fuel*, **2008**, 87 (15), 3313-3321.

65. Alasfour, F., Butanol—a single cylinder engine study: engine performance. *International journal of energy research*, **1997**, 21 (1), 21-30.

66. Alasfour, F., Butanol—a single-cylinder engine study: availability analysis. *Applied Thermal Engineering*, **1997**, 17 (6), 537-549.

67. Gautam, M.; Martin, D., Combustion characteristics of higher-alcohol/gasoline blends. *Proceedings of the Institution of Mechanical Engineers, Part A: Journal of Power and Energy*, **2000**, 214 (5), 497-511.

68. Gautam, M.; Martin, D.; Carder, D., Emissions characteristics of higher alcohol/gasoline blends. *Proceedings of the Institution of Mechanical Engineers, Part A: Journal of Power and Energy*, **2000**, 214 (2), 165-182.

69. Yacoub, Y.; Bata, R.; Gautam, M., The performance and emission characteristics of C1-C5 alcohol-gasoline blends with matched oxygen content in a single-cylinder spark ignition engine. *Proceedings of the Institution of Mechanical Engineers, Part A: Journal of Power and Energy*, **1998**, 212 (5), 363-379.

70. Bhattacharya, T.; Chatterjee, S.; Mishra, T., Performance of a constant speed CI engine on alcohol-Diesel microemulsions. *Applied Engineering in Agriculture*, **2004**, 20 (3), 253.

71. Camacho, J.; Lieb, S.; Wang, H., Evolution of size distribution of nascent soot in n-and i-butanol flames. *Proceedings of the Combustion Institute*, **2013**, 34 (1), 1853-1860.

72. Glassman, I. Soot formation in combustion processes. in Symposium (international) on combustion. 1989 22 (1) 295-311.

73. Vander Wal, R. L.; Jensen, K. A.; Choi, M. Y., Simultaneous laser-induced emission of soot and polycyclic aromatic hydrocarbons within a gas-jet diffusion flame. *Combustion and Flame*, **1997**, 109 (3), 399-414.

74. Reilly, P.; Gieray, R.; Whitten, W.; Ramsey, J., Direct observation of the evolution of the soot carbonization process in an acetylene diffusion flame via real-time aerosol mass spectrometry. *Combustion and flame*, **2000**, 122 (1), 90-104.

75. Richter, H.; Howard, J. B., Formation of polycyclic aromatic hydrocarbons and their growth to soot—a review of chemical reaction pathways. *Progress in Energy and Combustion science*, **2000**, 26 (4), 565-608.

76. Frenklach, M.; Warnatz, J., Detailed modeling of PAH profiles in a sooting low-pressure acetylene flame. *Combustion science and technology*, **1987**, 51 (4-6), 265-283.

77. Appel, J.; Bockhorn, H.; Frenklach, M., Kinetic modeling of soot formation with detailed chemistry and physics: laminar premixed flames of C 2 hydrocarbons. *Combustion and Flame*, **2000**, 121 (1), 122-136.

78. Frenklach, M., Reaction mechanism of soot formation in flames. *Physical Chemistry Chemical Physics*, **2002**, 4 (11), 2028-2037.

79. Frenklach, M.; Wang, H. Detailed modeling of soot particle nucleation and growth. in Symposium (International) on Combustion. 1991 23 (1) 1559-1566.

80. Frenklach, M.; Wang, H., Detailed mechanism and modeling of soot particle formation, in Soot formation in combustion. 1994, Springer. p. 165-192.

81. Colket, M. B.; Seery, D. J. Reaction mechanisms for toluene pyrolysis. in Symposium (International) on Combustion. 1994 25 (1) 883-891.

82. D'Anna, A.; Violi, A. A kinetic model for the formation of aromatic hydrocarbons in premixed laminar flames. in Symposium (International) on Combustion. 1998 27 (1) 425-433.

83. D'Anna, A.; Kent, J., A model of particulate and species formation applied to laminar, nonpremixed flames for three aliphatic-hydrocarbon fuels. *Combustion and Flame*, **2008**, 152 (4), 573-587.

84. Miller, J. A.; Klippenstein, S. J.; Georgievskii, Y.; Harding, L. B.; Allen, W. D.; Simmonett, A. C., Reactions between Resonance-Stabilized Radicals: Propargyl+ Allyl†. *The Journal of Physical Chemistry A*, **2010**, 114 (14), 4881-4890.

85. Hansen, N.; Miller, J. A.; Klippenstein, S. J.; Westmoreland, P. R.; Kohse-Höinghaus, K., Exploring formation pathways of aromatic compounds in laboratory-based model flames of aliphatic fuels. *Combustion, Explosion, and Shock Waves*, **2012**, 48 (5), 508-515.

86. Dean, A. M., Detailed kinetic modeling of autocatalysis in methane pyrolysis. *Journal of Physical Chemistry*, **1990**, 94 (4), 1432-1439.

87. Marinov, N.; Pitz, W.; Westbrook, C.; Castaldi, M.; Senkan, S., Modeling of aromatic and polycyclic aromatic hydrocarbon formation in premixed methane and ethane flames. *Combustion Science and Technology*, **1996**, 116 (1-6), 211-287.

88. D'Anna, A.; Kent, J., Aromatic formation pathways in non-premixed methane flames. *Combustion and flame*, **2003**, 132 (4), 715-722.

89. Richter, H.; Grieco, W. J.; Howard, J. B., Formation mechanism of polycyclic aromatic hydrocarbons and fullerenes in premixed benzene flames. *Combustion and flame*, **1999**, 119 (1), 1-22.

90. Schenk, M.; Hansen, N.; Vieker, H.; Beyer, A.; Gölzhäuser, A.; Kohse-Höinghaus, K., PAH formation and soot morphology in flames of C 4 fuels. *Proceedings of the Combustion Institute*, **2015**, 35 (2), 1761-1769.

91. Hwang, J. Y.; Lee, W.; Kang, H. G.; Chung, S. H., Synergistic effect of ethylene–propane mixture on soot formation in laminar diffusion flames. *Combustion and flame*, **1998**, 114 (3), 370-380.

92. Hwang, J. Y.; Chung, S. H.; Lee, W. Effects of oxygen and propane addition on soot formation in counterflow ethylene flames and the role of C 3 chemistry. in Symposium (International) on Combustion. 1998 27 (1) 1531-1538.

93. Cole, J. A.; Bittner, J. D.; Longwell, J. P.; Howard, J. B., Formation mechanisms of aromatic compounds in aliphatic flames. *Combustion and Flame*, **1984**, 56 (1), 51-70.

94. Wu, C.; Kern, R., Shock-tube study of allene pyrolysis. *Journal of Physical Chemistry*, **1987**, 91 (24), 6291-6296.

95. McEnally, C. S.; Pfefferle, L. D., Experimental assessment of naphthalene formation mechanisms in non-premixed flames. *Combustion science and technology*, **1997**, 128 (1-6), 257-278.

96. Castaldi, M. J.; Marinov, N. M.; Melius, C. F.; Huang, J.; Senkan, S. M.; Pit, W. J.; Westbrook, C. K. Experimental and modeling investigation of aromatic and polycyclic aromatic hydrocarbon formation in a premixed ethylene flame. in Symposium (International) on Combustion. 1996 26 (1) 693-702.

97. McEnally, C.; Pfefferle, L., An experimental study in non-premixed flames of hydrocarbon growth processes that involve five-membered carbon rings. *Combustion science and technology*, **1998**, 131 (1-6), 323-344.

98. Karataş, A. E.; Gülder, Ö. L., Soot formation in high pressure laminar diffusion flames. *Progress in Energy and Combustion Science*, **2012**, 38 (6), 818-845.

99. Warnatz, J.; Maas, U.; Dibble, R., Combustion, Physical and Chemical Fundamentals, Modeling and Simulation, Experiments, Pollutant Formation. 2006: Springer, Berlin-Heidelberg, Germany.

100. Bockhorn, H., Soot Formation in Combustion. 1994: Springer, Berlin-Heidelberg, Germany.

101. Dockery, D. W.; Pope, C. A.; Xu, X.; Spengler, J. D.; Ware, J. H.; Fay, M. E.; Jr, B. G. F.; Speizer, F. E., An association between air pollution and mortality in six US cities. *New England journal of medicine*, **1993**, 329 (24), 1753-1759.

102. McCrain, L. L.; Roberts, W. L., Measurements of the soot volume field in laminar diffusion flames at elevated pressures. *Combustion and Flame*, **2005**, 140 (1), 60-69.

103. Hui, X.; Kumar, K.; Sung, C.-J.; Edwards, T.; Gardner, D., Experimental studies on the combustion characteristics of alternative jet fuels. *Fuel*, **2012**, 98, 176-182.

104. Hui, X.; Sung, C.-J., Laminar flame speeds of transportation-relevant hydrocarbons and jet fuels at elevated temperatures and pressures. *Fuel*, **2013**, 109, 191-200.

105. Hui, X.; Das, A. K.; Kumar, K.; Sung, C.-J.; Dooley, S.; Dryer, F. L., Laminar flame speeds and extinction stretch rates of selected aromatic hydrocarbons. *Fuel*, **2012**, 97, 695-702.

106. Hofmann, M.; Bessler, W.; Schulz, C.; Jander, H., Laser-induced incandescence for soot diagnostics at high pressures. *Applied optics*, **2003**, 42 (12), 2052-2062.

107. Liu, F.; Daun, K.; Snelling, D. R.; Smallwood, G. J., Heat conduction from a spherical nano-particle: status of modeling heat conduction in laser-induced incandescence. *Applied physics B*, **2006**, 83 (3), 355-382.

108. Boïarciuc, A.; Foucher, F.; Mounaïm-Rousselle, C., Soot volume fractions and primary particle size estimate by means of the simultaneous two-color-time-resolved and 2D laser-induced incandescence. *Applied Physics B*, **2006**, 83 (3), 413-421.

109. Dreier, T.; Bougie, B.; Dam, N.; Gerber, T., Modeling of time-resolved laser-induced incandescence transients for particle sizing in high-pressure spray combustion environments: a comparative study. *Applied physics B*, **2006**, 83 (3), 403-411.

110. Ni, T.; Gupta, S.; Santoro, R. Suppression of soot formation in ethene laminar diffusion flames by chemical additives. in Symposium (International) on Combustion. 1994 25 (1) 585-592.

111. Vander Wal, R. L.; Jensen, K. A., Laser-induced incandescence: excitation intensity. *Applied optics*, **1998**, 37 (9), 1607-1616.

112. Braun-Unkhoff, M.; Chrysostomou, A.; Frank, P.; Gutheil, E.; Lückerath, R.; Stricker, W., Experimental and numerical study on soot formation in laminar high-pressure flames. *Symposium (International) on Combustion*, **1998**, 27 (1), 1565-1572.

113. Angrill, O.; Geitlinger, H.; Streibel, T.; Suntz, R.; Bockhorn, H., Influence of exhaust gas recirculation on soot formation in diffusion flames. *Proceedings of the Combustion Institute*, **2000**, 28 (2), 2643-2649.

114. Cignoli, F.; De Iuliis, S.; Manta, V.; Zizak, G., Two-dimensional two-wavelength emission technique for soot diagnostics. *Applied Optics*, **2001**, 40 (30), 5370-5378.

115. Krüger, V.; Wahl, C.; Hadef, R.; Geigle, K. P.; Stricker, W.; Aigner, M., Comparison of laser-induced incandescence method with scanning mobility particle sizer technique: the influence of probe sampling and laser heating on soot particle size distribution. *Measurement Science and Technology*, **2005**, 16 (7), 1477.

116. Bockhorn, H.; Geitlinger, H.; Jungfleisch, B.; Lehre, T.; Schön, A.; Streibel, T.; Suntz, R., Progress in characterization of soot formation by optical methods. *Physical Chemistry Chemical Physics*, **2002**, 4 (15), 3780-3793.

117. Park, J.; Ryoo, H. C.; Chun, H. S.; Song, S.; Hahn, J. W.; Chun, K. M., A study on time-resolved laser induced incandescence analysis method for the measurement of primary particle size in diesel exhaust. *JSME International Journal Series B Fluids and Thermal Engineering*, **2006**, 49 (4), 1351-1357.

118. Filippov, A. V.; Markus, M. W.; Roth, P., In-situ characterization of ultrafine particles by laser-induced incandescence: sizing and particle structure determination. *Journal of Aerosol Science*, **1999**, 30 (1), 71-87.

119. Cignoli, F.; Benecchi, S.; Zizak, G., Time-delayed detection of laser-induced incandescence for the two-dimensional visualization of soot in flames. *Applied optics*, **1994**, 33 (24), 5778-5782.

120. Ni, T.; Pinson, J.; Gupta, S.; Santoro, R., Two-dimensional imaging of soot volume fraction by the use of laser-induced incandescence. *Applied Optics*, **1995**, 34 (30), 7083-7091.

121. Shaddix, C. R.; Harrington, J. E.; Smyth, K. C., Quantitative measurements of enhanced soot production in a flickering methane/air diffusion flame. *Combustion and Flame*, **1994**, 99 (3), 723-732.

122. Quay, B.; Lee, T.-W.; Ni, T.; Santoro, R., Spatially resolved measurements of soot volume fraction using laser-induced incandescence. *Combustion and Flame*, **1994**, 97 (3), 384-392.

123. Shaddix, C. R.; Smyth, K. C., Laser-induced incandescence measurements of soot production in steady and flickering methane, propane, and ethylene diffusion flames. *Combustion and Flame*, **1996**, 107 (4), 418-452.

124. Vander Wal, R.; Weiland, K., Laser-induced incandescence: development and characterization towards a measurement of soot-volume fraction. *Applied Physics B*, **1994**, 59 (4), 445-452.

125. Dasch, C. J., Continuous-wave probe laser investigation of laser vaporization of small soot particles in a flame. *Applied optics*, **1984**, 23 (13), 2209-2215.

126. Santoro, R. J.; Shaddix, C. R., in Applied Combustion Diagnostics p. 252-286.

127. Will, S.; Schraml, S.; Bader, K.; Leipertz, A., Performance characteristics of soot primary particle size measurements by time-resolved laser-induced incandescence. *Applied optics*, **1998**, 37 (24), 5647-5658.

128. Melton, L. A., Soot diagnostics based on laser heating. *Applied optics*, **1984**, 23 (13), 2201-2208.

129. Bejaoui, S.; Lemaire, R.; Desgroux, P.; Therssen, E., Experimental study of the E (m, λ)/E (m, 1064) ratio as a function of wavelength, fuel type, height above the burner and temperature. *Applied Physics B*, **2014**, 116 (2), 313-323.

130. Leermakers, C. A. J.; Musculus, M. P. B., In-cylinder soot precursor growth in a low-temperature combustion diesel engine: Laser-induced fluorescence of polycyclic aromatic hydrocarbons. *Proceedings of the Combustion Institute*, **2015**, 35 (3), 3079-3086.

131. Singh, P.; Hui, X.; Sung, C.-J., Soot formation in non-premixed counterflow flames of butane and butanol isomers. *Combustion and Flame*, **2016**, 164, 167–182.

132. Santoro, R. J.; Shaddix, C. R., Laser-induced incandescence. *Applied combustion diagnostics*, **2002**, 252-286.

133. Snelling, D. R.; Smallwood, G. J.; Liu, F.; Gülder, O. L.; Bachalo, W. D., A calibration-independent laser-induced incandescence technique for soot measurement by detecting absolute light intensity. *Applied Optics*, **2005**, 44 (31), 6773-85.

134. Hanisch, S.; Jander, H.; Pape, T.; Wagner, H. G. Soot mass growth and coagulation of soot particles in $C_2 H_4$/air-flames at 15 bar. in Symposium (International) on Combustion. 1994 25 (1) 577-584.

135. Bengtsson, P. E.; Aldén, M., Soot-visualization strategies using laser techniques. *Applied Physics B*, **1995**, 60 (1), 51-59.

136. Schraml, S.; Dankers, S.; Bader, K.; Will, S.; Leipertz, A., Soot temperature measurements and implications for time-resolved laser-induced incandescence (TIRE-LII). *Combustion and Flame*, **2000**, 120 (4), 439-450.

137. McDonald, J. R.; Baronavski, A. P.; Donnelly, V. M., Multiphoton-vacuum-ultraviolet laser photodissociation of acetylene: Emission from electronically excited fragments. *Chemical Physics*, **1978**, 33 (2), 161-170.

138. Decroix, M. E.; Roberts, W. L., Transient flow field effects on soot volume fraction in diffusion flames. *Combustion science and technology*, **2000**, 160 (1), 165-189.

139. Vander Wal, R. L.; Ticich, T. M.; Stephens, A. B., Optical and microscopy investigations of soot structure alterations by laser-induced incandescence. *Applied Physics B*, **1998**, 67 (1), 115-123.

140. Witze, P. O.; Hochgreb, S.; Kayes, D.; Michelsen, H. A.; Shaddix, C. R., Time-resolved laser-induced incandescence and laser elastic-scattering measurements in a propane diffusion flame. *Applied Optics*, **2001**, 40 (15), 2443-2452.

141. Dasch, C. J., One-dimensional tomography: a comparison of Abel, onion-peeling, and filtered backprojection methods. *Applied optics*, **1992**, 31 (8), 1146-1152.

142. Smyth, K. C.; Shaddix, C. R., The elusive history of m∼= 1.57–0.56i for the refractive index of soot. *Combustion and Flame*, **1996**, 107 (3), 314-320.

143. Dalzell, W. H.; Sarofim, A. F., Optical constants of soot and their application to heat-flux calculations. *Journal of Heat Transfer*, **1969**, 91 (1), 100-104.

144. Batten, C. E., Spectral optical constants of soots from polarized angular reflectance measurements. *Applied optics*, **1985**, 24 (8), 1193-1199.

145. Mullins, J.; Williams, A., The optical properties of soot: a comparison between experimental and theoretical values. *Fuel*, **1987**, 66 (2), 277-280.

146. Charalampopoulos, T. T.; Felske, T. D., Refractive indices of soot particles deduced from in-situ laser light scattering measurements. *Combustion and flame*, **1987**, 68 (3), 283-294.

147. Charalampopoulos, T. T.; Chang, H., In situ optical properties of soot particles in the wavelength range from 340 nm to 600 nm. *Combustion Science and Technology*, **1988**, 59 (4-6), 401-421.

148. Charalampopoulos, T. T.; Chang, H.; Stagg, B., The effects of temperature and composition on the complex refractive index of flame soot. *Fuel*, **1989**, 68 (9), 1173-1179.

149. Chang, H.; Charalampopoulos, T. T. Determination of the wavelength dependence of refractive indices of flame soot. in Proceedings of the Royal Society of London A: Mathematical, Physical and Engineering Sciences. 1990 430 (1880) 577-591.

150. Lee, S. C.; Tien, C. L. Optical constants of soot in hydrocarbon flames. in Symposium (international) on combustion. 1981 18 (1) 1159-1166.

151. Williams, T. C.; Shaddix, C. R.; Jensen, K. A.; Suo-Antilla, J. M., Measurement of the dimensionless extinction coefficient of soot within laminar diffusion flames. *International Journal of Heat and Mass Transfer*, **2007**, 50 (7), 1616-1630.

152. Feng, Q.; Jalali, A.; Fincham, A. M.; Wang, Y. L.; Tsotsis, T. T.; Egolfopoulos, F. N., Soot formation in flames of model biodiesel fuels. *Combustion and Flame*, **2012**, 159 (5), 1876-1893.

153. Verstraete, L.; Léger, A., The visible and ultraviolet absorption of large polycyclic aromatic hydrocarbons. *Astronomy and Astrophysics*, **1992**, 266, 513-519.

154. Beretta, F.; Cincotti, V.; D'alessio, A.; Menna, P., Ultraviolet and visible fluorescence in the fuel pyrolysis regions of gaseous diffusion flames. *Combustion and flame*, **1985**, 61 (3), 211-218.

155. Berman, I. R., Handbook of Fluorescence Spectra of Aromatic Molecules. second ed. ed.: Academic Press, New York, 1971.

156. Zizak, G.; Cignoli, F.; Montas, G.; Benecchi, S.; Donde, R., Detection of aromatic hydrocarbons in the exhaust gases of a gasoline ic engine by laser-induced fluorescence technique. *Rec. Res. Dev. Appl. Spectrosc*, **1996**, 1, 17-24.

157. Petarca, L.; Marconi, F., Fluorescence spectra and polycyclic aromatic species in a n-heptane diffusion flame. *Combustion and flame*, **1989**, 78 (3), 308-325.

158. Lee, S. M.; Yoon, S. S.; Chung, S. H., Synergistic effect on soot formation in counterflow diffusion flames of ethylene–propane mixtures with benzene addition. *Combustion and flame*, **2004**, 136 (4), 493-500.

159. Smyth, K. C.; Shaddix, C. R.; Everest, D. A., Aspects of soot dynamics as revealed by measurements of broadband fluorescence and flame luminosity in flickering diffusion flames. *Combustion and Flame*, **1997**, 111 (3), 185-207.

160. Ciajolo, A.; Ragucci, R.; Apicella, B.; Barbella, R.; De Joannon, M.; Tregrossi, A., Fluorescence spectroscopy of aromatic species produced in rich premixed ethylene flames. *Chemosphere*, **2001**, 42 (5), 835-841.

161. Sgro, L.; Minutolo, P.; Basile, G.; D'Alessio, A., UV-visible spectroscopy of organic carbon particulate sampled from ethylene/air flames. *Chemosphere*, **2001**, 42 (5), 671-680.

162. Ciajolo, A.; Barbella, R.; Tregrossi, A.; Bonfanti, L. Spectroscopic and compositional signatures of PAH-loaded mixtures in the soot inception region of a premixed ethylene flame. in Symposium (International) on Combustion. 1998 27 (1) 1481-1487.

163. McEnally, C. S.; Pfefferle, L. D., Experimental study of nonfuel hydrocarbons and soot in coflowing partially premixed ethylene/air flames. *Combustion and Flame*, **2000**, 121 (4), 575-592.

164. Ossler, F.; Metz, T.; Aldén, M., Picosecond laser-induced fluorescence from gas-phase polycyclic aromatic hydrocarbons at elevated temperatures. I. Cell measurements. *Applied Physics B,* **2001**, 72 (4), 465-478.

165. Ciajolo, A.; Tregrossi, A.; Barbella, R.; Ragucci, R.; Apicella, B.; De Joannon, M., The relation between ultraviolet-excited fluorescence spectroscopy and aromatic species formed in rich laminar ethylene flames. *Combustion and flame,* **2001**, 125 (4), 1225-1229.

166. Choi, B. C.; Choi, S. K.; Chung, S.-H., Soot formation characteristics of gasoline surrogate fuels in counterflow diffusion flames. *Proceedings of the Combustion Institute*, **2011**, 33 (1), 609-616.

167. Wang, Y.; Raj, A.; Chung, S. H., A PAH growth mechanism and synergistic effect on PAH formation in counterflow diffusion flames. *Combustion and flame*, **2013**, 160 (9), 1667-1676.

168. Yoon, S. S.; Lee, S. M.; Chung, S. H., Effect of mixing methane, ethane, propane, and propene on the synergistic effect of PAH and soot formation in ethylene-base counterflow diffusion flames. *Proceedings of the Combustion Institute*, **2005**, 30 (1), 1417-1424.

169. CHEMKIN-PRO. **2011**, Reaction Design: San Diego.

170. Kee, R. J.; Miller, J. A.; Evans, G. H.; Dixon-Lewis, G. Chemkin II: A computational model of the structure and extinction of strained, opposed flow, premixed methane-air flames. in Symposium (International) on Combustion. 1989 22 (1) 1479-1494.

171. Menon, A. V., *Effect Of M-Xylene On Soot Formation In High Pressure Diffusion,* The Pennsylvania State University, 2010, https://etda.libraries.psu.edu/catalog/10696.

172. Williams, F. A., Combustion Theory. 1985: Addison-Wesley.

173. Seshadri, K.; Williams, F. A., Laminar flow between parallel plates with injection of a reactant at high Reynolds number. *International Journal of Heat and Mass Transfer*, **1978**, 21 (2), 251-253.

174. Kreutz, T. G.; Law, C. K., Ignition in nonpremixed counterflowing hydrogen versus heated air: Computational study with detailed chemistry. *Combustion and Flame*, **1996**, 104 (1), 157-175.

175. Fotache, C. G.; Wang, H.; Law, C. K., Ignition of ethane, propane, and butane in counterflow jets of cold fuel versus hot air under variable pressures. *Combustion and Flame*, **1999**, 117 (4), 777-794.

176. Wang, H.; Frenklach, M., Enthalpies of formation of benzenoid aromatic molecules and radicals. *The Journal of physical chemistry*, **1993**, 97 (15), 3867-3874.

177. Wang, H.; Frenklach, M., Calculations of rate coefficients for the chemically activated reactions of acetylene with vinylic and aromatic radicals. *The Journal of Physical Chemistry*, **1994**, 98 (44), 11465-11489.

178. Wang, H.; Frenklach, M., Transport properties of polycyclic aromatic hydrocarbons for flame modeling. *Combustion and flame*, **1994**, 96 (1), 163-170.

179. McEnally, C. S.; Pfefferle, L. D., Fuel decomposition and hydrocarbon growth processes for oxygenated hydrocarbons: butyl alcohols. *Proceedings of the Combustion Institute*, **2005**, 30 (1), 1363-1370.

180. McMurry, P. H., A review of atmospheric aerosol measurements. *Atmospheric Environment*, **2000**, 34 (12), 1959-1999.

181. Du, J.; Axelbaum, R. L., The effect of flame structure on soot-particle inception in diffusion flames. *Combustion and Flame,* **1995**, 100 (3), 367-375.

182. Du, J.; Axelbaum, R. L. The effects of flame structure on extinction of CH 4-O 2-N 2 diffusion flames. in Symposium (international) on Combustion. 1996 26 (1) 1137-1142.

183. Chao, B.; Liu, S.; Axelbaum, R., On soot inception in nonpremixed flames and the effects of flame structure. *Combustion science and technology,* **1998**, 138 (1-6), 105-135.

184. Sunderland, P.; Axelbaum, R. L.; Urban, D.; Chao, B.; Liu, S., Effects of structure and hydrodynamics on the sooting behavior of spherical microgravity diffusion flames. *Combustion and Flame,* **2003**, 132 (1), 25-33.

185. Sung, C.; Liu, J.; Law, C., Structural response of counterflow diffusion flames to strain rate variations. *Combustion and Flame,* **1995**, 102 (4), 481-492.

186. Wang, Y.; Chung, S. H., Effect of strain rate on sooting limits in counterflow diffusion flames of gaseous hydrocarbon fuels: Sooting temperature index and sooting sensitivity index. *Combustion and Flame,* **2014**, 161 (5), 1224-1234.

187. McEnally, C. S.; Pfefferle, L. D., Sooting tendencies of oxygenated hydrocarbons in laboratory-scale flames. *Environmental science & technology,* **2011**, 45 (6), 2498-2503.

188. Karataş, A. E.; Commodo, M.; Gülder, O. m. L., Soot formation in co-and counter-flow laminar diffusion flames of binary mixtures of ethylene and butane isomers and synergistic effects. *Energy & Fuels*, **2010**, 24 (9), 4912-4918.

189. Lemaire, R.; Lapalme, D.; Seers, P., Analysis of the sooting propensity of C-4 and C-5 oxygenates: Comparison of sooting indexes issued from laser-based experiments and group additivity approaches. *Combustion and Flame,* **2015**, 162 (9), 3140-3155.

190. Frenklach, M.; Clary, D. W.; Gardiner, W. C.; Stein, S. E. Detailed kinetic modeling of soot formation in shock-tube pyrolysis of acetylene. in Symposium (International) on Combustion. 1985 20 (1) 887-901.

191. Frenklach, M.; Gardiner, W.; Stein, S.; Clary, D.; Yuan, T., Mechanism of soot formation in acetylene-oxygen mixtures. *Combustion science and technology*, **1986**, 50 (1-3), 79-115.

192. Frenklach, M.; Clary, D. W.; Gardiner, W. C.; Stein, S. E. Effect of fuel structure on pathways to soot. in Symposium (International) on Combustion. 1988 21 (1) 1067-1076.

193. Frenklach, M.; Yuan, T.; Ramachandra, M., Soot formation in binary hydrocarbon mixtures. *Energy & fuels*, **1988**, 2 (4), 462-480.

194. Frenklach, M.; Wang, H., Soot Formation in Combustion in Mechanisms and Models. 1994, Springer-Verlag, Heidelberg. p. 165-189.

195. Kern, R. D.; Xie, K., Shock tube studies of gas phase reactions preceding the soot formation process. *Progress in energy and combustion science*, **1991**, 17 (3), 191-210.

196. Glassman, I.; Yetter, R. A.; Glumac, N. G., Environmental combustion considerations, in Combustion 2014, 5th Edition, Academic Press. p. 393-472.

197. Stein, S. E.; Walker, J. A.; Suryan, M. M.; Fahr, A. A new path to benzene in flames. in Symposium (International) on Combustion. 1991 23 (1) 85-90.

198. Melius, C. F.; Miller, J. A.; Evleth, E. M. Unimolecular reaction mechanisms involving C 3 H 4, C 4 H 4, and C 6 H 6 hydrocarbon species. in Symposium (International) on Combustion. 1992 24 (1) 621-628.

199. M.B. Colket, R. J. H., Soot Formation in Combustion, in Mechanisms and Models. 1994, Springer-Verlag, Heidelberg. p. 442-468.

200. Westmoreland, P. R.; Dean, A. M.; Howard, J. B.; Longwell, J. P., Forming benzene in flames by chemically activated isomerization. *The Journal of Physical Chemistry*, **1989**, 93 (25), 8171-8180.

201. McEnally, C. S.; Pfefferle, L. D.; Atakan, B.; Kohse-Höinghaus, K., Studies of aromatic hydrocarbon formation mechanisms in flames: Progress towards closing the fuel gap. *Progress in Energy and Combustion Science*, **2006**, 32 (3), 247-294.

202. Smyth, K. C.; Miller, J. H.; Dorfman, R. C.; Mallard, W. G.; Santoro, R. J., Soot inception in a methane/air diffusion flame as characterized by detailed species profiles. *Combustion and Flame*, **1985**, 62 (2), 157-181.

203. Haynes, B. S.; Jander, H.; Wagner, H. G., Optical Studies of Soot-Formation Processes in Premixed Flames. *Berichte der Bunsengesellschaft für physikalische Chemie*, **1980**, 84 (6), 585-592.

204. Prado, G.; Garo, A.; Ko, A.; Sarofim, A. Polycyclic aromatic hydrocarbons formation and destruction in a laminar diffusion flame. in Symposium (international) on combustion. 1985 20 (1) 989-996.

205. Beretta, F.; D'Alessio, A.; D'Orsi, A.; Minutolo, P., UV and visible laser excited fluorescence from rich premixed and diffusion flames. *Combustion science and technology*, **1992**, 85 (1-6), 455-470.

206. Santoro, R.; Semerjian, H.; Dobbins, R., Soot particle measurements in diffusion flames. *Combustion and Flame*, **1983**, 51, 203-218.

207. Santoro, R.; Semerjian, H. Soot formation in diffusion flames: flow rate, fuel species and temperature effects. in Symposium (International) on Combustion. 1985 20 (1) 997-1006.

208. Allen, M. G.; McManus, K. R.; Sonnenfroh, D. M.; Paul, P. H., Planar laser-induced-fluorescence imaging measurements of OH and hydrocarbon fuel fragments in high-pressure spray-flame combustion. *Applied optics*, **1995**, 34 (27), 6287-6300.

209. Vander Wal, R. L., Onset of carbonization: spatial location via simultaneous LIF-LII and characterization via TEM. *Combustion science and technology*, **1996**, 118 (4-6), 343-360.

210. Crittenden, B.; Long, R., Formation of polycyclic aromatics in rich premixed acetylene and ethylene flames. *Combustion and Flame*, **1973**, 20 (3), 359-368.

211. Bittner, J.; Howard, J. Composition profiles and reaction mechanisms in a near-sooting premixed benzene/oxygen/argon flame. in Symposium (International) on Combustion. 1981 18 (1) 1105-1116.

212. Smedley, J.; Williams, A.; Bartle, K., A mechanism for the formation of soot particles and soot deposits. *Combustion and flame*, **1992**, 91 (1), 71-82.

213. Mckinnon, J. T.; Meyer, E.; Howard, J. B., Infrared analysis of flame-generated PAH samples. *Combustion and flame*, **1996**, 105 (1), 161-166.

214. Mckinnon, J. T.; Howard, J. B. The roles of PAH and acetylene in soot nucleation and growth. in Symposium (International) on Combustion. 1992 24 (1) 965-971.

215. Senkan, S.; Castaldi, M., Formation of polycyclic aromatic hydrocarbons (PAH) in methane combustion: comparative new results from premixed flames. *Combustion and flame*, **1996**, 107 (1), 141-150.

216. Hepp, H.; Siegmann, K.; Sattler, K., New aspects of growth mechanisms for polycyclic aromatic hydrocarbons in diffusion flames. *Chemical physics letters*, **1995**, 233 (1), 16-22.

217. Bohm, H.; Braun-Unkhoff, M.; Frank, P., Investigations on initial soot formation at high pressures. *Progress in Computational Fluid Dynamics, an International Journal*, **2003**, 3 (2-4), 145-150.

218. Marinov, N. M.; Pitz, W. J.; Westbrook, C. K.; Vincitore, A. M.; Castaldi, M. J.; Senkan, S. M.; Melius, C. F., Aromatic and polycyclic aromatic hydrocarbon formation in a laminar premixed n-butane flame. *Combustion and flame*, **1998**, 114 (1), 192-213.

219. Kamphus, M.; Braun-Unkhoff, M.; Kohse-Höinghaus, K., Formation of small PAHs in laminar premixed low-pressure propene and cyclopentene flames: Experiment and modeling. *Combustion and Flame*, **2008**, 152 (1), 28-59.

220. Tsang, W., Thermal stability of alcohols. *International Journal of Chemical Kinetics*, **1976**, 8 (2), 173-192.

221. Marinov, N. M., A detailed chemical kinetic model for high temperature ethanol oxidation. *International Journal of Chemical Kinetics*, **1999**, 31 (3), 183-220.

222. Park, J.; Zhu, R.; Lin, M., Thermal Decomposition of Ethanol. 1. Ab Initio MO/RRKM Prediction of Rate Constant and Product Branching Ratios. *J. Chem. Phys*, **2002**, 117, 3224-31.

223. Bui, B.; Zhu, R.; Lin, M., Thermal decomposition of iso-propanol: first-principles prediction of total and product-branching rate constants. *Journal of Chemical Physics*, **2002**, 117 (24), 11188-11195.

224. Brezinsky, K.; Dryer, F., A Flow Reactor Study of the Oxidation of Iso-butylene and an Iso-butyleneln-octane Mixture. *Combustion science and technology*, **1986**, 45 (5-6), 225-232.

225. Tsang, W.; Walker, J. A. Mechanism and rate constants for the reactions of hydrogen atoms with isobutene at high temperatures. in Symposium (International) on Combustion. 1989 22 (1) 1015-1022.

226. Hansen, N.; Kasper, T.; Klippenstein, S. J.; Westmoreland, P. R.; Law, M. E.; Taatjes, C. A.; Kohse-Höinghaus, K.; Wang, J.; Cool, T. A., Initial steps of aromatic ring formation in a laminar premixed fuel-rich cyclopentene flame. *The Journal of Physical Chemistry A*, **2007**, 111 (19), 4081-4092.

227. Miller, J. A.; Pilling, M. J.; Troe, J., Unravelling combustion mechanisms through a quantitative understanding of elementary reactions. *Proceedings of the Combustion Institute*, **2005**, 30 (1), 43-88.

228. Kennedy, I. M., Models of soot formation and oxidation. *Progress in Energy and Combustion Science*, **1997**, 23 (2), 95-132.

229. Bohm, H.; Feldermann, C.; Heidermann, T.; Jander, H.; Luers, B.; Wagner, H., Soot formation in premixed C2H4-air flames for pressures up to 100 bar *Symposium(International) on Combustion*, **1992**, 24 (1), 991–998.

230. Singh, J.; Balthasar, M.; Kraft, M.; Wagner, W., Stochastic modeling of soot particle size and age distributions in laminar premixed flames. *Proceedings of the Combustion Institute*, **2005**, 30 (1), 1457-1465.

231. Patterson, R. I.; Singh, J.; Balthasar, M.; Kraft, M.; Wagner, W., Extending stochastic soot simulation to higher pressures. *Combustion and Flame*, **2006**, 145 (3), 638-642.

232. Flower, W. L.; Bowman, C. T., Measurements of the effect of elevated pressure on soot formation in laminar diffusion flames. *Combustion Science and Technology*, **1984**, 37, 93–97.

233. Flower, W. L.; Bowman, C. T., Soot production in axisymmetric laminar diffusion flames at pressures from one to ten atmospheres. *Twenty-first Symposium (International) on Combustion, Combust. Inst.*, **1986**, 21, 1115–1124.

234. Flower, W. L., Soot particle temperatures in axisymmetric laminar ethylene-air diffusion flames at pressures up to 0.7 MPa. *Combustion and flame*, **1989**, 77 (3), 279-293.

235. Lee, W.; Na, Y. D., Soot Study in Laminar Diffusion Flames at Elevated Pressure Using Two-Color Pyrometry and Abel Inversion. *JSME International Journal Series B*, **2000**, 43 (4), 550-555.

236. Bento, D. S.; Thomson, K. A.; Gülder, Ö. L., Soot formation and temperature field structure in laminar propane–air diffusion flames at elevated pressures. *Combustion and Flame*, **2006**, 145 (4), 765-778.

237. Joo, H. I.; Gülder, Ö. L., Soot formation and temperature field structure in co-flow laminar methane–air diffusion flames at pressures from 10 to 60atm. *Proceedings of the Combustion Institute*, **2009**, 32 (1), 769-775.

238. Zhou, L.; Dam, N. J.; Boot, M. D.; de Goey, L. P. H., Measurements of sooting tendency in laminar diffusion flames of n-heptane at elevated pressure. *Combustion and Flame*, **2013**, 160 (11), 2507-2516.

239. Thomson, K. A.; Gülder, Ö. L.; Weckman, E. J.; Fraser, R. A.; Smallwood, G. J.; Snelling, D. R., Soot concentration and temperature measurements in co-annular, nonpremixed CH 4/air laminar flames at pressures up to 4 MPa. *Combustion and Flame*, **2005**, 140 (3), 222-232.

240. Wang, H.; Du, D. X.; Sung, C. J.; Law, C. K., Experiments and numerical simulation on soot formation in opposed-jet ethylene diffusion flames. *Proc. Combust. Inst.* , **1996**, 26 (2), 2359–2368.

241. D'Anna, A.; Commodo, M.; Sirignano, M.; Minutolo, P.; Pagliara, R., Particle formation in opposed-flow diffusion flames of ethylene: An experimental and numerical study. *Proceedings of the Combustion Institute*, **2009**, 32 (1), 793-801.

242. Smooke, M. D.; Long, M. B.; Connelly, B. C.; Colket, M. B.; Hall, R. J., Soot formation in laminar diffusion flames. *Combustion and Flame*, **2005**, 143 (4), 613-628.

243. Smooke, M.; Hall, R.; Colket, M.; Fielding, J.; Long, M.; McEnally, C.; Pfefferle, L., Investigation of the transition from lightly sooting towards heavily sooting co-flow ethylene diffusion flames. *Combustion Theory and Modelling*, **2004**, 8 (3), 593-606.

244. Smooke, M.; McEnally, C.; Pfefferle, L.; Hall, R.; Colket, M., Computational and experimental study of soot formation in a coflow, laminar diffusion flame. *Combustion and Flame*, **1999**, 117 (1), 117-139.

245. Van Oijen, J. A.; De Goey, L. P. H., Modelling of premixed counterflow flames using the flamelet-generated manifold method. *Combustion Theory and Modelling*, **2002**, 6 (3), 463-478.

246. Slavinskaya, N. A.; Frank, P., A modelling study of aromatic soot precursors formation in laminar methane and ethene flames. *Combustion and Flame*, **2009**, 156 (9), 1705-1722.

247. Li, W.; Law, M. E.; Westmoreland, P. R.; Kasper, T.; Hansen, N.; Kohse-Höinghaus, K., Multiple benzene-formation paths in a fuel-rich cyclohexane flame. *Combustion and Flame*, **2011**, 158 (11), 2077-2089.

248. D'Anna, A.; Violi, A., Detailed modeling of the molecular growth process in aromatic and aliphatic premixed flames. *Energy & fuels*, **2005**, 19 (1), 79-86.

249. Liu, F.; Dworkin, S. B.; Thomson, M. J.; Smallwood, G. J., Modeling DME addition effects to fuel on PAH and soot in laminar coflow ethylene/air diffusion flames using two PAH mechanisms. *Combustion Science and Technology*, **2012**, 184 (7-8), 966-979.

250. Dworkin, S. B.; Zhang, Q.; Thomson, M. J.; Slavinskaya, N.; Riedel, U., Application of an enhanced PAH growth model to soot formation in a laminar coflow ethylene/air diffusion flame. *Combustion and Flame*, **2011**, 158 (9), 1682-1695.

251. Saffaripour, M.; Kholghy, M.; Dworkin, S. B.; Thomson, M. J., A numerical and experimental study of soot formation in a laminar coflow diffusion flame of a jet A-1 surrogate. *Proceedings of the Combustion Institute*, **2013**, 34 (1), 1057-1065.

252. Guo, H.; Gu, Z.; Thomson, K. A.; Smallwood, G. J.; Baksh, F. f., Soot formation in a laminar ethylene/air diffusion flame at pressures from 1 to 8atm. *Proceedings of the Combustion Institute*, **2013**, 34 (1), 1795-1802.

253. Violi, A.; D'Anna, A.; D'Alessio, A.; Sarofim, A. F., Modeling aerosol formation in opposed-flow diffusion flames. *Chemosphere*, **2003**, 51 (10), 1047-1054.

254. Cuoci, A.; Frassoldati, A.; Faravelli, T.; Ranzi, E., Formation of soot and nitrogen oxides in unsteady counterflow diffusion flames. *Combustion and Flame*, **2009**, 156 (10), 2010-2022.

255. Mehta, R. S.; Haworth, D. C.; Modest, M. F., An assessment of gas-phase reaction mechanisms and soot models for laminar atmospheric-pressure ethylene–air flames. *Proceedings of the Combustion Institute*, **2009**, 32 (1), 1327-1334.

256. Singh, P.; Sung, C. J., PAH Formation in Counterflow Non-Premixed Flames of Butane and Butanol Isomers. *Combustion and flame,* **2016**. 10.1016/j.combustflame.2016.05.009

257. Daily, J. W., Laser induced fluorescence spectroscopy in flames. *Progress in energy and combustion science*, **1997**, 23 (2), 133-199.

Appendix

Chemical structures of some of the intermediate species during initial fuel breaking processes.

	methyl	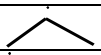	1-methyl-ethyl
	ethyl	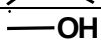	1-hydroxy-methyl
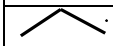	propyl	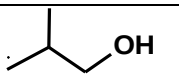	3-hydroxy-2-methyl-propyl
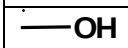	1-hydroxy-methyl	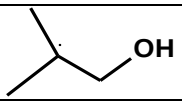	2-hydroxymethyl-1-methyl-ethyl
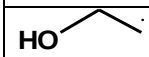	2-hydroxy-ethyl	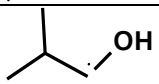	1-hydroxy-2-methyl-propyl
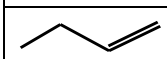	1-butene	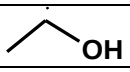	1-hydroxy-ethyl
	2-butene	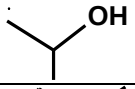	2-hydroxy-2-methyl-ethyl
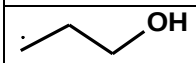	3-hydroxy-propyl	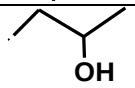	3-hydroxy-3-methyl-propyl
	4-hydroxy-butyl	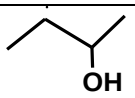	2-hydroxy-1-methyl-propyl
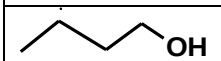	3-hydroxy-1-methyl-propyl	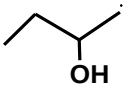	2-hydroxy-butyl
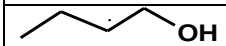	1-hydroxymethyl-propyl	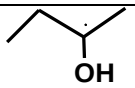	1-hydroxy-1-methyl-propyl
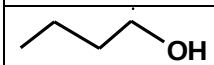	1-hydroxy-butyl	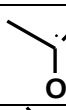	1-hydroxy-1-methyl-ethyl
	*iso*-butene	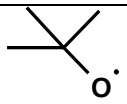	*tert*-butoxide
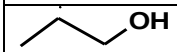	1-hydroxymethyl-ethyl	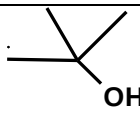	2-hydroxy-2-methyl-propyl